Remote-Controlled Self-Assembly of Three-Dimensional Micro Structures for Ultra-Sensitive Sensors and Three-Dimensional Metamaterials

A THESIS SUBMITTED TO THE FACULTY OF
THE UNIVERSITY OF MINNESOTA
BY

Chao Liu

IN PARTIAL FULFILLMENT OF THE
REQUIREMENTS FOR THE DEGREE OF
DOCTOR OF PHILOSOPHY

Advisor: Prof. Jeong-Hyun Cho

October 2018

Copyright

Acknowledgement

My sincere gratitude goes to my advisor Prof. Jeong-Hyun Cho for supporting my Ph.D. study and research. Without whom, it would not be possible for me to complete my Ph.D. work. His guidance, patience, kindness, and enthusiasm help me go through difficulties in research and even life. I am forever indebted to him for what I have learned from him and for making me who I am today.

I would also like to acknowledge the rest of my committee members: Prof. Campbell, Prof. Gopinath, and Prof. Cui for their encouragement and insightful suggestions.

I am grateful to the collaborators and all of those who have helped me through my research: Dr. Daeha Joung, Chunhui Dai, and Kriti Agarwal, for the help and support in preparing samples and finishing projects. Special thanks to Dr. Dibakar R. Chowdhury, Dr. Azad Abul from Los Alamos National Laboratory and Prof. Hyeong-Ryeol. Park, Prof. Sang-Hyun Oh, for all the transmission measurements. This dissertation and projects would not have completed without their helps.

There are many wonderful people who I worked with in the lab over the years. I am grateful to all of those who I absolutely have had the pleasure to work with: Chunhui Dai, Kriti Agarwal, Dr. Daeha Joung, Prof. Lianbi Li, Jiaxuan Wen, Daniel Wrakowski, Emily Zhou, Nick Buchele, Joseph Schauff, Dr. Sehyun Hwang, Avishek Mishra, Amulya Vishw, Nafiz Jaidye, Saran Kumar Chaganti, Neel Chatterjee, Seokhyeong Lee, Seung Yeon Lee, Yijia Liu, Aaron Bartnik.

Finally, I would like to express my love and thank to my fiancé, parents, and friends. This journey would not have been possible without their support and encouragement. Special thanks to my fiancé Stacey Jo Schugel, for not always being mad at me when I work late at night.

Dedication

To my parents,

for seeing the best in me and trusting what I am doing.

To my fiancé Stacey Jo Schugel,

for her patience, love, and faith, because she always understood.

Abstract

Self-assembly has been widely used to fabricate micro-scale three-dimensional (3D) structures for various applications like sensors, drug delivery systems, and advanced robotics (e.g., micro-actuators, micro-machines). Self-assembly is always driven by external sources (e.g., heat, solvent, pH), which makes the assembly process hard to control and leads to extremely low yield. Direct contact of heat or chemicals is usually required to trigger a self-assembly process, which limits the applications of self-assembly and decreases the manipulative capability of the process.

To address the issues of the traditional direct triggered self-assembly, my Ph.D. work involved in developing novel remote-controlled self-assembly techniques with microwave and induction energies, combining the self-assembly technique with advanced metamaterial (MM) designs, and exploring their potential applications as 3D sensors and devices. The goal of the work is to achieve advanced remotely controlled self-assembly to improve the yield and manipulative capability of the assembly process and discover new aspects of the assembly technique (e.g., biocompatible assembly, multiple and sequential assembly) and its applications (e.g., 3D sensors, 3D MM devices).

For remotely controlled self-assembly, electromagnetic waves can be remotely applied to the metal thin films within the microstructures. Eddy current can be created inside the thin films and generate heat to melt the polymeric hinges. The molten hinges generate surface tension force to transform the two-dimensional (2D) net into 3D microstructures. Induction heating can trigger self-assembly without harming live organs or tissues, which is suitable for biomedical applications.

Remote-controlled self-assembly also allows multiple and sequential self-assembly. The movements of each part of structure can be precisely controlled by adjusting the energy sources in a remote location, increasing manipulative capability of the 3D assembly process. The achievement of sequential self-assembly and multiple folding angles in a single structure is essential for building complex microstructures and micro-actuators.

One important application for remote-controlled 3D self-assembled structure is to build 3D MM devices. Split ring resonators (SRRs) and closed ring resonators (CRRs) can be patterned on each face of the self-assembled structures to achieve 3D MMs with fully anisotropic and isotropic behaviors. However, the quality factor (Q-factor) of conventional MMs is low (typically under 10), results in low sensitivity and selectivity. To increase Q-factor of the MMs, we developed novel nanopillar-based MMs driven by displacement current. The nanopillar-based MMs contain thousands of metallic nanopillars with nanoscale dielectric gaps between them. Forming the MMs with nanopillars and nano gaps decreases the Ohmic energy loss in the resonator and increases the energy storage in the dielectric nano gaps, thus an enhanced Q-factor up to 14000 can be achieved. The ultra-high Q nanopillar-based MM can be patterned on each face of the self-assembled 3D structures to realize ultra-high Q 3D MM structures.

Novel ultra-sensitive THz MMs and 3D MMs combined with remote-controlled self-assembly opens a new area of creating diverse sensors and devices for 3D optoelectronic, 3D MMs, and ultra-high sensitive biomedical sensors. This thesis will be roughly divided into two parts. We begin with part one by introducing the novel remotely controlled self-assembly using electromagnetic energies that I have developed over my

Ph.D. program as well as its unique properties and benefits over traditional self-assemblies. The second part involves my design and theory of ultra-high Q nanopillar-based MM and the 3D MM devices by combining the nanopillar-based MM with self-assembly technique.

Table of Contents

Copyright ..... **i**

Acknowledgement ..... **i**

Dedication ..... **iii**

Abstract ..... **iv**

Table of Contents ..... **vii**

List of Tables ..... **xiii**

List of Figures ..... **xiv**

List of Abbreviations ..... **xxvii**

1. History and Theory of Self-Assembly **1**

1.1 Introduction **1**

1.2 Self-assembly evolution **3**

1.2.1 Self-assembly in nature 3

1.2.2 Artificial self-assembly – Origami Art 9

1.2.3 Self-assembly of micro- and nano-structures 10

1.3 Self-assembly driving forces **14**

1.3.1 Pneumatic force-driven self-assembly 15

1.3.2 Magnetic force-driven self-assembly 15

1.3.3 Volumetric expansion-driven self-assembly 16

1.3.4 Differential thermal expansion-driven self-assembly 16

1.3.5 Surface tension-driven self-assembly 17
1.3.6 Shape memory-driven self-assembly 17
1.3.7 Thin film stress-driven self-assembly 18
1.3.8 Shrinkage-driven self-assembly 18
1.3.9 Cell traction force-driven self-assembly 19
1.4 Stimuli of self-assembly 19
1.4.1 Heat triggered self-assembly 20
1.4.2 Solvent triggered self-assembly 20
1.4.3 pH triggered self-assembly 21
1.4.4 Other triggers for self-assembly 22
1.5 Quick summary 22
2. Remotely Controlled Self-Assembly Overview 24
2.1 Current issues of direct-triggered self-assembly 24
2.2 Theory of remotely controlled self-assembly 25
2.2.1 Remotely controlled electromagnetic energy source 26
2.2.2 Eddy current generation by electromagnetic wave 29
2.2.3 Eddy current heat generation 30
2.3 Design of remotely controlled self-assembly 32
2.4 Advantages of remotely controlled self-assembly 33
3. Remote-Controlled Microwave Driven Self-Assembly 35
3.1 Theory of Microwave triggered self-assembly 35
3.2 Remotely controlled microwave system setup 38
3.3 Sample design 39

3.3.1 Anchored and anchorless design of the micro-scale structures 39
3.3.2 Substrate selection 41
3.4 Fabrication process 42
3.4.1 Anchored structures 42
3.4.2 Anchorless structures 44
3.5 Hinge reflow analysis 45
3.6 Self-assembly of cubic structures 48
3.6.1 Anchored structures 48
3.6.2 Anchorless structures 49
3.7 Folding analysis 50
3.8 Multiple and sequential assembly 52
3.8.1 Multiple and sequential assembly theories 52
3.8.2 Sample design 53
3.8.3 Folding angle analysis 53
3.8.4 Advantages of multiple and sequential assembly 54
4. Remote-Controlled Induction Driven Self-Assembly 56
4.1 Theory of induction driven self-assembly 56
4.1.1 Induction induced eddy current 57
4.1.2 Eddy current driven self-assembly 58
4.2 Induction system setup 60
4.3 Sample design and fabrication 61
4.3.1 Substrate, panels, and hinges 61
4.3.2 Fabrication process 62

4.4 Thermal analysis..... 63

4.4.1 Surface temperature modeling overview..... 63

4.4.2 Surface temperatures with different film thickness..... 64

4.4.3 Surface temperatures with different panel areas 65

4.4.4 Surface temperatures with different induction powers..... 65

4.5 Self-assembly of cubic structures 69

4.5.1 Overview 69

4.5.2 Folding angle and angular speed analysis 70

4.6 Reticulum beef tripe experiment..... 72

4.6.1 Beef tripe experiment overview 72

4.6.2 Self-assembly in beef tripe 73

4.6.3 Thermal analysis..... 73

4.7 Ladybug experiment 75

4.7.1 Ladybug experiment overview 75

4.7.2 Self-assembly with ladybug 75

4.7.3 Thermal analysis..... 76

4.7.4 Advantages 76

5. 3D Metamaterial and Self-Assembly 79

5.1 Background of Metamaterial 79

5.1.1 Overview 79

5.1.2 Types of metamaterials 80

5.2 Split Ring Resonator (SRR) Metamaterials..... 82

5.2.1 Overview 82

5.2.2 Electric and magnetic responses 83
5.2.3 Quality factor of SRRs 84
5.3 3D Metamaterials 85
5.3.1 Overview 85
5.3.2 Drawbacks of 2D MMs 85
5.3.3 3D asymmetric metamaterial 87
5.4 Self-assembled 3D Metamaterials 88
5.4.1 Overview 88
5.4.2 Fabrication strategies 88
5.4.3 3D isotropic metamaterials 90
6. Advanced THz Metamaterial 93
6.1 Drawbacks of existing metamaterials 93
6.1.1 Sensitivity 93
6.1.2 Frequency shift 94
6.1.3 Selectivity 95
6.2 Nanopillar-based SRR metamaterials 95
6.2.1 Design of nanopillar-based SRRs 95
6.2.2 Electromagnetic induced displacement current 96
6.2.3 Geometric configurations and parameters 97
6.2.4 Resonant behaviors 98
6.3 Transmission and frequency responses 101
6.4 Quality factor analysis 104
6.5 Film- and nanopillar-based SRRs Comparisons 107

6.6 Fabrication process and measurements 110

6.6.1 Fabrication process 110

6.6.2 Measurement 112

6.7 Nanopillar-based closed ring resonators 116

6.7.1 Overview 116

6.7.2 Theory 118

6.7.3 Fabrication process 120

6.7.4 Transmission and frequency comparison 121

6.7.5 Ultra-high quality factor 125

6.7.6 Nanopillar configuration discussion 128

6.7.7 Example of high Q 3D MM – electromagnetic cloaking 132

7. 3D Self-Assembled Nanopillar-Based Metamaterials 137

7.1 Design of nanopillar-based 3D metamaterials 137

7.1.1 Overview 137

7.1.2 Fabrication strategy 138

7.1.3 Transmission responses 140

7.2 Frequency shifts 143

8. Conclusion 144

8.1 Looking behind 144

8.2 Looking ahead 146

Bibliography 147

Appendix A 183

List of Tables

Table 1.1 Self-assembly driving forces and stimuli 23

Table 3.1 Comparison between anchored and anchorless self-assembly 41

List of Figures

Figure 1.1 Examples of self-assembly in the natural world. (a) Self-assembly of stars, particles, clouds, and molecular gases into the Pinwheel galaxy M101 [16]. (b) Self-assembly of atoms into DNA double helix [23]. 2

Figure 1.2 Crystallizations of salt and ice. (a) Crystal lattice of salt (NaCl) [44]; (b) Crystal lattice of ice [45]; (c) macroscopic shape of salt crystals [46]; (d) macroscopic shape of ice crystals [47]. 4

Figure 1.3 No two snowflakes are alike. Different shapes of the ice crystal depend on the environmental condition during ice crystal growth [53]. 6

Figure 1.4 Pinecone structure self-assembly: (a) bilayer of the pinecone scale consists of CMF tissues aligned or perpendicular to the length of the scale; (b) Pinecone opens and closes triggered by water. [54] 7

Figure 1.5 Self-assembly of Venus flytrap leaves. The self-assembly of the leaves is triggered by the touching of the hairs on the leaves [62]. 9

Figure 1.6 Japanese art of folding papers – Origami. Origami uses different folding techniques to transfer a piece of paper into 3D structures (a) Valley folding (b) Crease folding (c) Mountain folding. (d) Illustration of the origami paper folding process of making a flapping bird. [68] 10

Figure 1.7 Self-assembly in micro-scale. The micro-scale structure contains two rigid panels and one hinge connected between them. Heat triggers the hinge to melt and generate surface tension stress to lift up the panels..... 11

Figure 1.8 Self-assembly of nano-scale structures. Ni thin films with nano-scale dimensions are curving up due to the stress induced during Tin grain coalescence.. 13

Figure 2.1 Remotely controlled self-assembly triggered by LED lights with different wavelengths (blue and red in color). Hinges with different colors can selectively absorb lights with different wavelengths, results in selective self-assembly of the structures [165]. 26

Figure 2.2 Remotely controlled self-assembly using electromagnetic energy 27

Figure 2.3 Eddy current (*I*) generation by electromagnetic field (*H*) inside metal thin films. 30

Figure 2.4 Eddy current heat generation. Eddy current (*I*) inside the metal thin film flows against the resistance (*R*) of the thin film, which results in Joule heating. 32

Figure 3.1 Illustration of remotely controlled 3D self-assembly using microwave Energy [161]. (a) Heat power generation within a Cr thin film via eddy current looping in the Cr film against the resistance of the Cr. The eddy current is induced by electromagnetic waves generated by a magnetron. Self-assembly of cubic structures consisted of a nano-scale Cr film, SU-8 panels, (b) PCL hinges and (c) SPR-220 hinges. Hinges are melted due to heat generation within Cr, inducing surface tension force on the hinges, leading to self-assembly. (d) A microwave system for remote-controlled self-assembly. Generated microwave energy is applied to the sample through a waveguide in a remote location without physical contact, inducing heat generation for self-assembly. 37

Figure 3.2 A microwave system for remote-controlled self-assembly [161]. Generated microwave energy is applied to the sample through a waveguide in a remote location without physical contact, inducing heat generation for self-assembly. 38

Figure 3.3 Fabrication of cubic structures for self-assembly on substrate [161]. (a-h) Illustration of the fabrication process of cubic structures on a glass substrate. (i-k) Optical images of a 2D micro structure (i), a half-folded micro structure (j), and a folded micro structure (k). (h) Optical image of a cubic structure array folded using remote-controlled microwave energy. 43

Figure 3.4 Fabricated of cubic structures for substrate-free self-assembly [161]. (a-h) Illustration of the fabrication process of cubic structures for substrate-free self-assembly. (i-k) Optical images of a 100 nm thick Cr pattern (i), SU-8 panels (j), and a 2D micro structure on paper (k). (h) Optical image of a cubic structure array folded using substrate-free remote-controlled microwave energy. 45

Figure 3.5 Hinge reflow and surface temperature analysis of micro-structures [161]. (a-d) Top view of the reflow process of 24 μm thick SPR-220 photoresist hinges with microwave exposure time from 0 sec to 15 sec. (e-h) Cross-section view of the corresponding hinge reflow shown in (a-d). Contact angle of the SPR-220 hinge varies from 65^{o} to 35^{o}. (i-l) Surface temperatures of the 20 nm thick Cr film were captured using an infrared camera. (m) Surface temperature, (n) heat power generation, and (o) thermal energy generating within the 20 nm Cr film with different microwave exposure time were modeled and measured. 47

Figure 3.6 Micro-scale 3D cubic structures for remote-controlled self-assembly [161]. (a-c) Real-time self-assembly process images of the cubic structures on a glass/ 20 nm thick Cr substrate. Images are captured using an optical microscope and camera at different microwave exposure time of (a) 0, (b) 0.5 t, and (c) t. (d-f) Zoomed-in optical images of a micro-structure shown in (a-b). (d) A 2D, (e) a half-way folded,

and (f) a fully folded cubic structure are captured. (g) Optical image of an anchorless folded cubic structure with a 100 nm thick Cr film on the surface of SU-8 panels... 49

Figure 3.7 Folding angle analysis with different Cr thicknesses [161]. (a-d) Real-time optical images of self-assembly on glass substrate with 20 nm Cr. (e) Folding angle and (f) angular speed of cubic structure with different Cr thicknesses (10 nm, 15 nm and 20 nm) were modeled and measured. (g) Folding angles of cubic structure with a 20 nm Cr film at different temperatures. The angles vs. temperatures modeled from equation (2) shows a good agreement with measurements. 52

Figure 3.8 Remote-controlled self-assembly with multiple folding configurations [161]. (a-c) Illustration of self-assembly with multiple hinges. (a) Cr with different thicknesses (10 nm, 50 nm and 100 nm) were patterned adjacent to the PCL hinges on top of SU-8 Panels. (b) Different amounts of heat are generated from the Cr depending on its thicknesses. (c) Self-assembled structures with different folding configurations show multiple folding angles. (d, e) Optical images show the micro structure with (d) multiple hinges before assembly and (e) the folded structures with multiple folding angles. (f) Measurement data shows different folding angles of the panels corresponding to different Cr thicknesses. 55

Figure 4.1 Illustration of induction driven self-assembly for biomedical applications. (a) Induction coil generates high frequency magnetic field penetrating through the sample on a paper substrate. (b) The magnetic field (blue line) creates eddy current (red line) in the Ni panels of the sample. The eddy current flows against the resistance of the Ni and generates heat. 58

Figure 4.2 Eddy current driven self-assembly (a) A cross-section of the structure shows the Ni panels, PCL hinges and Al_2O_3 supporting layer. The magnetic field (blue line) penetrates through the sample. (b) Heat is generated due to the eddy current, which melts the PCL hinges. The molten hinge creates surface tension stress to lift up the panels. (c) A totally self-assembled structure. 59

Figure 4.3 Induction system setup for the induction driven self-assembly. 61

Figure 4.4 Fabrication details of the micro-scale structures for induction driven remotely controlled self-assembly. 63

Figure 4.5 Thermal analysis of the induction heating process for remotely controlled self-assembly 68

Figure 4.6 COMSOL modeling of the induction heating process for the remotely controlled self-assembly. 69

Figure 4.7 Remotely controlled self-assembly of micro-scale cubic structures using induction energies..... 72

Figure 4.8 Reticulum beef tripe experiments for induction driven self-assembly. (A-D) Illustration of the induction driven self-assembly on beef tripe. (A) Magnetic field is generated using an induction coil. (B) The coil temperature remains low due to the water-cooling system. A beef tripe is placed on top of the coil as a substrate. The sample to be self-assembled is placed on the beef tripe. (C) Magnetic field penetrates through the beef tripe and reaches the Ni panels of the sample. The eddy current is generated inside the Ni panels and produce heat. (D) Heat melts the PCL hinges and triggers the self-assembly process. (E) A honeycomb structure of the reticulum beef tripe. (F) A 5 face 2D structure placed in one of the honeycomb beef tripe chamber.

(G) A self-assembled cubic structure in the beef tripe chamber. (H-J) infrared images of the beef tripe and the sample during the self-assembly process. The surface temperature of the beef tripe remains at low temperature of around 10 ºC and the surface temperature of the sample increases from (H) 20 ºC to (J) 55 ºC during the self-assembly process. 74

Figure 4.9 Ladybug experiment for the induction driven self-assembly. (A-C) Real-time optical image of the self-assembly process with a live ladybug placed close to the sample. The ladybug remains undisturbed during the self-assembly process (D-F) Infrared images of the ladybug and the sample during the self-assembly process. The surface temperature of the ladybug remains at around 20 ºC. The surface temperature of the sample increases from (D) 20 ºC to (F) 55 ºC during the self-assembly process. (G) Surface temperature of the ladybug (black line) and the sample (red line) at different induction radiation time from 0 sec to 25 sec. (H) Surface temperature of the ladybug remains at 20 ºC at different sample temperatures. 77

Figure 5.1 An example of a MM system consists of periodic metallic resonators and dielectric substrates. Each resonator/substrate component interacts with the electromagnetic wave and exhibits unique electromagnetic properties [228]..... 80

Figure 5.2 An example of electromagnetic cloaking using electromagnetic MMs..... 81

Figure 5.3 Traditional film-based SRRs [245]. (a) Schematic of film-based SRR. (b) Simulated transmission spectrum of film-based SRRs with three resonant modes. (c) Measured transmission spectrum of film-based SRRs with three resonant modes. (d-f) Images of film-based SRR array under an optical microscope. The dimension of film-based SRR is 36um*36um. The width of SRR arm is 4um and the split of the

SRR is 4um. The film-based SRR is made of Au using electroplating process and the thickness of the deposited Au is around 300 nm. 83

Figure 5.4 Electric and magnetic responses of SRR. (a) Electric response of the SRR with electric field (*E*) parallel to the split. (b) Magnetic response of the SRR with electric field (*E*) perpendicular to the split. 84

Figure 5.5 Comparison between 2D MMs and 3D MMs. 86

Figure 5.6 3D asymmetric cubic SRR MM [225]. 87

Figure 5.7 Fabrication process of 3D asymmetric SRR MM [225]. 89

Figure 5.8 Self-assembled 3D asymmetric MM structure [225]. 90

Figure 5.9 3D X-shape MM shows fully isotropic behaviors. (a) A traditional 3D CRR MM (b) A novel 3D Octagram MM with X-shape resonators on each face of the cubic structure (c) The resonant frequency comparison between 3D CRR MM and 3D Octagram MM at different rotation angles. 91

Figure 5.10 Fabrication of 3D X-shape MM [224]. 92

Figure 6.1 Illustration and SEM images of nanopillar-based MMs utilizing displacement current [245]. (a) Displacement current (I_d) induced between two conducting plates with time-dependent electric field (*E*) generated by separated charges (+*q* and -*q*). (b) Displacement current (I_d) induced between two metallic nanopillars. This displacement current is derived from the same concept as displacement current between two plates. (c) Nanopillar arrays with different configurations (circle, hexagon and square). (d) SEM images of circular nanopillar-based SRR array. Each SRR is formed by thousands of Au nanopillars fabricated using an anodic aluminum oxide template. (e) Schematic of square-nanopillar-based SRR. The geometry and a

material property are defined by the height (H), width (l), interface area (A), nano-gap size (d) and permittivity (ε). (f) Simulated transmission spectra of a nanopillar-based SRR (with split size of 4 um, SRR length of 36 um, and SRR arm width of 4 um) and the surface current distributions at the first three resonant frequencies. First mode (ω_1) and third mode (ω_3) of the SRR are for the electric field parallel to the split, while second mode (ω_2) is for the electric field perpendicular to the split. 101

Figure 6.2 Transmission properties of nanopillar-based SRRs with varied parameters [245]. First modes (ω_1) of nanopillar-based SRRs in transmission spectra were obtained by simulation. Influences of (a) nano gap size of SRRs and (b) height of SRRs on transmission amplitude. Transmission amplitude of nanopillar-based SRRs with varied nano-gap size, (c) permittivity, and (d) height. 103

Figure 6.3 Q-factor characterization of nanopillar-based SRRs with varied parameters [245]. The Q-factors of thin-film-based SRRs (nano-gap size = 0 nm) are also presented in the figures. The nano-gap size varies from 5 nm to 25 nm for each simulation and Q-factor of both first mode (ω_1) and third mode (ω_3) of nanopillar-based SRRs are shown. The dependence of Q-factor of nanopillar-based SRRs on (a) the height of nanopillars, (b) permittivity of the nano-gaps and (c) the width of nanopillars. A maximum Q-factor of nanopillar-based SRRs of more than 450 is observed which is more than 32 times higher than that of thin-film-based SRRs. .. 106

Figure 6.4 Characterization of resonant frequency shifts using simulation [245]. (a) Resonant frequency (ω_1) shifts of nanopillar-based SRRs and film-based SRRs on transmission spectrum with varied permittivities (ε = 1, 2.5, 5 and 9.8). (b) Quantitative comparison (histogram) of the resonant frequency shift between

nanopillar-based SRRs (red bars) and film-based SRRs (black bars) with 4 different permittivity intervals. 109

Figure 6.5 Fabrication scheme and experimental characterization of slit-based SRRs [245]. (a-d) Fabrication scheme of slit-based SRRs, which involves (a) electroplating deposition of first Au slit layer on high-resistive Si substrate and (b) ALD of nano-scale Al_2O_3 layer followed by electroplating deposition of second Au slit layer. (c, d) Nano gap is defined by ALD Al_2O_3 (blue) between two Au slit layers (yellow). Al_2O_3 can also be removed using wet etching process to make air gaps between Au slits. (e-h) SEM images of slit-based SRR array with 10 nm nano gaps between Au slits. Simulated (i) and measured (j) transmission spectra of slit-based SRRs with 10 nm Al_2O_3 gaps clearly show three resonant modes. Simulated (k) and measured (l) transmission spectra of slit-based SRRs with 10 nm vacuum gaps also show three resonant modes. Both measured spectra match with simulation results. The measurement is performed using THz time-domain spectroscopy in Los Alamos National Laboratory. 111

Figure 6.6 Details of the fabrication process of slit-based SRRs [245]. (a, e) High-resistive (560 - 840 Ohm·cm) Si substrate. (b, f) 5 nm Cr and 10 nm Cu deposited on Si substrate using an E-beam evaporation process. (c, g) 400 nm thick Au slits (the width of the Au slit is 2 μm and the length of the slit is 4 μm) patterned on Cu layer using photolithography and electroplating process. (d, h) Cr and Cu were etched away using wet etching process followed by deposition of 5 nm Al_2O_3 between each Au slit (Blue color in schematic) with an ALD system. (i, m) Another 5 nm Cr and 10 nm Cu layer deposited on top of Au and Al_2O_3 using an E-beam evaporation process.

Since E-Beam evaporation was used to directly deposit Cr and Cu without rotating the sample, Cr and Cu are only deposited on the top surface of the structure. (j, n) An Au electroplating process was used to deposit a second layer of Au between the first Au slits to form Al_2O_3 nano-gaps between first and second layers of Au. (k, o) Cr and Cu on top of the sample were etched away using a wet etching process. (l, p) An additional layer of Au was deposited to fully fill the gap between two Au layers. (q, u) SRR C-shape was patterned with S1813 photoresist on top of the sample using photolithography process. (r, v) Au outside the C-shape was etched away using an ion milling process. (s, w) S1813 photoresist was removed using acetone completing the fabrication of the slit-based SRR with 5 nm Al_2O_3 nano gaps (t, x) Al_2O_3 can be further etched away using HF solution to create air nano gaps. (y) An optical image of first layer of Au slits on Si substrate. (z) An optical image of the second layer of Au deposited between first Au slits. (aa) An optical mage of SRR C-shape comprised of S1813 photoresist on top of the sample. (ab) A slit-based-SRR array after ion milling process. (ac) A zoomed-in optical image of single slit-based SRR. (ad) A SEM image of first layer of Au slits deposited on Si substrate. (ae) A SEM image of the second layer of Au deposited between the first Au slits. (af) A cross-sectional SEM image of slit-based SRRs after an ion milling process. (ag) A SEM images showing 5 nm gap between two Au slits. 114

Figure 6.7 Illustration of nanopillar-based CRR. (a) An array of nanopillar-based CRR. (b) A single nanopillar-based CRR. (c) The Au nanopillars and nano gaps between them. (d) Film-based CRR and (e) nanopillar-based CRR with different configurable

parameters. (f) Transmission spectra of both film and nanopillar-based CRRs. Electric field distribution of (g) film-based CRR and (h, i) nanopillar-based CRR. 119

Figure 6.8 Fabrication process of the nanopillar-based CRRs. (a-d) Fabrication of nanopillar-based CRRs using E-beam lithography, E-beam evaporation and lift-off methods. (e) A SEM image of an array of nanopillar-based CRRs. (f) A SEM image of a single nanopillar-based CRR. (g) A SEM image of an array of Au nanopillars. (h) A SEM image shows the 50 nm gap between two Au nanopillars..... 121

Figure 6.9 Transmission analysis of the nanopillar-based CRRs. (a-d) Transmission spectra of nanopillar-based CRRs with (a) different nano gap size, (b) different nanopillar thickness, (c) different nanopillar diameter, and (d) different permittivity. (e-h) Resonant frequency and magnitude comparisons of the nanopillar-based CRRs with (e) different nano gap size, (f) different nanopillar thickness, (g) different nanopillar diameter, and (h) different permittivity..... 125

Figure 6.10 Q-factor analysis of the nanopillar-based CRRs. (a, b) Q-factors of the nanopillar-based CRRs with different nanopillar thicknesses. (c, d) Q-factors of the nanopillar-based CRRs with different nanopillar diameters. (e, f) Q-factors of the nanopillar-based CRRs with different permittivity. 127

Figure 6.11 Nanopillar shape and configuration analysis. (a-d) Different nanopillar shapes of (a) circle, (b) square, (c) triangle, and (d) hexagon. (e) Total volume of the nanopillar and Q-factor of the nanopillar-based CRR with different nanopillar shapes. (f) Q-factor of the nanopillar-based CRR with different nanopillar shapes at different nano gap sizes. (g) A 3D plot of the Q-factors with different nano gap sizes and different total volume of the nanopillars. Different configurations of the nanopillars

with (h) aligned and (i) zigzag nanopillars. (j) Top view of the aligned and zigzag nanopillars and the current flow direction. (k) Q-factor of the nanopillar-based CRR with different nanopillar configurations. (l) Total capacitance of the nanopillar-based CRRs with different nanopillar configurations. (m) Q-factor difference between the aligned and the zigzag nanopillar-based CRRs at different nano gap sizes. (n) Comparison between Q-factor difference and total capacitance difference of the aligned and zigzag nanopillar-based CRRs at different nano gap sizes. 131

Figure 6.12 Electromagnetic cloaking using 3D MM designs. (a) 3D cloaking shell structure with inner radius R1 and outer radius R2. (b) The cloaking structure can be made of array of MMs (e.g., CRRs). (c) The CRR is made of Au ring with a length *L*, a width *W*, and a thickness *H*. 133

Figure 6.13 Modeled Electric field across the MM cloak with different Q-factor values of the MM. The electromagnetic field flows from the bottom of the field (Y = 0 mm) towards to the top of the field (Y = 1000 mm). (a) MM cloak with a Q of 10. (b) MM cloak with a Q of 30. (c) MM cloak with a Q of 100. (d) MM cloak with a Q of 1000. 135

Figure 6.14 Electric field amplitude comparison before and after the electromagnetic wave enters the cloak with different Q-factors..... 136

Figure 7.1 3D nanopillar-based X-shape MM using self-assembly technique. 138

Figure 7.2 Fabrication of 3D nanopillar-based MM using self-assembly process. 139

Figure 7.3 Comparison between 3D nanopillar-based MM and 3D film-based MM. (a) Illustration of the 3D nanopillar-based MM with X-shape nanopillar-based resonators patterned on each face of the 3D cubic structure. (b) An illustration of the

displacement current generated within the Au nanopillars. (c) Transmission spectrum shows the resonant peaks of 3D nanopillar-based MM (blue solid line) and 3D film-based MM (red dashed line). The Q-factor of the 3D nanopillar-based MM is around 9000 while the Q-factor of the film-based MM is around 30. 141

Figure 7.4 3D X-shape MM and its characters. (a) Illustration of the rotation axis of the 3D structure. (b) Resonant frequency comparison of the film-based 3D X-shape MM and the 3D nanopillar-based X-shape MM. (c) Resonant Magnitude comparison of the film-based 3D X-shape MM and the 3D nanopillar-based X-shape MM. (d) Q-factor comparison of the film-based 3D X-shape MM and the 3D nanopillar-based X-shape MM. 142

Figure 7.5 Frequency comparisons between film-based 3D X-shape MM and nanopillar-based 3D X-shape MM..... 143

List of Abbreviations

2D: two-dimensional

3D: three-dimensional

Al2O3: aluminum oxide

ALD: atomic layer deposition

ASR: asymmetric split resonator

Au: gold

Cr: chromium

CRR: closed ring resonator

Cu: copper

CMF: stiff cellulose microfibril

$Cl_2CHCHCl_2$: tetrachloroethane

DI: deionized

DNA: deoxyribonucleic Acid

EEMR: electric field excited magnetic response

EMF: electromotive force

ER: electric field excited response

FDTD: finite-difference time-domain

LC: inductive-capacitive

MM: metamaterial

Ni: nickel

NaCl: sodium chloride

NIPAm: N-isopropyl-acrylamide

PCL: polycaprolactone

Q-factor: quality factor

RIE: reactive ion etching

SEM: scanning electron microscope

Si: silicon

SRR: split ring resonator

Sn: tin

SMAs: shape memory alloys

THz: terahertz

Chapter 1

History and Theory of Self-Assembly

1.1 Introduction

"*Self-assembly refers to the spontaneous formation of organized structures through a stochastic process that involves pre-existing components, and can be controlled by proper design of the components, environment, and the driving force*". John A. Pelesko at University of Delaware defined self-assembly as such in his book "Self Assembly: The Science of Things That Put Themselves Together" published in 2007 [1]. This definition of self-assembly tells us all the information and essential elements of self-assembly. "*Spontaneous formation*" shows that the process is self-directed and self-controlled without any excessive external assistance. "*Pre-existing*" distinguishes the difference between self-assembly and patterning as the latter does not have any "*pre-existing*" components. Formation of "*Organized structures*" from a "*stochastic*" stage indicates that the self-assembly process well designed and organized while "*proper design of the components*", "*environment*", and "*driving force*" emphasize on the necessary components to realize the self-assembly process [2-6].

Self-assembly may sound like a technical term that only exists in science and research. However, as we dig through the definitions of self-assembly, we can find self-assembly in every aspect of our lives [7-12]. Self-assembly can be as large as the formation of the galaxy millions of light years away from us and as small as the

Deoxyribonucleic Acid (DNA) double helix that is in the human body [13, 14]. Figure 1.1a shows the Pinwheel Galaxy M101, which was first discovered in 1781 by Pierre Méchain [15, 16]. The M101 galaxy contains around a trillion of stars, particles, clouds, and molecular gases. Under the influences of gravities and interactions between the starts, they manage to self-assemble into a well-organized spiral structure with a diameter of 170,000 light years [17-20]. Figure 1.1b illustrates the fundamental element of all known forms of life – DNA [21-23]. From a single atom to the two complementary nitrogenous bases of DNA strands and to the double helix structure, DNAs allow themselves to be self-assembled and organized perfectly so that important generic information can be stored and passed down from generations to generations [24-30].

Figure 1.1 Examples of self-assembly in the natural world. (a) Self-assembly of stars, particles, clouds, and molecular gases into the Pinwheel galaxy M101 [16]. (b) Self-assembly of atoms into DNA double helix [23].

Besides these two extreme examples of self-assembly, almost every aspect of our lives contains certain degrees of self-assembly, especially from the natural world. In the

rest of the chapter, we will look at a few self-assembly examples in the nature and see how artists and engineers attempt to mimic the natural self-assembly and create their own self-assembly in the micro- and nano- world.

1.2 Self-assembly evolution

1.2.1 Self-assembly in nature

Self-assembly in nature is the most common phenomenon and is extremely important for studying and understanding the fundamentals of self-assembly of artificial and engineered structures [8, 31]. Needless to say, self-assembled structures in nature are way complex and advanced compared to the ones created by artists, scientists and engineers. However, understanding the interconnection between natural self-assembly and engineered self-assembly allow us to create structures, devices and machines that will share similar characteristics as the natural structures and even have functions that the natural structure does not have [32-37]. In the next few sections, we will look at 3 self-assembly examples in the natural world: (i) Crystallization of salt crystals and ice crystals (ii) reversible self-assembly of pinecone reinforcement structure for pine seed dispersal; (iii) self-assembly of Venus flytrap leaves for predation. (J. H. Cho, Nanotechnology for Self-Assembly, Class lecture, University of Minnesota, Minneapolis, MN, Spring 2016)

1.2.1.1 Crystallization of salt and ice crystals

Crystal is a solid whose microscopic components are well orientated by a crystal lattice [38]. The macroscopic shape of the crystal follows the shape of the crystal lattice and can extend towards all directions of the lattice [39]. The most common crystals are salt (sodium chloride, NaCl) and ice [41-43]. The crystal of salt and ice are shown in figure 1.2a and figure 1.2b respectively. The macroscopic shapes of salt and ice are shown in figure 1.2c and 1.2d for comparison.

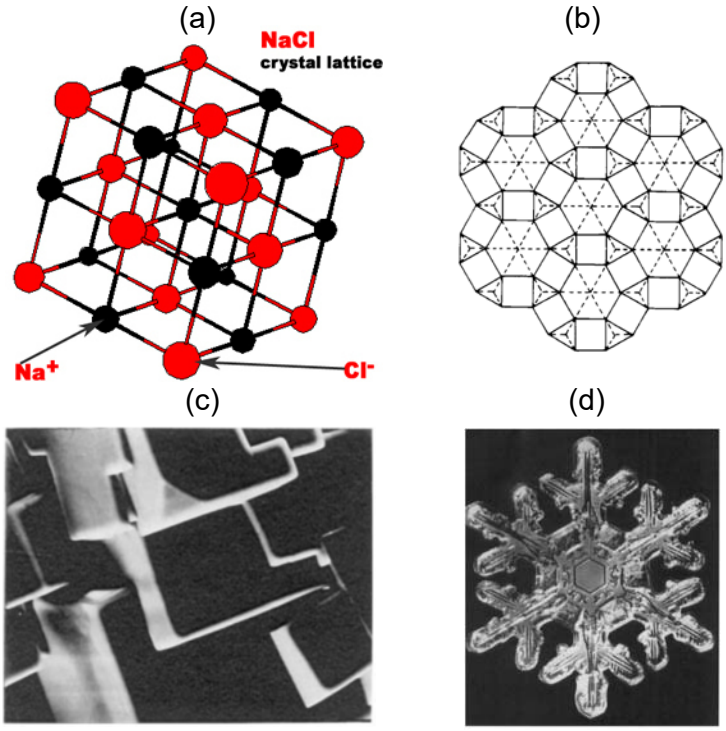

Figure 1.2 Crystallizations of salt and ice. (a) Crystal lattice of salt (NaCl) [44]; (b) Crystal lattice of ice [45]; (c) macroscopic shape of salt crystals [46]; (d) macroscopic shape of ice crystals [47].

The crystallization process can be viewed as a self-assembly process. Considering a bowl of oversaturated salt water, the NaCl molecules in the salt water were initially disordered. When the water started to evaporate, the first salt crystal lattice shows up. The

disordered molecules in the salt water will spontaneously self-assembled to the organized salt crystal, resulting in the growth of the crystal while maintaining its original lattice shape. This crystallization process is the self-assembly of salt molecules from disordered stages in the water to an organized crystal state [48]. The driving force behind the self-assembly is thermodynamics: the atoms or molecules approaching the crystal lattice are seeking for the most stable energy equilibrium stage, which is when the atoms or molecules are aligned with the crystal lattice [49]. The atoms or molecules will fill up the voids of the crystal and form an outer layer of the crystal. The same process repeats and eventually a well-organized crystal is self-assembled layer by layer.

For ice crystal formation, the situation is slightly complicated. As seen in figure 1.2b, the crystal lattice of ice is in a shape of hexagon. A nucleus is first formed by the water droplet frozen on a dust or particle [50]. The initial shape of the ice crystal is hexagon, which followed the crystal lattice shape of the ice. As the ice nucleus continues to be exposed to the air, water vapors start to deposit on to the surface of the ice nucleus. Since the 6 corners of the hexagonal ice nucleus have larger contact with the water vapors in the air, the ice crystals at the corners grows faster than the rest of the ice nucleus, results in the final shape of the ice crystal [50]. The shape of the ice crystal is highly symmetric thanks to the perfect self-assembly process during the growth of the ice crystal [51, 52]. It is worth mention that not all ice crystals shapes the same. This is because the environmental conditions largely affect the crystal formation. With different humidity and temperatures, the ice crystal growth is also different, leading to various shapes of the ice crystals. Figure 1.3 shows different shapes of the snowflakes due to different temperature

and humidity in the atmosphere. However, exactly how environmental changes affect the shape of the ice crystal remains a mystery [53].

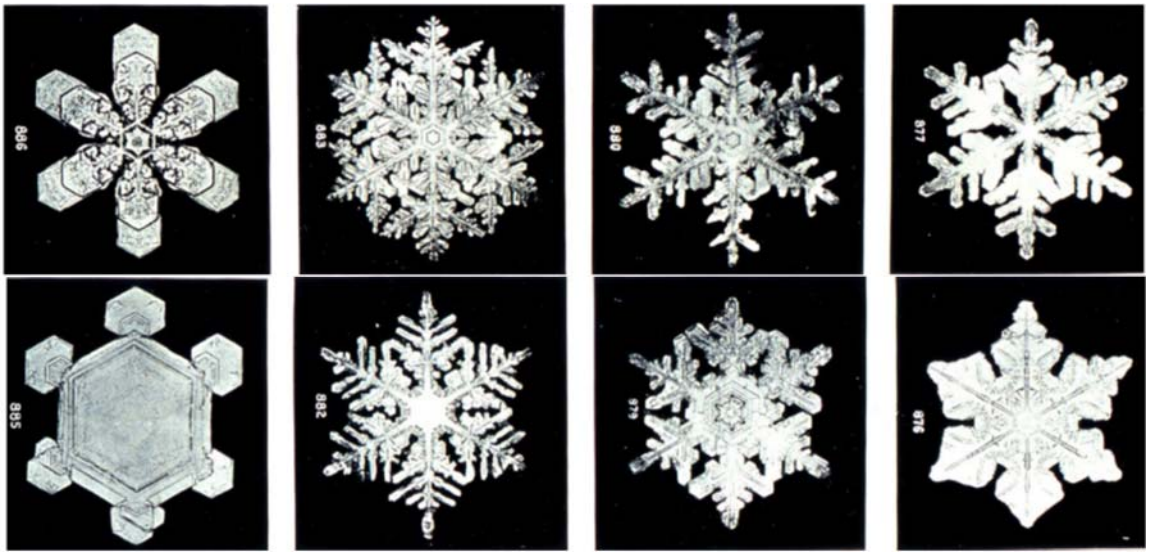

Figure 1.3 No two snowflakes are alike. Different shapes of the ice crystal depend on the environmental condition during ice crystal growth [53].

1.2.1.2 Self-assembly of pinecones

Pinecone is one of the masterpieces that the nature made to show us how self-assembly works to benefit living organisms and maintain their reproduction and proliferation [54]. Pinecone is a reinforced structure whose main purpose is to protect the pine seeds and guarantee that the seeds are properly dispersed [55-58]. In order to guarantee a long distance seed dispersal, the seed dispersal needs to be done in a dry and windy weather condition. Pinecone is thus evolved to become a self-assembly structure using water precipitation or humidity as a trigger. The scale of the pinecone is a bilayer consists of tissues called stiff cellulose microfibril (CMF) [59, 60]. In the top layer of the pinecone scale, the CMF tissues are aligned along the length of the scale while in the

bottom layer of the pinecone scale, the CMF tissues are perpendicular to length of the scale (figure 1.4a). The bottom layer of the scale tends to expand and shrink more along the length of the scale compared to the top layer due to the perpendicular aligned CMF tissues. Upon wetting the scale, the bottom layer swells faster than the top layer, bending the scale upwards to protect the seeds inside the pinecone. Upon drying, the bottom layer shrinks fasters than the top layer, bending the scale downwards to release the seeds into the air for longer seed dispersal (figure 1.4b). This open and close process of the pinecone illustrates a perfect self-assembly actuator that is triggered with different environmental conditions (water and humidity) [59, 60].

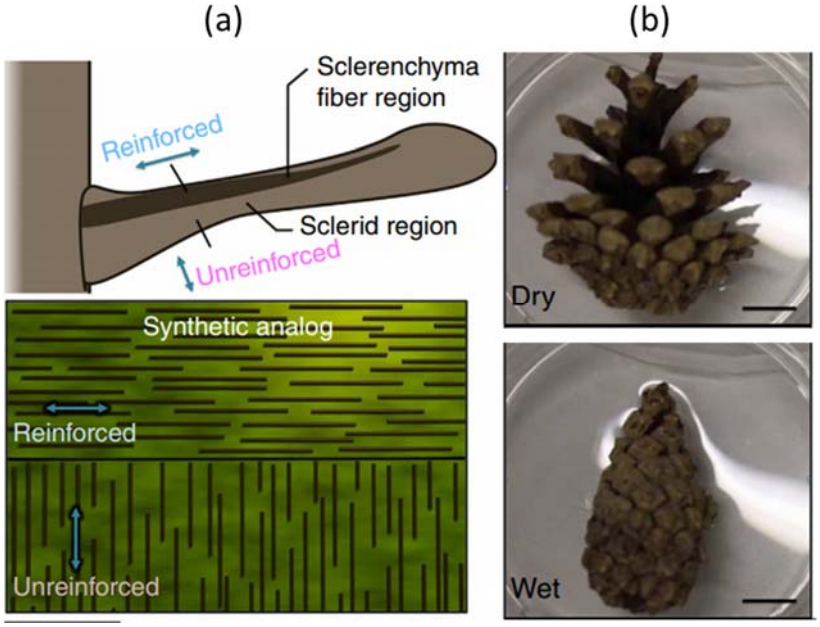

Figure 1.4 Pinecone structure self-assembly: (a) bilayer of the pinecone scale consists of CMF tissues aligned or perpendicular to the length of the scale; (b) Pinecone opens and closes triggered by water. [54]

1.2.1.3 Self-assembly of Venus flytrap

Venus flytrap is another example of self-assembly actuator in nature [61]. The leaves of the flytrap contain small sensitive hairs. When the hairs are touch by insects crawling on the leaves, an electric signal is sent to the lower cells of the midrib. The signal triggered the hydrogen ions (H^+) to move out of the cells. Hydrogen ions (H^+) make the space outside the cells more acid and dissolve Calcium (Ca^{++}), results in a softer tissue in the leaves. Since the Calcium concentration inside the cell increases, more water gets absorbed inside the cell and makes the leaves expand. Once the signal is no longer exist, the Hydrogen ions moves back into the cells and shrinks the leaves. The expanding and shrinking motions of the leaves is a self-assembly process which folds and unfolds the leaves in just about 100 ms. The self-assembly of Venus flytrap leaves clearly shows its significance towards the variety and complexity of the nature [62].

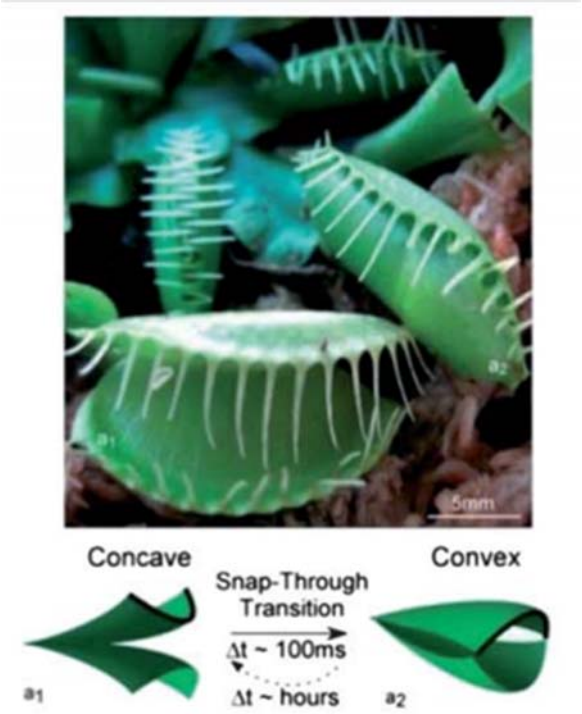

Figure 1.5 Self-assembly of Venus flytrap leaves. The self-assembly of the leaves is triggered by the touching of the hairs on the leaves [62].

1.2.2 Artificial self-assembly – Origami Art

It is not difficult to notice that there are many man-made structures and ideas that shares similar characters as the self-assembly in the natural world. One of the most attractive artificial structures is the Japanese art of folding papers – Origami [63, 64]. The word "*Origami*" came from "*Ori*" meaning folding in Japanese and "*kami*" meaning paper in Japanese [65]. Origami is an art, also a technique to transform a piece of flat paper into various structures that represent objects that we see in our daily lives. Origami uses different folding techniques (e.g., valley fold, mountain fold, cushion fold, squash fold, square folding, etc.) to achieve the proposed shapes (figure 1.6a-1.6c) [66, 67, 68]. We can

see the similarities between self-assembly and Origami (figure 1.6d): (i) both of them starts from a pre-existing component; (ii) Both of them experience environmental changes or triggered by a driving force; (iii) Both of them have an organized final form.

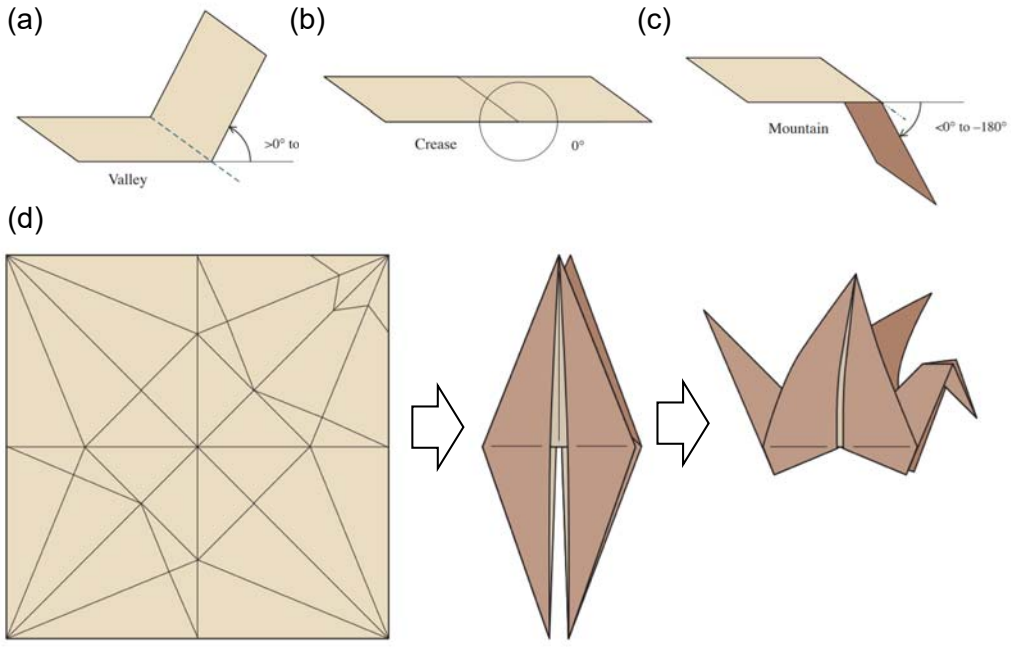

Figure 1.6 Japanese art of folding papers – Origami. Origami uses different folding techniques to transfer a piece of paper into 3D structures (a) Valley folding (b) Crease folding (c) Mountain folding. (d) Illustration of the origami paper folding process of making a flapping bird. [68]

1.2.3 Self-assembly of micro- and nano-structures

Even though Origami closely follows the example of self-assembly in nature, the driving force of the Origami (with the use of hands) extremely limits the capability and applications of the Origami. For example, the traditional Origami will not work properly if

the desired structure is smaller than what hands can control. In addition, complex Origami structures require people with experienced skills to accomplish, which is not always available. Despite the disadvantages of the Origami self-assembly, researchers and scientists are inspired by the Origami and endeavor to develop novel self-assembly technique to fit the self-assembled structures into the micro and nano world.

A simple and typical micro-scale self-assembly inspired by Origami involved in two rigid panels and a hinge (shown in figure 1.7) [31, 69-81]. The hinge connected between two panels is made of materials that can respond to different stimuli (e.g., heat) and usually results in chemical or physical changes (e.g., melt). When the hinge's physical property changes, a driving force (e.g., surface tension stress) is normally spontaneously generated, leading to the movements of the panels connected to the hinge. As shown in figure 1.7, the two rigid panels can be self-assembled and folded towards each other under a heating condition just like the closure of the Venus flytrap's leaves and the folding of papers.

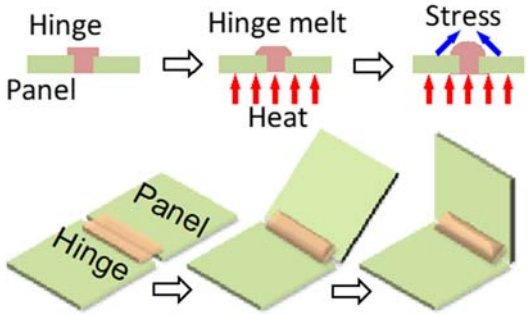

Figure 1.7 Self-assembly in micro-scale. The micro-scale structure contains two rigid panels and one hinge connected between them. Heat triggers the hinge to melt and generate surface tension force to lift up the panels.

Another example of self-assembly is self-curving in nano-scale [82-87]. Figure 1.8 shows a nano-scale bilayer structure made of thin Nickel (Ni) top layer and thin Tin (Sn) bottom layer. When reactive ion etching (RIE) is applied to the structure, silicon (Si) substrate underneath the structure is being etched while Sn grains in the top layer start to melt and coalesce (figure 1.8a-e). The Sn grain coalescence introduces stress in the Sn-Ni bilayer and curves the structure upwards (figure 1.8f and g). This nano-scale self-assembly process is similar to the curving of pinecones upon wetting and drying. The differences are the driving forces of the self-assembly, the stimuli, and the materials and dimensions of the structures.

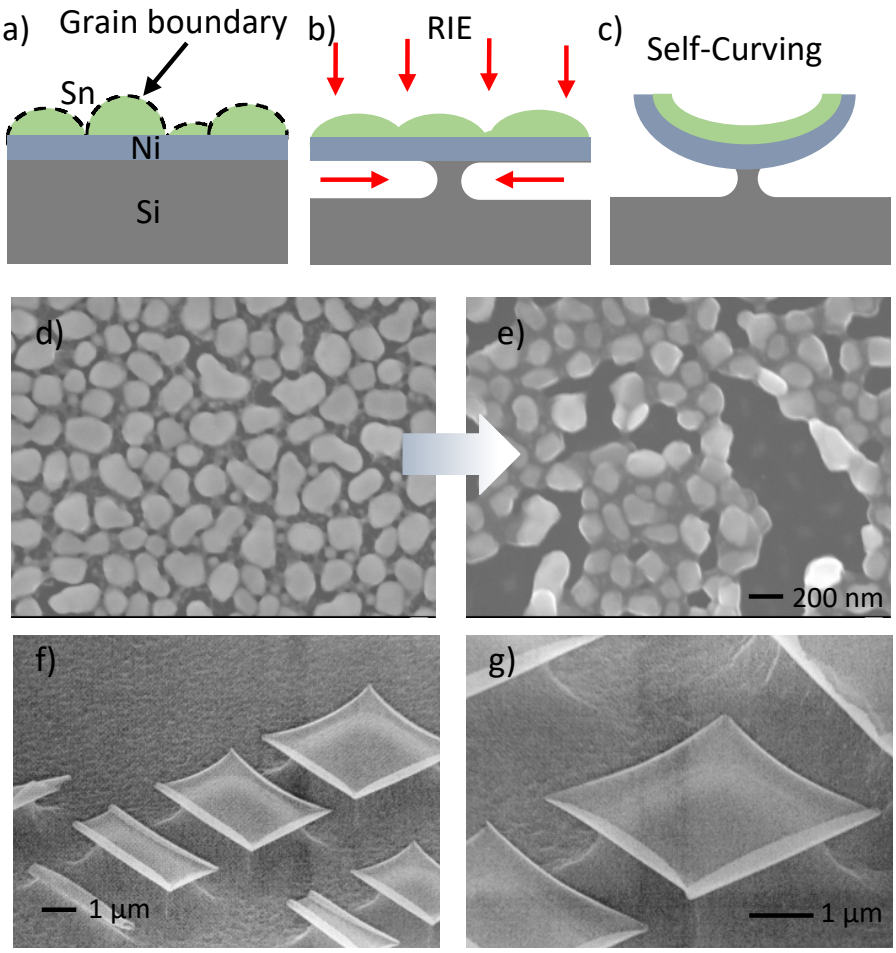

Figure 1.8 Self-assembly of nano-scale structures. Ni thin films with nano-scale dimensions are curving up due to the stress induced during Tin grain coalescence.

The ability to create complex 3D structures in micro- and nano-scale using self-assembly is significant [31, 88]. First, self-assembly reduces the complication of creating 3D structures using standard manufacturing techniques. The self-assembly process is fast, simple, and inexpensive. Second, self-assembly in micro- and nano-scale is compatible with current micro- and nano-fabrication processes. Functional structures and devices can be easily designed and developed by combining self-assembly and other fabrication techniques [89]. Third, self-assembly provides a hand-free method for controlling small

objects and movements. This is extremely important when micro-robots and micro-actuators are needed for medical and biological fields [90-95].

1.3 Self-assembly driving forces

It is not difficult to notice the similarities among self-assemblies in nature and in the micro- and nano-world. To have a better understanding of the man-made self-assembly process and help us design a self-assembly system, we need to revisit the important elements in the self-assembly definition. "*Pre-existing components*" is the precondition of designing any self-assembly system. By adjusting the pre-existing components, a final structure can be predicted and created. This gives the self-assembly a large freedom to be able to create any structures in our mind. "*Environment*" or "*stimulus*" is what triggers the self-assembly. It is the signal that the outside world gives to the structures or systems for them to act. Without stimulus, a system will remain its pre-existing status and loses its characters of being a self-assembly system. "*Driving force*" is what makes all the magic happens. For instance, in order to make the pinecone open and close, the swelling and shrinking differences between upper and lower scale is the driving force. To make two micro-scale panels folding together, a surface tension force is the driving force. Driving force is the connection between the stimulus and the actual self-assembly movement [31, 96-100]. In the following sections, different self-assembly driving forces and stimuli will be discussed. It is critical to understand various driving forces and stimuli before designing self-assembly systems.

1.3.1 Pneumatic force-driven self-assembly

Pneumatic force-driven self-assembly uses flexible chambers and joints to realize self-assembly [101-104]. When fluids (e.g., air, water) are pumped into the chambers, the elastic joints are forced to bend and assemble the structure. The advantage of pneumatic self-assembly is that the folding is reversible through many pumping cycles. However, the structures for pneumatic self-assembly tend to be large (usually in millimeter scale) and the pumps and tubes have to be connected to the structure to make the self-assembly work.

1.3.2 Magnetic force-driven self-assembly

Magnetic force-driven self-assembly is normally realized by designing the rigid structures with ferromagnetic materials (e.g., Ni, iron) with a flexible hinge [105-110]. Upon applying a magnetic field to the structure, the magnetic rigid structures move around the flexible hinge due to the magnetic field. This is an easy and inexpensive method to realize complex structures. The drawback of the magnetic force-driven self-assembly is that at least one point of the structure has to be anchored on the substrate, otherwise the applied magnetic field will push the entire structure away. In addition, final self-assembled structure tends to be instable and returns back to its original form once the magnetic field is removed. Thus advanced locking mechanism is needed for this type of self-assembly.

1.3.3 Volumetric expansion-driven self-assembly

Hydrogel is one of the most common volumetric expansion materials for self-assembly [111-117]. Hydrogel is a polymeric network that can absorb solvents and swell. Depends on whether the hydrogel is merged or detached to the solvent, it can swell or contract, results in bending, folding and wrinkling of the structures. Most of the volumetric expansion-driven self-assembly is reversible due to the unique property of the hydrogel. In addition, other factors like temperature, pH, and ionic concentration of the solvent can also affect the swelling and contracting behaviors of the hydrogel, making the self-assembly process more maneuverable. However the hydrogel volumetric expansion-driven self-assembly needs to be conducted in an aquatic environment, which limits its applications.

1.3.4 Differential thermal expansion-driven self-assembly

Differential thermal expansion-driven self-assembly usually contains a bilayer structure [118-121]. The materials for each layer are carefully selected so that the thermal expansion coefficient of each material is different from each other. After applying heat to the bilayer structure, the expansion of each layer is different due to the different thermal expansion coefficient, leading to the bend of the structure. By controlling the heat and the material properties of the bilayer, the curvature of the bending can be precisely predicted and adjusted. Trilayer and multiple joint structures can also be designed to create more complex 3D structures using differential thermal expansion-driven self-assembly.

1.3.5 Surface tension-driven self-assembly

Surface tension-driven self-assembly is one of the most common and simple self-assembly methods [122, 123]. Rigid components are usually connected together by a heat-sensitive hinge. Applying heat to the structure melts the hinge material and forms a liquid droplet shape between the rigid components. A surface tension force can be generated along the surface of the hinge droplet and pull the two rigid components closer. This is due to the surface trying to find the minimum energy state. The surface tension force is large enough to join the two rigid components and fold the structures. Once the heat is removed from the structure, the hinge re-solidified and secures the self-assembled 3D structures. Since hinges and panels can be freely designed and located, complex 3D structures can be easily created using surface tension-driven self-assembly.

1.3.6 Shape memory-driven self-assembly

Shape memory gains many attentions in recent years to realize 3D self-assembled structures [75, 124-130]. Shape memory alloys (SMAs) are special alloys that have multiple transition stages at various temperatures. They are usually created at certain temperatures to form an original shape. The SMA can be then bended and deformed to any shapes. Upon placing the SMA back to the temperature it was created, the SMA can be automatically transformed back to its original shape. The self-assembly using SMAs has many benefits because of the programmable property of the SMAs. However,

fabricating SMA for self-assembly is considerably difficult due to the patterning issues and high temperature deposition.

1.3.7 Thin film stress-driven self-assembly

Thin film stress-driven self-assembly also contains bilayers or trilayers in the structure [131-137]. Unlike differential thermal expansion-driven self-assembly, whose assembly process is triggered by heating, thin film stress-driven self-assembly maintains the stress inside the layers without any external stimuli. The stress between layers is normally due to the lattice mismatch, layer boundary conditions, and thermal coefficients during the thin film deposition processes. Since the layers are deposited on a substrate, the intrinsic stress does not affect the shape of the structure. Upon release the structure from the substrate, the structure is free from the restrict of the substrates, leading to the bending of the structures due to the stored stress. Thin film stress-driven self-assembly is not as widely used as other self-assembly techniques because the stress generated during the deposition process is difficult to control and thus the assembly result is hard to predict.

1.3.8 Shrinkage-driven self-assembly

The shrinkage-driven self-assembly refers to the self-assembly using an elastic hinge material (e.g., polyimide) that can shrink when high curing temperature is applied to the material [138, 139]. The shrink of the hinge causes bending of the structures. The

bending of the structures can be controlled by adjusting the curing temperature of the hinge. The disadvantage of the shrinkage-driven self-assembly is that normally a really high temperature (more than 200 ºC) is required for the hinge to shrink, which may cause damage to other components within the structures.

1.3.9 Cell traction force-driven self-assembly

Cell traction force-driven self-assembly is a newly developed area for self-assembly [140, 141]. The idea being that instead of using flexible and elastic polymers as the hinge materials, cells are being cultured inside a biological scaffold between the panels. The cell contraction can be triggered using electrical signals and pull the panels to realize self-assembly. Regardless of the novel and unique idea of cell traction force-driven self-assembly, there are still many problems related to it. The biggest problem is that the cell hinge itself is not robust enough to hold the entire structure together, which makes the self-assembled structure easy to break.

1.4 Stimuli of self-assembly

Stimuli are the triggers for the driving force to occur at the beginning of the self-assembly process. It is noticed that stimulus and driving force are not one-to-one correspondence, meaning that several stimuli can be used to trigger a certain type of self-

assembly, while one stimulus can also be used by multiple driving forces. Common self-assembly stimuli are listed in the sections below.

1.4.1 Heat triggered self-assembly

Heat is the most common stimulus to trigger thermo-responsive self-assembly process [75, 118-123, 128-130, 138, 139]. Applying constant heat to the structure can result in the melting of the hinges in surface tension-driven self-assembly, the transformation of the SMAs, the shrinkage of polyimide hinges, and the swell and contract of the bilayers for differential thermal expansion-driven self-assembly. In addition, different temperatures of the solvent can also affect the swelling of the hydrogels, leading to different self-assembly shapes. The advantages of heat stimulus are that it is easy to apply to the structure and can realize reversible self-assembly for most of the cases. However, the heat capacity of the common heat source (e.g., hotplate, hot water bath) is relatively large ($C=Q/\Delta T$, C is the heat capacity, Q is the transferred heat, and ΔT is the temperature difference), which makes the thermal response of the heat source slow. The temperature change of the structure surface is thus difficult to control, which is not suitable for fast-responsive applications and precisely controllable self-assembly.

1.4.2 Solvent triggered self-assembly

Solvent stimulus is widely used in hydrogels for volumetric expansion-driven self-assembly and used as the pumping fluid in the pneumatic self-assembly [101-104, 111-117]. In most of the situations, the water in the solvent can react with water-responsive polymers (e.g., hydrogels) to introduce swell and contract in the polymer. Solvent stimulus is always combined with other stimuli (e.g., temperature, pH, concentration) to trigger the self-assembly process. The advantage of solvent-triggered self-assembly is that the trigger (solvent) is easy to obtain and self-assembly process is simple and inexpensive. The disadvantage of the solvent-triggered self-assembly is that the assembly needs to be conducted in an aquatic environment, which limits its applications.

1.4.3 pH triggered self-assembly

Self-assembly triggered by pH uses polyelectrolytes as the active material. pH sensitive materials can be seen as smart hydrogels [116, 143-145]. Similar to water response of hydrogel, pH sensitive materials response to both water and pH in the solvent. Such materials can be made into bilayer structures. When pH in the solvent changes, the swelling ratio between the top and bottom layers also varies, which leads to a bending of the structure. Gracias *et al* studied the swelling ratio differences of N-isopropyl-acrylamide (NIPAm) and its bilayers under different pH levels, illustrating the possibility of using pH to tune the self-assembly process. However, like hydrogel, the pH triggered self-assembly needs to be conducted in an aquatic environment.

1.4.4 Other triggers for self-assembly

There are many others stimuli for self-assembly like magnetic field [105-110], electric signal [146-148], enzyme [149], ionic strength of the solvent [98,150-152], pressure [101-104], and light [125-127]. Each of the stimulus has its unique way of generating the driving force for the self-assembly. I will not list the details for each of the self-assembly stimuli but learning the stimuli and driving forces is the first step to understand the self-assembly process. In addition, each driving force and stimulus has its own advantages and disadvantages. Wisely choosing the suitable method depending on the condition of the self-assembly is the key to design a successful self-assembly system.

1.5 Quick summary

Table 1.1 is a quick summary of all the common driving forces and stimuli for micro-scale and nano-scale self-assembly. The materials, dimensions, advantages and disadvantages of those methods area also listed for better comparisons between each method.

Table 1.1 Self-assembly driving forces and stimuli

Driving forces	Stimuli	Dimensions	Materials	Advantages	Disadvantages
Pneumatic force	Pressure	mm to cm	Elastic polymers	Reversible assembly	Large dimensions, pump and tube connection
Magnetic force	Magnetic field	nm to mm	Ferromagnetic materials	Remote control, easy to apply	Anchor required, locking mechanism required
Volumetric expansion	Solvent, temperature, pH, ionic strength	µm to mm	Hydrogels	Simple stimuli, multiple controls	Aquatic environment required
Differential thermal expansion	Heat	µm	Bilayers with different thermal expansion coefficient	Simple stimuli	Limited curvature
Surface tension	Heat	nm to mm	Materials that can be liquified	Simple stimuli, easy to control and maneuver	High temperature required, locking mechanism required
Shape memory	Heat	µm to mm	SMAs	Simple stimuli	Programming and high deposition temperature required
Thin film stress	No active stimuli	nm to µm	Bilayers, trilayers	Simple design	Passive triggers, difficult to control
Shrinkage	Heat	µm	polyimide	Simple stimuli, easy to control	High temperature required
Cell traction force	Electric signal	mm to cm	Cells and biological scarfolds	Novel ideas, biocompatible	Instable structure

Chapter 2

Remotely Controlled Self-Assembly Overview

2.1 Current issues of direct-triggered self-assembly

Among above mentioned self-assembly techniques, direct interactions or contacts between the stimuli and the structures are normally required to trigger the self-assembly process. For example, during the surface tension-driven self-assembly process, the heat energy usually comes from an external source (e.g., hotplate, hot water bath) [153-156]. The thermal-sensitive hinges normally have direct contact with the hotplate or are merged in the hot water bath to achieve a rapid temperature increase. For volumetric expansion-driven self-assembly, physical/chemical reactions occur when the solvent-sensitive hinges are merged inside the solvent, triggering the self-assembly [157-160]. We call this type of self-assembly *direct-triggered self-assembly* because the stimuli and the structures are in direct contact. Direct-triggered self-assembly has its benefits of short response time, fast self-assembly process, and simple and easy system setup. However, because of the structures to be self-assembled cannot be accessed during the process, the manipulative capability and yield of the direct-triggered self-assembly are usually low, which limits its applications. In addition, the direct-triggers cannot be applied in situations where the self-assembly has to be conducted in a confined and non-accessible environments [161]. Moreover, due to the high specific heat of the hotplate and hot water bath, the heat energy cannot be precisely controlled, which makes it difficult to realize precisely controlled self-

assembly process and prevent the self-assembly technique to be used in various applications.

In addition, some self-assembly applications require the assembly of 3D structures to be completed in situations where the energy source or the environmental changes adjacent to the 2D structures to be assembled are not accessible. For example, self-assembly drug delivery system has to be assembled and dis-assembled inside human bodies to deliver the drugs to targeted organs and tissues for its maximum effects. This cannot be realized using direct-triggered self-assembly techniques because the heat or solvent triggers cannot pass through organ or tissue barriers to reach the structure to be assembled.

2.2 Theory of remotely controlled self-assembly

To alleviate above issues of direct-triggered self-assembly, indirect triggers have been used to realize remote-controlled self-assembly. Common remote-controlled energy sources include laser [162, 163], light [164, 165], and electromagnetic energy [161]. By applying electromagnetic energy or intense laser/light, heat can be generated locally on the surface of the sample or at the hinge areas. The localized heat can melt the hinge materials to trigger the self-assembly process. The localized heat generation can be precisely adjusted and controlled by the remotely located triggers (e.g., laser, light). This remote controls of the self-assembly process does not requires direct contacts between the structure and the triggers, increasing the manipulative capability of the process. However, complicated and expensive optical/laser systems are required to generate the laser/light

source and focus the laser/light on the hinge areas of the sample. In addition, laser/light triggered self-assembly requires the hinge to be exposed to the laser/light source, which is inconvenient in situations where the structure to be assembled in located in a closed environment (e.g., human body). In addition, in order to generate enough heat to trigger the self-assembly process, the light-sensitive hinge area needs to be large enough (usually in millimeter scale), which is not compatible with micro- and nano- technologies.

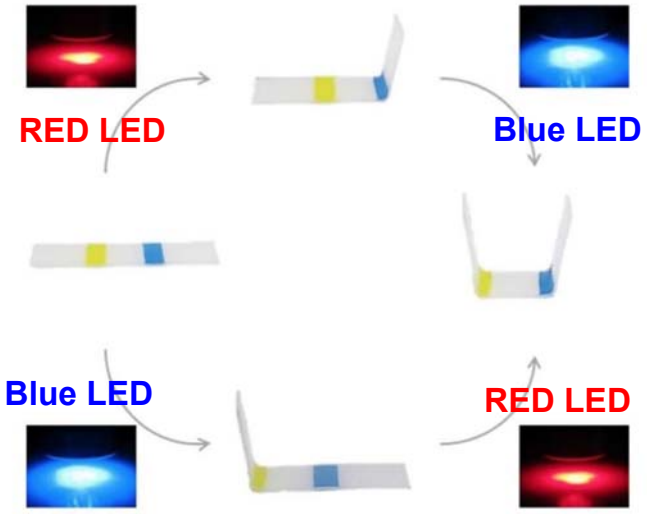

Figure 2.1 Remotely controlled self-assembly triggered by LED lights with different wavelengths (blue and red in color). Hinges with different colors can selectively absorb lights with different wavelengths, results in selective self-assembly of the structures [165].

2.2.1 Remotely controlled electromagnetic energy source

In order to address above problems of current indirect triggered self-assembly, in this Ph.D. work, we have developed a remote-controlled self-assembly technique using electromagnetic energy to avoid direct contact between the structures and the energy sources, and to achieve precise control of self-assembly [161]. The electromagnetic energy

induces eddy current and joule heating, causing the temperature of the structural materials (i.e., metal thin films) or the hinge materials (e.g., graphene ink, metal particles) to increase and trigger self-assembly (figure 2.2) [161]. The remotely applied electromagnetic energy leads to quick and accurate control of the self-assembly of polymer panels, which are ideal for rapid self-assembly applications and remotely controlled applications. The remotely controlled electromagnetic self-assembly combines surface-tension-driven self-assembly and electromagnetic heating, providing an ideal route to fast and precise self-assembly process. Since electromagnetic heat can generate a large amount of thermal energy within small areas, the dimension of the self-assembled structure can be reduced to micro-scale, enhancing the compatibility of the remotely controlled self-assembly with micro-fabrication techniques.

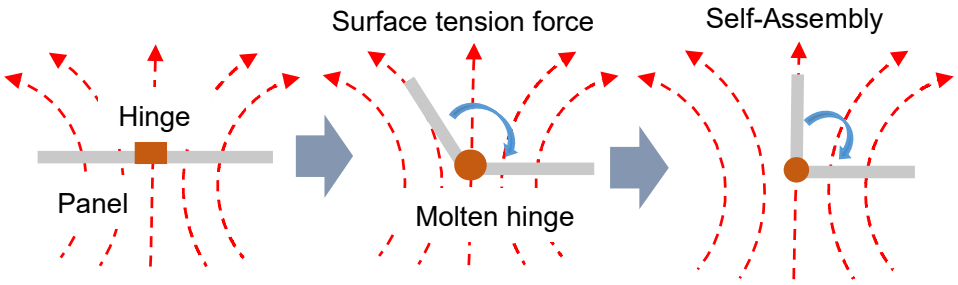

Figure 2.2 Remotely controlled self-assembly using electromagnetic energy

Depends on the frequency of the electromagnetic field, the electromagnetic energy source can be separated as microwave energy source and induction energy source. For microwave energy source, high frequency electromagnetic wave (2.45 GHz) is generated using a magnetron [161]. The generated electromagnetic wave is then directed by a waveguide to the sample. The entire system needs to be properly isolated due to the

danger of microwave to human beings. The induction energy source is constructed with an induction coil connected with an induction generator circuit. A magnetic wave of a few hundreds of MHz can be generated through the induction coils by applying AC power to the coil. Since the frequency of the induction electromagnetic field is much lower compared to the microwave electromagnetic field, induction is not harmful to human beings. Both microwave and induction energy source can generate electromagnetic fields that can be remotely applied to the structure for self-assembly. Both of them have their advantages and disadvantages. Microwave remotely controlled self-assembly can be used in situations that rapid assembly is required. Since the microwave electromagnetic field has high power and frequency, an assembly of under 10 sec can be easily realized. However, the microwave energy is harmful to living tissues and organs, which is not suitable for biomedical applications like drug delivery, biomedical sensing, cell encapsulation, and cell culture [166-174]. Induction induced magnetic field operates at a frequency of a few MHz to hundreds of MHz, which is high enough to generate heat to trigger the self-assembly process but low enough not to harm human bodies and living tissues and organs. The drawback of induction self-assembly is that the strength of the magnetic field is decaying exponentially with increase of the distance between the object and the induction coil. In order to realize long distance remotely controlled self-assembly, special coil designs and high power and high frequency induction systems need to be considered.

2.2.2 Eddy current generation by electromagnetic wave

The remote-controlled self-assembly is driven by the eddy current heat generation process inside metal thin films. The generated rapid-alternating magnetic field (*H*) penetrates through the metal thin films and induces a loop of electric current (*I*), namely eddy current, in the metal thin film due to the changing magnetic field (*H*) (figure 2.3). The generation of eddy current inside metal thin film under changing magnetic field can be explained by Faraday's law of induction [175, 176]. According to Faraday's law of induction, when an alternating magnetic field (*B*) is applying to a thin sheet of conductor, a magnetic flux ($\Phi B = B \times S$ when magnetic field is constant, where S is the surface of the conductor) is generated through the surface of the conductor, which can be defined as the surface integral of the magnetic field (*B*) components normal to the surface (*S*):

$$\Phi_B = \iint_S B \cdot ds \tag{1}$$

Since the magnetic field (*B*) applied to the conductor is changing with time, magnetic flux (ΦB) is also changing accordingly, which creates an electric field (*E*) inside the conductor. The generated electric field (*E*) is circulating around the magnetic field line and the direction of the electric field (*E*) is counterclockwise against the magnetic flux:

$$\nabla \times E = -\frac{\partial B(t)}{\partial t} \tag{2}$$

Where $\nabla \times E$ is the curl of the electric field vector and $\frac{\partial B(t)}{\partial t}$ is the time-variable magnetic field.

This electric field loop inside the thin sheet of conductor creates a loop current (*I*) circulating inside the thin sheet, which is defined as eddy current [175, 176]. The

generation of eddy current can also be explained by Lenz's law. According to Lenz's law, the changing magnetic flux (ΦB) introduces an electromotive force (EMF) inside the thin sheet of conductor:

$$\varepsilon = -\frac{d\Phi_B}{dt} \tag{3}$$

Where ε is the EMF and $d\Phi B$ is the changing magnetic flux with time (t). The generated EMF is applied to the mobile charge carriers (electrons) inside the conductor, which drives the electrons to move accordingly and generate the eddy current (I). The direction of the eddy current can be determined by such that it generates a magnetic field that opposes the changing field that produces it.

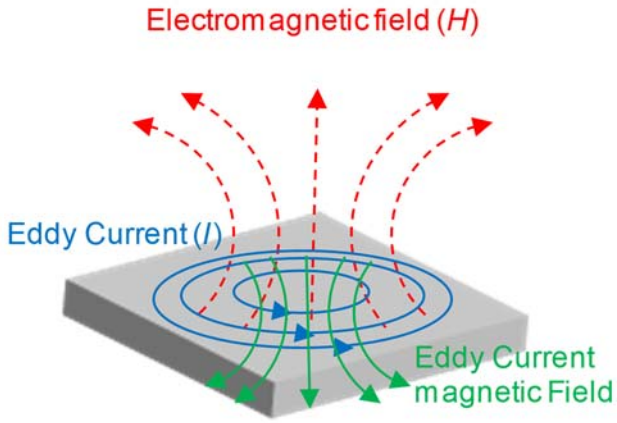

Figure 2.3 Eddy current (I) generation by electromagnetic field (H) inside metal thin films.

2.2.3 Eddy current heat generation

Eddy current (I) is circulating inside the metal thin film and is flowing against the resistance (R) of the thin film (figure 2.4). According to Joule's effect, when the current passes through the conductor, part of the electrical energy converts to heat energy through resistive losses due to the collision and friction of the electrons and conductor atoms inside the conductor [177, 178]. The power dissipation (P) of the eddy current (I) due to joule loss depends on the resistivity of the conducting material and the eddy current itself (I) [179, 180]:

$$P \propto I^2 \cdot R \tag{4}$$

Taking eddy current, magnetic field properties, conducting material properties and thin film dimensions into consideration, equation 4 can be rewrite to a more complicated form [181]:

$$P = \frac{\pi^2 \cdot B_p^2 \cdot d^2 \cdot f^2}{6 \cdot \kappa \cdot \rho \cdot D} \tag{5}$$

Where P is the power dissipation by eddy current per unit mass [W/kg], Bp is the peak of magnetic field [T], d is the thickness of the metal thin film [m], f is the frequency of the magnetic field [Hz], κ is a constant (κ = 1 for thin sheet of conductor), ρ is the resistivity of the metal thin film [ohm·m] and D is the density of metal thin film [kg/m^3]. The power dissipation by eddy current inside the thin film of conductor can then be converted to heat generation by relating the power dissipation of eddy current (thermal energy) with temperature raise of the thin film using specific heat capacity of the conducting thin film [182]:

$$C = \frac{Q}{\Delta T} = \frac{P \cdot t}{\Delta T} \tag{6}$$

Where C is specific heat capacity of the conducting material, Q is the thermal energy, T is temperature and P is the power dissipation by eddy current. Equation 6 shows that the temperature changes (ΔT) of the conducting thin film due to the power dissipation by the eddy current circulating inside the thin film. Metal thin films with nano-scale thicknesses are used to verify my theory. When alternating magnetic field is applied to the metal thin film, eddy currents can be created inside the metal thin film. The generated eddy currents flows against the resistance of the metal thin film and generate thermal energy by joule heating. The thermal energy in the metal thin film results in the rapid temperature increase of the metal thin film to realize remote-controlled heat generation of metal thin film.

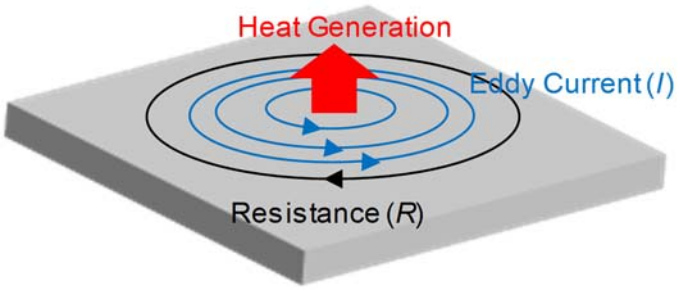

Figure 2.4 Eddy current heat generation. Eddy current (I) inside the metal thin film flows against the resistance (R) of the thin film, which results in Joule heating.

2.3 Design of remotely controlled self-assembly

To realize remotely controlled self-assembly of micro-scale structures, the pre-existing components of the 2D micro-scale structures consists of rigid panels and thermal sensitive hinges. The heat generation from the eddy current in the metal thin film triggers

the thermal sensitive hinge to reflow, leading to a surface tension force generation. The surface tension force lifts up the rigid panels and transform the 2D pre-existing micro-scale structures into 3D structures (figure 2.2). In this case, the surface tension force is the driving force for the remotely controlled self-assembly. After the electromagnetic field is removed from the structure, the hinge temperature drops dramatically due to heat dissipation to the environment and re-solidifies to secured the self-assembled 3D structure.

2.4 Advantages of remotely controlled self-assembly

The advanced remotely controlled self-assembly technique using electromagnetic energy can be used to create 3D self-assembled structures for various applications, including 3D sensors [89, 183-185], carriers [186], and microbots [187-190]. In addition, the ability to build 3D structures on a micro-scale is essential because micro-scale self-assembly allows for the realization of 3D structures that can be used for 3D terahertz (THz) sensors [191-193] and biomedical devices designed for *in vivo* operation [194-198]. Also, multiple and sequential self-assembly can be realized under a single remotely located energy source by applying different hinge materials, angle locking mechanisms and different configurations of the hinge structures. This allows the development of complex 3D microstructures with multiple configurations. In addition, induction magnetic field can penetrate through biomaterials and the generated heat is localized only on the surface of the microstructures. Induction heating can trigger self-assembly without harming live organs or tissues, showing the potential for biomedical applications like cell encapsulation, cell cultural, biomedical sensing, and drug delivery. Using remote-

controlled assembly technique to secure drugs in a 3D structure and remotely control the release of drugs in specific locations of the body can reduce the side effects of drugs to minimum.

Chapter 3

Remote-Controlled Microwave Driven Self-Assembly

3.1 Theory of Microwave triggered self-assembly

A novel 3D self-assembly of microstructures using remote-controlled microwave energies has been developed [161]. A remotely located microwave energy source can generate high frequency microwave that triggers the localized heating of the microstructures to trigger the self-assembly process. The assembly of the panels can be precisely controlled by adjusting the microwave energy source, which improving the manipulative capability of the remote-controlled self-assembly process in situations where the energy sources are not controllable and accessible. Microwave can trigger the self-assembly process from a long distance due to its high frequency and strong electromagnetic field, which is suitable for applications where the structure is far away from the energy source.

The remote-controlled self-assembly process is driven by eddy current heat generation within the metal thin films (figure 3.1) [161]. A magnetron with a high frequency of 2.45 GHz is used as a remote-located energy source (figure 3.1a). The magnetron can generate a rapid-alternating electromagnetic wave (B) that penetrates through the thin metal films, resulting in a loop of eddy current (I) inside the metal thin film [175, 176]. The eddy current inside the metal thin film flows against the resistance of the metal (R), which dissipates energy as heat to its surroundings (figure 3.1a). This eddy

current heat generation process is called Joule heating, which is caused by the collision and friction between the electrons and conductors inside the metal [177-180]. Above eddy current heat generation induced by microwave can be applied to a 2D microstructure freestanding on a substrate with a thin metal film (Cr). As the microwave is applying to the Cr thin film, the heat can be generated within the Cr film and passed to the polymer hinges (polycaprolactone, PCL or SPR-220). The temperature of the hinges exceeds the melting point of the hinges and triggers the reflow the polymer hinges, which generates surface tension force (figure 3.1b and 3.1c). The panels that are connected by the hinges are made of SU-8 resist, which is rigid during the heating process. Thus the generated surface tension force can lift up the SU-8 panels and trigger the self-assembly of a 2D microstructures to a 3D cubic structure. After the microwave is removed from the sample, the eddy current heating process stops, which results in the rapid temperature drop of the samples due to the low mass and large surface areas of the Cr thin film. The hinges are re-solidified and secure the panels and the entire shape of the 3D microstructure (figure 3.1b and c). Two different configurations of the micro structures can be designed to illustrate the microwave driven remote-controlled self-assembly: anchorless design (figure 3.1b) and anchored design (figure 3.1c). The anchorlss design (figure 3.1b) shows the microstructure with a thin Cr film embedded under the SU-8 panels. This design allows the structure to be self-assembled without attaching to a substrate that has a pre-deposited Cr layer. The self-assembly of an individual microstructure can be achieved using the anchorless design due to the fact that the heat generation comes from each Cr thin films within the SU-8 panels. PCL is used as the hinge material because of the low melting point of PCL (60 ^{o}C), compensating for the small area of the Cr films for the anchorless

design. For anchored design (figure 3.1c), the Cr thin film is deposited on the entire glass substrate under the microstructures to achieve a large heat generation. The microstructures are supported on the Cr/glass substrate by a thick Cr pillar and do not have any contact with the substrate. SPR-220 hinges are used for this anchored design with a melting point of around 100 ºC due to the easier fabrication process of the SPR-220 hinges compared to PCL hinges.

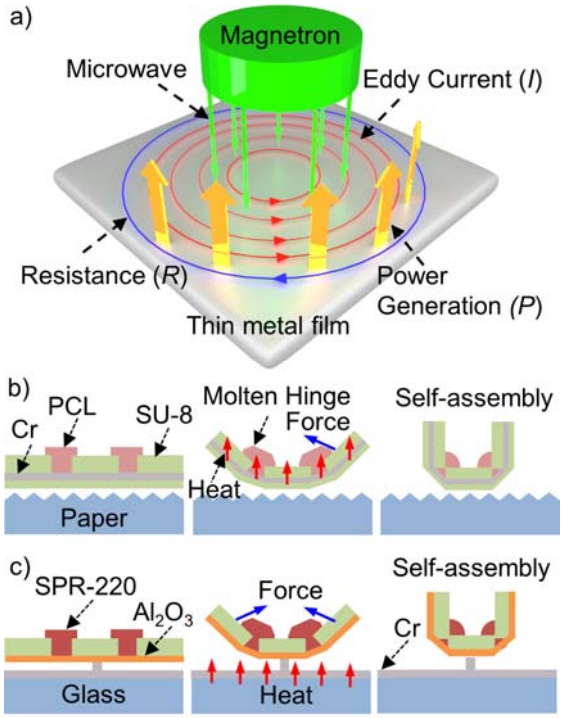

Figure 3.1 Illustration of remotely controlled 3D self-assembly using microwave Energy [161]. (a) Heat power generation within a Cr thin film via eddy current looping in the Cr film against the resistance of the Cr. The eddy current is induced by electromagnetic waves generated by a magnetron. Self-assembly of cubic structures consisted of a nano-scale Cr film, SU-8 panels, (b) PCL hinges and (c) SPR-220 hinges. Hinges are melted due to heat generation within Cr, inducing surface tension force on the hinges, leading to self-assembly. (d) A microwave system for remote-controlled self-assembly. Generated

microwave energy is applied to the sample through a waveguide in a remote location without physical contact, inducing heat generation for self-assembly.

3.2 Remotely controlled microwave system setup

A commercialized magnetron (Galanz M24FA-410A) with a power of 1050 W was used for the microwave energy source, which operates at a frequency of 2.45 GHz [161]. A waveguide is used to guide the generated microwave towards the sample to be self-assembled. The sample was placed on a plastic holder upon assembly to reduce the effects of the sample holder on the heating process (figure 3.2). Since the microwave is remotely applied to the microstructure though a magnetron and a waveguide, no direct contact between the sample and the energy source is required (figure 3.2). The remotely microwave generates a localized heat energy on the microstructures, leading to the reflow of the hinges and trigger the self-assembly process.

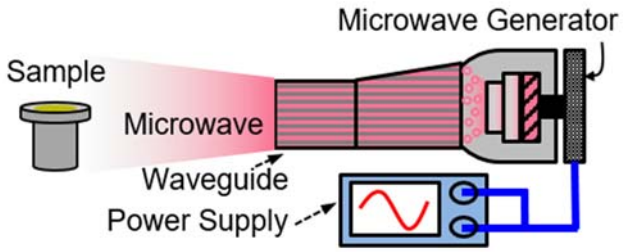

Figure 3.2 A microwave system for remote-controlled self-assembly [161]. Generated microwave energy is applied to the sample through a waveguide in a remote location without physical contact, inducing heat generation for self-assembly.

3.3 Sample design

3.3.1 Anchored and anchorless design of the micro-scale structures

To achieve the remote-controlled self-assembly of microstructures using microwave energy, a 2D microstructure with SU-8 panels and polymer hinges (PCL or SPR-220 depends on the design) was fabricated on a glass substrate upon applying microwave energy to the sample [161]. A 300 nm Cu was used as the sacrificial layer between the glass and the 2D microstructure for releasing the 2D microstructure before self-assembly.

If the structure is anchored to the substrate, the Cu sacrificial layer are partially etched to detach the structure from the Cr thin film substrate while the 2D structures still maintain its original positions on the substrate. When remote-controlled electromagnetic energy is applied to the sample, heat is generated inside the Cr thin film due to the eddy current effect describe above and the heat transfers from the Cr thin film to the 2D structures on the Cr thin film. Since the distance between the 2D structure and the Cr thin film is small (300 nm, defined by the thickness of the Cu sacrificial layer), the majority of the heat generated by the eddy current can be transferred to the 2D structure. Large heat generation leads to high temperature localized on the 2D structures, which exceeds the melting point of the polymer hinges. The molten hinges can generate surface tension forces to lift the panels and realize self-assembly of 2D structures to 3D structures. After the microwave is removed from the sample, the temperature of the sample rapidly decreases, leading to the re-solidification of the hinges. The hinges are not only patterned between panels but also located on each side of the panels, results in the design of self-locking structures. When the panels are folded to 90 degrees, the two adjacent panels are

connected to each other with the hinges locking the position of the two panels to prevent over-folding. Thus a 3D well-shaped folded cubic structure can be created using this method.

If the structure is anchorless, instead of using polymeric rigid panels, metallic panels are used to generate heat under electromagnetic field [161]. The panels and hinges are built on a Cu sacrificial layer. The structure is then completed released from the substrate by etching the Cu sacrificial layer using Cu etchant. Upon self-assembly, the structure is placed on a paper substrate. Electromagnetic field creates eddy current inside the metallic panels and generates heat to trigger the self-assembly process.

Depends on the two different configurations of the micro structures (anchored or anchorless), the materials used for each component of the structure are also different [161]. For anchored structures, metal film is deposited on the entire glass substrate to achieve a large area for higher heat generation. Cr is normally used for this purpose. The material of the substrate is glass to eliminate the effect of the substrate from the electromagnetic heating. The thickness of the Cr thin film on the glass substrate varies from a few nanometers to tens of nanometers. The panel material is a photoresist called SU-8 2010 (MicroChem). SU-8 resist becomes hardened and is resist to heat and most solvents when hard-baked, which is ideal for rigid panels. SPR-220 7.0 photoresist (MicroChem) is usually used as the hinge material (with a melting point of around 100 ^{o}C). Since the Cr film is deposited on the entire glass substrate, the heat generation is large enough to melt the SPR-220 hinges and trigger the self-assembly process.

For anchorless structures, the metal films can be either embedded in the SU-8 panels or used as the entire panels to achieve self-assembly without attaching to a

substrate. This allows a single microstructure to be self-assembled using microwave energy. Any metals with ferromagnetic properties and are resist to Cu etchant (e.g., Ni, Cr) can be both used for this purpose. Since the metal film area exposed to the electromagnetic field is much smaller compared to anchored structures, PCL hinge is used due to its low melting point of 60 ºC.

Table 2.1 Comparison between anchored and anchorless self-assembly

	Anchored	Anchorless
Substrate	Glass	Paper
Heating component	Cr adhesion layers	Cr or Ni panels
Panels	SU-8	SU-8 and/or Metal
Hinges	SPR-220 resist	PCL
Advantages	Realization of an array of self-assembled structures, high yield	Individual structure control, low temperature requirement
Disadvantages	High assembly temperature required	Low yield

3.3.2 Substrate selection

For anchorless structure, the structure was placed on a paper substrate before self-assembly [161]. Choosing paper material as a substrate eliminates the effect of the substrate to the heating process since paper does not react with electromagnetic field. For anchored structure, the structure was attached to the substrate that contains glass and a thin layer of Cr. In this case, glass is used as an inert supporting substrate and Cr thin film is used as the electromagnetic heating layer.

3.4 Fabrication process

The Cr thin films can be either placed on a glass substrate to realize a self-assembled cubic structure array or in each microstructure for substrate-free self-assembly applications [161]. In both cases, 2D structures (SU-8 panels and polymeric hinges) are patterned using conventional photolithography process. For self-assembly on a substrate, the Cu sacrificial layer is partially etched to detach the structure from the Cr thin film substrate while the 2D structures still maintain their original positions on the substrate. For substrate-free self-assembly, the entire structure is released from the glass substrate and transferred onto a paper (inactive to microwave energy) to simulate the in-situ environment.

3.4.1 Anchored structures

To fabricate 2D micro-scale structures for self-assembly on a substrate, a 1 μm Cr was patterned on the glass substrate to support the 2D structures (figure 3.3a). A Cr heat generation layer with various thicknesses (from 10 nm to 15 nm) and a 300 nm thick Cu sacrificial layer were then deposited on the substrate using an E-beam evaporation process (figure 3,3b), followed by a 30 nm thick aluminum oxide (Al_2O_3) pattern (figure 3.3c). The purpose of this Al_2O_3 layer is to separate the panels and hinges from the substrate to prevent the adhesion between panels/hinges and the substrate. 16 μm thick SU-8 panels and 24 μm thick SPR-220 hinges were patterned on the Al_2O_3 layer using photolithography process (figure 3.3d and 3.3e). The Cu sacrificial layer was then

removed by immerging the sample in the Cu etchant (figure 3.3f). The sample was then rinsed with deionized (DI) water and dried in air. Since a 1 μm Cr is used to support the panels and hinges, the 2D structures remain at their original positions on the substrate. The sample was then placed on the sample holder inside the microwave system chamber and microwave was applied to the sample to induce heat generation by eddy current inside the Cr thin films on top of the glass substrate. SPR-220 hinges were melted due to the heat generation and the generated surface tension force leads to the self-assembly of the 2D structures to 3D cubic structures (figure 3.3g and h). Optical microscopic images show the 2D micro-scale structures (figure 3.3i), self-assembly structures during the folding process (figure 3.3j), the totally folded 3D cubic structure (figure 3.3k), as well as the 3D self-folded cubic structure array on the glass substrate (figure 3.3l).

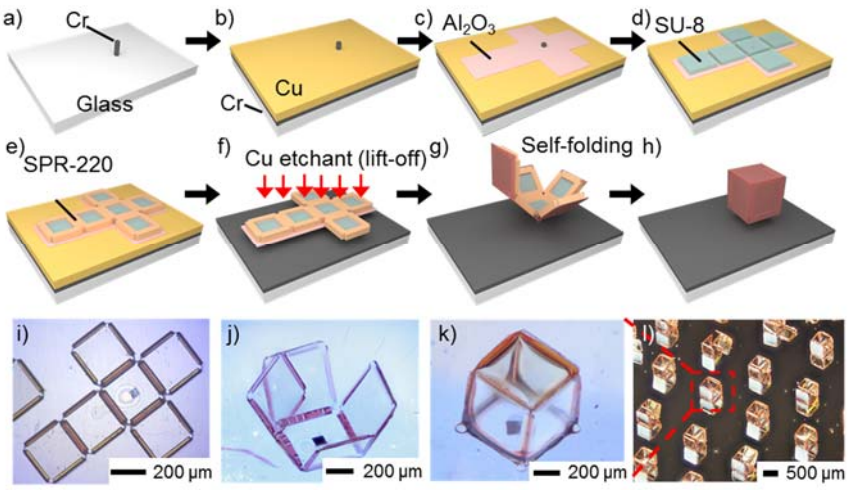

Figure 3.3 Fabrication of cubic structures for self-assembly on substrate [161]. (a-h) Illustration of the fabrication process of cubic structures on a glass substrate. (i-k) Optical images of a 2D micro structure (i), a half-folded micro structure (j), and a folded micro structure (k). (h) Optical image of a cubic structure array folded using remote-controlled microwave energy.

3.4.2 Anchorless structures

Since the substrate-free self-assembly requires the release of 2D structures from the substrate, the 1 μm thick Cr (Figure 3.3a) and Al_2O_3 pattern (figure 3.3c) are not necessary. A 10 nm thick Cr adhesion layer and 300 nm thick Cu sacrificial layer were deposited on the glass substrate using E-beam evaporation process (figure 3.4a and 3.4b). On top of the Cu sacrificial layer, a 150 nm thick SU-8 protection layer was patterned using a photolithography process (figure 3.4c), followed by a 100 nm thick Cr heat generation layer (figure 3.4d). A thicker Cr layer (100 nm) is used in this case to compensate the small area of Cr patterns and maximize the heat generation. 16 μm thick SU-8 panels and 24 μm thick PCL hinges were then patterned on the Cr layer (figure 3.4e and 3.4f). PCL hinge patterning process includes the preparation of PCL solution by dissolving PCL in tetrachloroethane [$Cl_2CHCHCl_2$] solvent, patterning of SPR-220 as sacrificial layer for PCL lift-off, spin-coating PCL solution on the sample and baking at 45 ^oC overnight to form PCL thin film and lifting-off PCL thin film to achieve PCL hinges. The 2D microstructures were then released from the substrate by etching the Cu sacrificial layer and transferred to a paper substrate (figure 3.4g). A single 2D structure was then placed in the microwave chamber for the substrate-free self-assembly (figure 3.4h). Optical microscopic images show the 100 nm thick Cr heat generation layer (figure 3.4i), 16 μm thick SU-8 panels on the Cr thin film (figure 3.4j), the fabricated 2D microstructures on the paper substrate (figure 3.4k), as well as the folded 3D cubic structure (figure 3.4l).

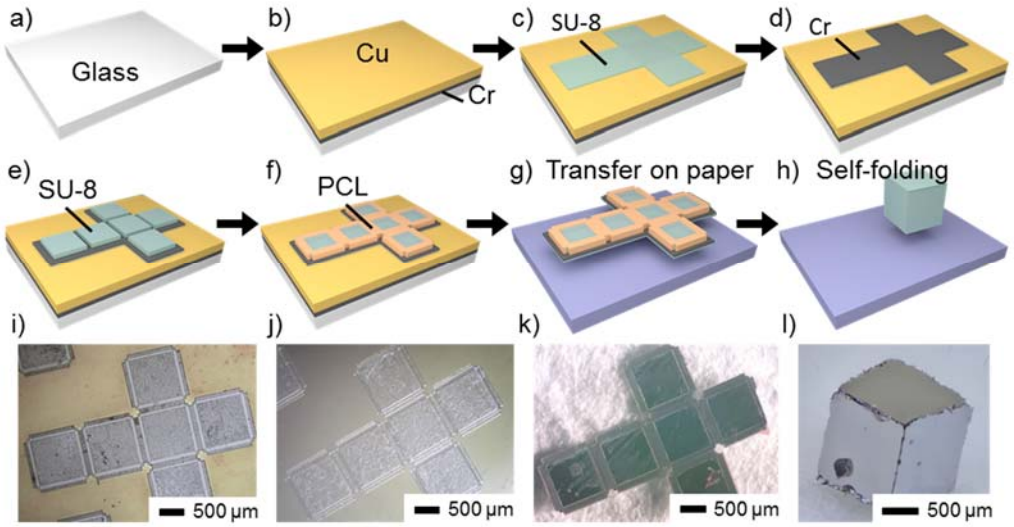

Figure 3.4 Fabricated of cubic structures for substrate-free self-assembly [161]. (a-h) Illustration of the fabrication process of cubic structures for substrate-free self-assembly. (i-k) Optical images of a 100 nm thick Cr pattern (i), SU-8 panels (j), and a 2D micro structure on paper (k). (h) Optical image of a cubic structure array folded using substrate-free remote-controlled microwave energy.

3.5 Hinge reflow analysis

To characterize the reflow of hinge materials for self-assembly, A 24 µm thick SPR-220 hinge was patterned on a glass substrate coated with a 20 nm Cr thin film [161]. The sample was then placed under the microwave radiations with a duration of 0 sec, 5 sec, 10 sec, and 15 sec respectively. Optical images of the top view (figure 3.5a-d) and cross-section view (figure 3.5e-h) of the SPR-220 hinges are shown after each microwave radiation. It can be clearly observed that the SPR-220 hinges start to reflow as the surface

temperature of the sample exceeds the melting point of the SPR-220 (60 ºC) at 5 sec and continue to melt as the microwave exposure time increases. The hinge reflow can be easily characterized by analyzing the contact angle of the hinge. As can be seen in figure 3.5e-h, the contact angle of the hinges decreases from 65 º to 35 º with the microwave exposure time increase (0 sec to 15 sec). The reduction of the contact angle illustrates the increase of the hinge reflow. To quantify the heat generation by eddy current heating inside the Cr thin film, an infrared camera (Seek Thermal CompactPro Thermal Imaging camera) was used to record the surface temperature of the sample during the microwave heating process at each exposure time (figure 3.5i-l). The temperatures taken from the center of the sample (indicated in figure 3.5i-l) were then calibrated using a thermocouple with an error of +/- 0.5 ºC. The calibrated surface temperatures of the sample were plotted and shown in figure 3.5m. The surface temperature of the sample (red line, figure 3.5m) increases from 28 ºC (room temperature) to 177 ºC in just 15 sec. The surface temperature, heat power generation, and thermal energy of the 20 nm Cr film can be modeled using Faraday's law of induction and specific heat [64, 65]. As the high frequency magnetic field (B) is applying to a thin metal film (Cr), the magnetic flux ($\Phi_B = B \times S$, where S is the surface area of the metal film) is created through the surface of the film. This magnetic flux (Φ_B) is accompanied by an electric field (E, where $\nabla \times E = - \partial B / \partial t$), which generates the eddy current (I) inside the metal film. The eddy current (I) circulates in the Cr film and flows against the resistance (R) of the Cr, results in the dissipation of energy as heat with a power dissipation (P) (equation 5). The surface temperature of the sample increases linearly with the increase of the microwave exposure time (t): $\Delta T = P \cdot t / C$, where ΔT is the surface temperature increase and C is the specific

heat capacity of the metal film (figure 3.5m). A good agreement between the experimental data and the modeled data can be seen in figure 3.5m. Figure 3.5n and 3.5o show the heat power generation (P) and the thermal energy ($Q = P \times t$) of the Cr film at different microwave exposure time respectively. The modeled power generation and thermal energy have a good agreement with the measurements.

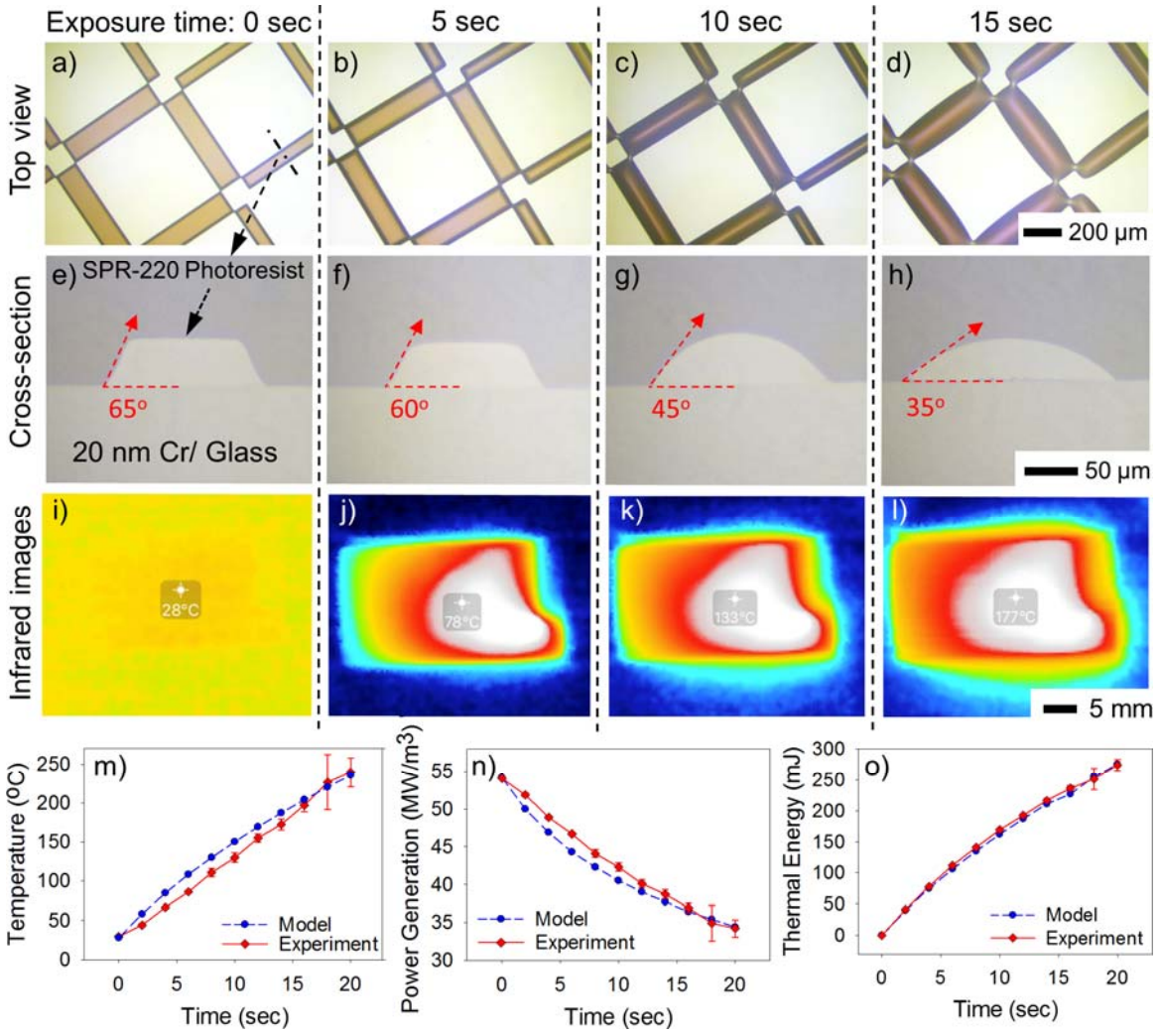

Figure 3.5 Hinge reflow and surface temperature analysis of micro-structures [161]. (a-d) Top view of the reflow process of 24 µm thick SPR-220 photoresist hinges with microwave exposure time from 0 sec to 15 sec. (e-h) Cross-section view of the corresponding hinge reflow shown in (a-d). Contact angle of the SPR-220 hinge varies

from 65° to 35°. (i-l) Surface temperatures of the 20 nm thick Cr film were captured using an infrared camera. (m) Surface temperature, (n) heat power generation, and (o) thermal energy generating within the 20 nm Cr film with different microwave exposure time were modeled and measured.

3.6 Self-assembly of cubic structures

3.6.1 Anchored structures

The remote-controlled self-assembly with an anchored design can be created with a 20 nm thick Cr film deposited on a glass substrate (10 ×10 mm^2) for the realization of an array of 3D microstructures (figures 3.6a-c, zoomed-in images are shown in figure 3.6d-f) [161]. For self-assembly of anchored structures, SPR-220 resist is used as the hinge material due to its easy fabrication process. As the surface temperature of the sample increases to the melting point of the SPR-220 (around 100 °C), the SPR-220 reflows and generate surface tension force to lift up the SU-8 panels and transform 2D microstructures into 3D cubic structures.

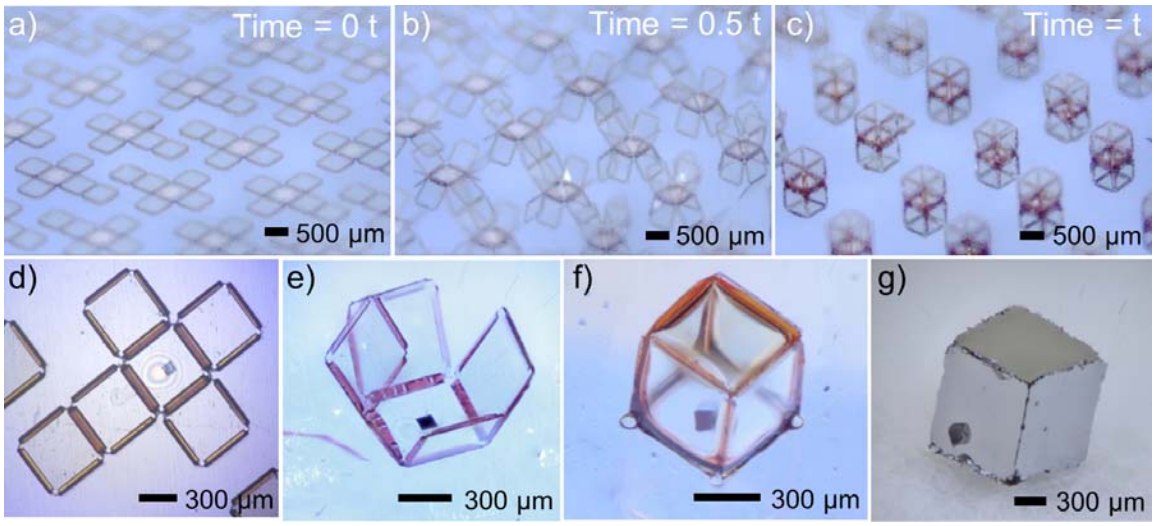

Figure 3.6 Micro-scale 3D cubic structures for remote-controlled self-assembly [161]. (a-c) Real-time self-assembly process images of the cubic structures on a glass/ 20 nm thick Cr substrate. Images are captured using an optical microscope and camera at different microwave exposure time of (a) 0, (b) 0.5 t, and (c) t. (d-f) Zoomed-in optical images of a micro-structure shown in (a-b). (d) A 2D, (e) a half-way folded, and (f) a fully folded cubic structure are captured. (g) Optical image of an anchorless folded cubic structure with a 100 nm thick Cr film on the surface of SU-8 panels.

3.6.2 Anchorless structures

For anchorless structures, a 3D microstructure can be self-assembled on a paper substrate (figure 3.6g) [161]. The entire 2D structure containing SU-8 panels and PCL hinges was first fabricated on a glass/Cr/Cu substrate. The Cu sacrificial layer was then etched away using Cu etchant to completely release the 2D microstructures from the substrate. The released structure was then transferred from the Cu etchant to DI water to remove excessive Cu etchant. The structures were then transferred to a paper substrate

upon self-assembly. The anchorless design allows the self-assembly of single microstructure, increasing the accessibility and controllability of the assembly process. The ability to remote self-assemble individual microstructure also allows the assembly process to be conducted in a restricted environment where energy source is not accessible or difficult to handle. One drawback of such anchorless design is that the local heat source (Cr thin film) area is relatively small (same as the size of the SU-8 panels) compared to anchored design, which dramatically reduces the heat generation. The low heat generation makes it difficult for the surface temperature of the sample to reach to the melting point of the SPR-220 hinges (100 ºC). To solve this problem, PCL hinges with a melting point of 60 ºC was used to replace the SPR-220 hinges to trigger the self-assembly with anchorless design (figure 3.6g).

3.7 Folding analysis

To numerically analyze the folding process of the microstructures, the folding angles of the SU-8 panels on a glass/Cr substrate (Cr thickness = 20 nm) was captured using a microscope and a camera at different microwave exposure times (figure 3.7a-d) [161]. The folding angle of the panels remains 0 degree before 6 sec of microwave exposure because the surface temperature has not reached to the melting point of the hinge (100 ºC) (figure 3.7a). After 6 sec of microwave exposure, the surface temperature of the sample reaches to 100 ºC and the SPR-220 hinges start to reflow and triggers the folding of the panels (figure 3.7b). The SU-8 panels were folded from 0 degree to 90 degree in 10 sec (figure 3.7d). Due to the locking mechanism of the SPR-220 hinges surrounding the

panels, the folding angle of the panels remains 90 degree even when the microwave energy continues to be applied to the structure. To quantitatively analyze the assembly process, an equation of folding angles (θ) was derived with the assumption that the folding angle of the panels is proportional to the thermal energy generated by the eddy current heating:

$$\theta = \frac{\alpha \cdot \pi^2 \cdot B_p^2 \cdot f^2 \cdot A \cdot d^3 \cdot (t-\beta)}{6 \cdot \kappa \cdot C \cdot \rho} \tag{7}$$

where α is a constant of 2.7×10^{-18}, presenting the coefficient of the proportionality. The value of α was obtained by using the curve fitting process between the experimental data and the modeled data. The same α value was applied to all models shown in figure 3.7e-g, which proves good agreements between the model and the measurement. The parameter β is the initial time at which the assembly starts. The value of β differs with different parameters of the microstructure and different microwave settings. The hinge effect to the folding performance was minimized by using the same hinge geometry (thickness, width, and length) for all the experiments. The parameter α accommodates for all the geometry changes occurs for different microstructures. It can be observed that as the Cr thickness (d) increases, the time (t) it took to fold the panel to 90 degree decreases (figure 3.7e) due to the cubed term (d^3) in equation (7). The high thermal generation of the thick Cr also results in a high angular folding speed (figure 3.7f). It can also be concluded from figure 3.7e and 3.7f that the initial start folding time also varies depends on the thickness of the Cr: 10 nm Cr: 6 sec, 15 nm Cr: 8 sec, and 20 nm Cr: 20 sec. As the Cr thickness (d) increases, the thermal heat generation also increases, leads to a shorter time for the sample surface temperature to reach to the melting point of the SPR-220 hinges (100 ^{o}C), thus results in an early initial folding time (figure 3.7g).

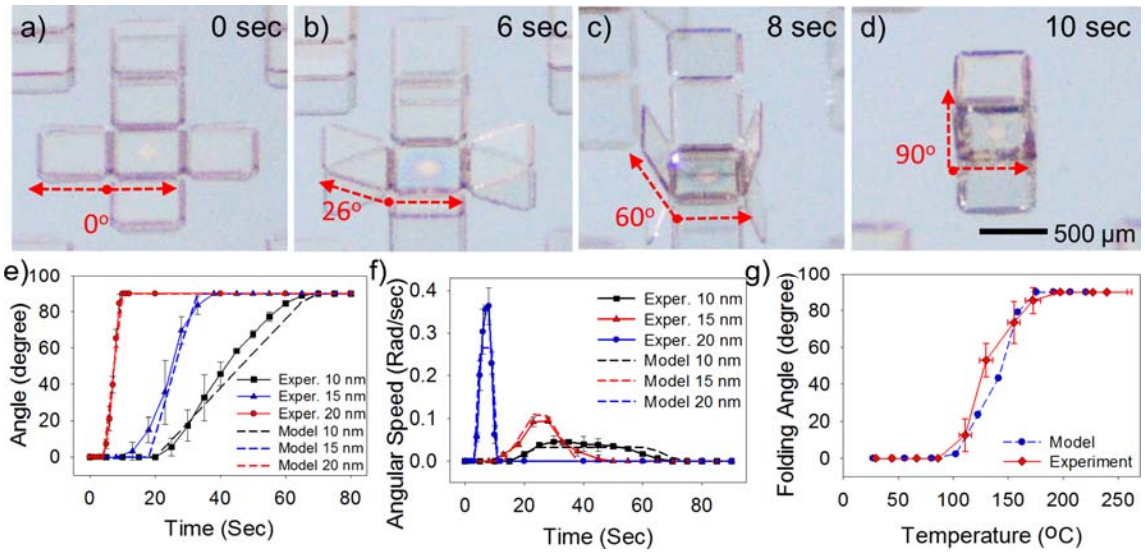

Figure 3.7 Folding angle analysis with different Cr thicknesses [161]. (a-d) Real-time optical images of self-assembly on glass substrate with 20 nm Cr. (e) Folding angle and (f) angular speed of cubic structure with different Cr thicknesses (10 nm, 15 nm and 20 nm) were modeled and measured. (g) Folding angles of cubic structure with a 20 nm Cr film at different temperatures. The angles vs. temperatures modeled from equation (2) shows a good agreement with measurements.

3.8 Multiple and sequential assembly

3.8.1 Multiple and sequential assembly theories

Due to the thermal energy and surface temperature's dependence to the thickness of the Cr films (within the skin depth of the Cr, which is around 3 μm at 2.46 GHz) (equation 7), multiple and sequential self-assembly can be designed. To realize multiple and sequential self-assembly, microstructures with Cr films locally patterned at multiple

hinge areas with different thicknesses (10 nm, 50 nm, and 100 nm respectively) were designed (figure 3.8) [161]. The increase of the Cr thickness (figure 3.8a) results in an increase of the eddy current heat generation (figure 3.8b), leading to a higher temperature, an early folding time, and a larger folding angle (equation 7) (figure 3.8c).

3.8.2 Sample design

In order to illustrate the multiple and sequential self-assembly, SU-8 panels and PCL hinges were used to create the microstructure [161]. Instead of depositing the Cr thin film under the entire structure (panels and hinges), the Cr films with different thicknesses (10 nm, 50 nm, and 100 nm) were selectively patterned on multiple hinge areas (figure 3.8a and d). The microstructure with Cr was then released from the substrate by Cu etching and was transferred to a paper substrate upon self-assembly.

3.8.3 Folding angle analysis

When the microwave energy was remotely applied to the microstructure, Cr film with different thicknesses (10 nm, 50 nm, and 100 nm) can generate different amount of thermal energies, which melts the PCL hinges and trigger the self-assembly [161]. Since the 10 nm Cr has the least heat generation, the PCL hinge adjacent to the 10 nm Cr has the smallest folding angle of only 20 degree and will fold the last (figure 3.8e and f). On the other hand, the PCL hinges adjacent to the 50 nm Cr and 100 nm Cr will have a larger folding angle of 90 degree and 175 degree respectively due to the larger heat generations

of the 50 nm and 100 nm Cr (figure 3.8e, f). Thus multiple and sequential self-assembly can be easily achieved.

3.8.4 Advantages of multiple and sequential assembly

The ability of self-assembly with sequential folding processes and multiple folding angles makes it easy to fabricate complex 3D microstructures and largely broaden the applications of 3D self-assembled microstructures like microbots, micro-actuators, and 3D micro-optic devices. Since large Cr thickness (d in equation 5) results in a large eddy current power generation (P in equation 5), the thermal energy (Q in equation 6) and temperature rise (T in equation 6) are also large. The higher temperature leads to a shorter time for the hinge to reach to its melting point. Thus the panel connected with thinner Cr film will fold first, followed by a panel with thicker Cr film. Sequential assembly makes it possible to assemble multi-panel structures without any collisions, which is beneficial for building complex and multifunctional microstructures.

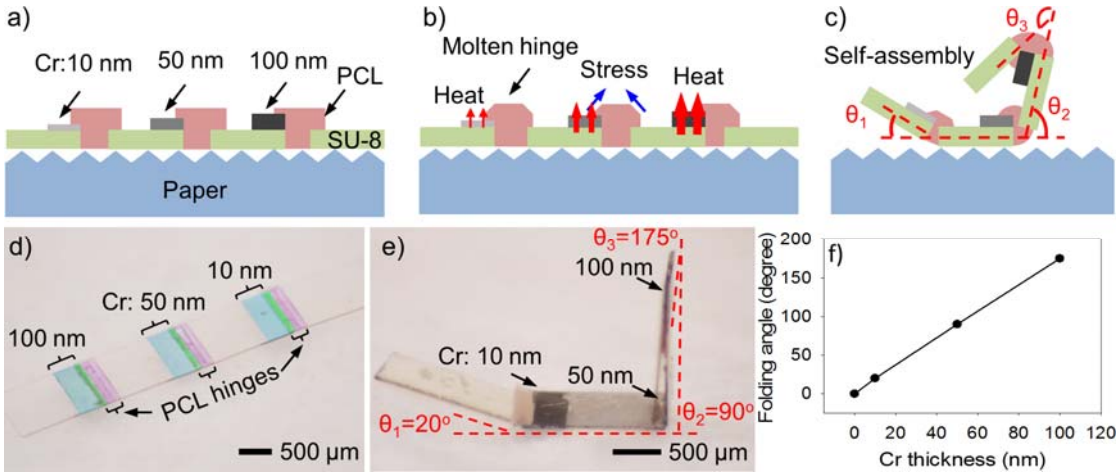

Figure 3.8 Remote-controlled self-assembly with multiple folding configurations [161]. (a-c) Illustration of self-assembly with multiple hinges. (a) Cr with different thicknesses (10 nm, 50 nm and 100 nm) were patterned adjacent to the PCL hinges on top of SU-8 Panels. (b) Different amounts of heat are generated from the Cr depending on its thicknesses. (c) Self-assembled structures with different folding configurations show multiple folding angles. (d, e) Optical images show the micro structure with (d) multiple hinges before assembly and (e) the folded structures with multiple folding angles. (f) Measurement data shows different folding angles of the panels corresponding to different Cr thicknesses.

Chapter 4

Remote-Controlled Induction Driven Self-Assembly

4.1 Theory of induction driven self-assembly

A remotely controlled self-assembly process driven by induction energy is developed. A high frequency (5 MHz) magnetic field is introduced using an induction system. The magnetic field produces localized heating through eddy current inside the metal panels of the micro-scale structures. The localized heat increases the surface temperature of the sample, which is high enough to melt the polymer hinge to trigger the self-assembly. The advantage of the induction driven remote-controlled self-assembly is that the energy source (induction energy) can be remotely applied to the sample during the assembly process, increasing the manipulative capability of the process. The induced induction magnetic field is biocompatible and is safe to use in living tissues and organs. Since the heat is only generated on the surface of metal panels, the temperature increase during the assembly process is only limited at the micro-scale structure, which limits the harm of heat to the surroundings to minimum. In addition, PCL is used as the hinge material, which has a low melting point of around 60 ºC. The low melting point of the PCL hinge allow the self-assembly at a low temperature, which further improves the biocompatibility of the process. Thus, the induction driven remote-controlled self-

assembly is suitable for various biomedical applications like cell encapsulation, culture and organization, and smart drug delivery.

4.1.1 Induction induced eddy current

The induction driven self-assembly is illustrated in figure 4.1a. The high frequency (5 MHz) time-varying magnetic field is provided using an induction coil connected with a high frequency induction circuit and a power supply. The 2D microstructure to be assembled is placed on a paper substrate on top of the induction coil upon self-assembly. The sample is located in the center of the coil in order to obtain uniform magnetic field. The purpose of the usage of the paper substrate is to minimize the effect of the substrate to the induction heating process since the paper substrate does not generate any heat during the induction magnetic field and the magnetic field can penetrate through the paper without any interruption. The mechanism of induction driven self-assembly is illustrated in figure 4.1b. The 2D microstructure is made of Ni panels and PCL hinges. As Faraday's law of induction indicates, eddy current (red line, figure 4.1b) can be created inside the Ni panels when the high frequency magnetic field (blue line, figure 4.1b) is applied to the sample [175, 176]. The eddy current is circulating inside the Ni panels and flows against the resistance of the Ni to dissipate energy as heat (Joule's law) [177-180]. The generated heat energy will melt the PCL hinges and generate surface tension force to lift up the Ni panels and transform a 2D microstructure to a 3D structure. The eddy current power generation can be calculated using equation 5 [181]. Such remote-controlled self-assembly can be easily realized by tuning the power of the magnetic field as well as the geometric

parameters of the microstructures. Induction induced magnetic field operates at a frequency of 5 MHz, which is high enough to generate heat to trigger the self-assembly process but low enough not to harm human bodies and living tissues and organs [199].

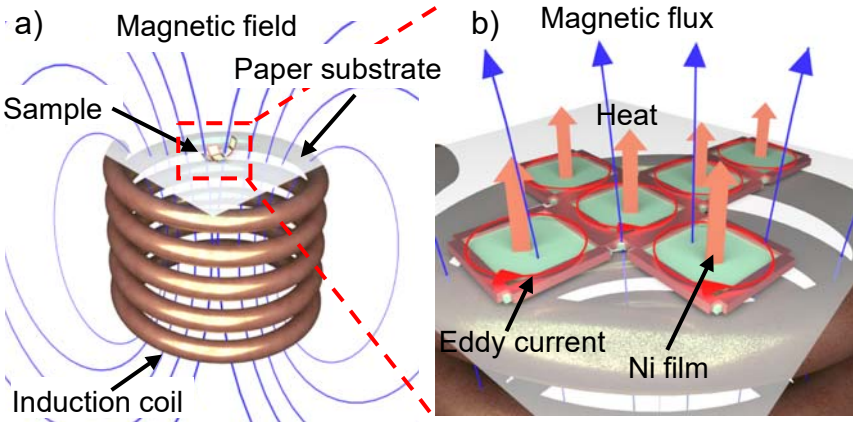

Figure 4.1 Illustration of induction driven self-assembly for biomedical applications. (a) Induction coil generates high frequency magnetic field penetrating through the sample on a paper substrate. (b) The magnetic field (blue line) creates eddy current (red line) in the Ni panels of the sample. The eddy current flows against the resistance of the Ni and generates heat.

4.1.2 Eddy current driven self-assembly

A detailed schematic of the induction driven self-assembly is shown in figure 4.2a – 4.2c. The 2D sample is made of Ni panels and PCL hinges, which is supported by a thin layer of Al_2O_3. The entire structure is placed on a paper substrate upon self-assembly (figure 4.2a). The magnetic field (blue line, figure 1a) is applied to the Ni panels of the structures and create eddy current inside the Ni panels. The eddy current flows against the

resistance of the Ni and dissipates energy as heat (red line, figure 4.2a) that melts the PCL hinges and creates surface tension force (figure 4.2b) necessary to transform 2D structures to 3D structures (figure 4.2c).

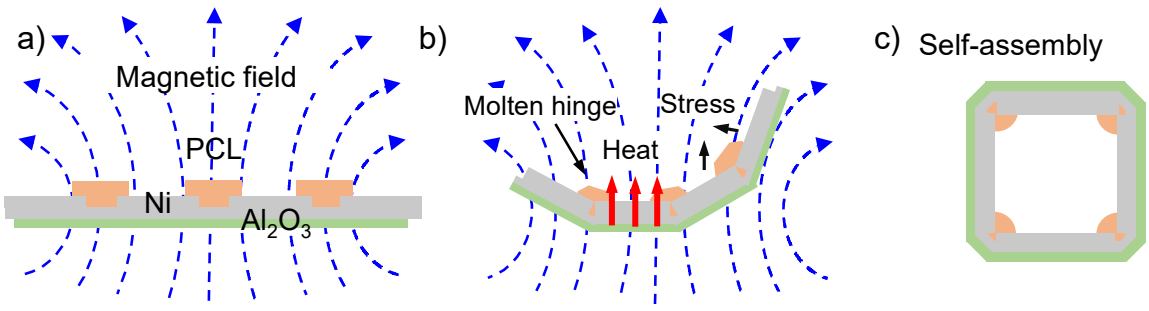

Figure 4.2 Eddy current driven self-assembly (a) A cross-section of the structure shows the Ni panels, PCL hinges and Al_2O_3 supporting layer. The magnetic field (blue line) penetrates through the sample. (b) Heat is generated due to the eddy current, which melts the PCL hinges. The molten hinge creates surface tension stress to lift up the panels. (c) A totally self-assembled structure.

Various metals can be used as the panel materials to induce eddy current and heat generation to trigger the induction driven self-assembly process including ferromagnetic materials (e.g., Ni, iron (Fe), and cobalt (Co)) and non-ferromagnetic materials (e.g., aluminum (Al), and Cu). Both types of materials can generate eddy current under high frequency electromagnetic fields and exhibit heat due to the resistance inside the metal. However, the amount of heat generated from different metals varies depends on the electrical and physical properties of the metal [200]. For example, normally, ferromagnetic materials (e.g., Ni, Fe, Co) have higher resistivity compared to non-ferromagnetic materials (e.g., Al, Cu), which results in more Joule heat generation if same eddy current

is introduced in the metal [200]. Ferromagnetic and magnetic materials also have hysteresis losses when exposed to electromagnetic fields. Hysteresis is the effect that the magnetic dipoles inside the metal oscillate due to the applied electromagnetic field, results in additional friction heat generation [200]. In addition, the temperature increase by induction heating also depends on the specific heat (ability to absorb heat) of the material. Al has a much lower specific heat compared to Ni, meaning that it takes Al less thermal energy to heat up to a high temperature compared to Ni [200].

4.2 Induction system setup

The induction heating system setup of the induction driven self-assembly is shown in figure 4.3. The induction coil is made of Cu wires and is connected with an induction circuit that can generate a 5 MHz time-dependent magnetic field (figure 4.3a) [201]. The induction circuit is supplied by a power supply with a maximum power of around 200 W. The 5 MHz induction circuit can be seen in figure 4.3b. The induction coil has 9 turns with a diameter of 1 cm and a length of 1.5 cm. The diameter of the Cu wires that are used to make the induction coils is 1 mm. A water-cooling system is used to cycle cold water (around 10 ^{o}C) around the induction coils to guarantee that the coil itself does not get heat up. The sample placed on top of the induction coil is monitored by two separate camera systems: (a) the optical camera and microscope are used to record the self-assembly of the microstructures; (b) The infrared camera system is also used to capture the surface temperature of the sample during the self-assembly process. The values for each component of the induction circuit are listed below. Resistor R1 = 1kohm, R2 = 0-4.7

kohm, R3 = 1 kohm. Capacitor C1 = 2.2 nF, C2 = 1.5 nF, C3 = 10 uF, C4 = 20 nF. Zener diode D1 = 6V. Q1: N-channel MOSFET IRFP 460.

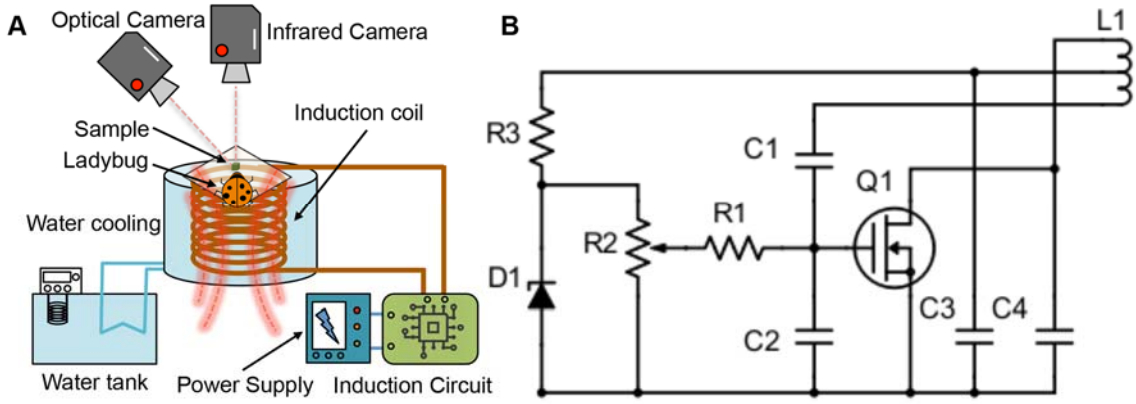

Figure 4.3 Induction system setup for the induction driven self-assembly.

4.3 Sample design and fabrication

4.3.1 Substrate, panels, and hinges

The structure used for induction driven self-assembly contains Ni panels and PCL hinges. The Ni panels are around 20 μm thick and the PCL hinges are around 25 μm thick. The entire structure is fabricated on a glass or Si substrate with 10 Cr seed layer and 300 nm Cu sacrificial layer. The complete fabricated structure is then released from the substrate by etching the Cu sacrificial layer and placed on a paper substrate upon self-assembly.

4.3.2 Fabrication process

Details of the fabrication process of the induction driven self-assembly are shown in figure 4.4. First, a 10 nm Cr adhesion layer and a 300 nm Cu sacrificial layer was deposited on a glass substrate using e-beam evaporation (figure 4.4a). A 30 nm Al_2O_3 layer was then patterned on the Cu sacrificial layer (figure 4.4b). The purpose of the Al_2O_3 layer is to support the entire structure (panels and hinges) and to prevent the hinges from sticking to the substrate. A 100 nm Ni layer was then patterned on the Al2O3 supporting layer used as the Ni electroplating seed layer (figure 4.4c). The Ni seed layer is slightly larger than the Al2O3 layer to guarantee the connection between the Ni and the Cu layer. Ni panels were then patterned on top of the Ni seed layer using Ni electroplating process (figure 4.4d). The PCL hinges were then patterned between the Ni panels (figure 4.4e). The Cu sacrificial layer is etched away to release the sample from the substrate (figure 4.4f). The sample is then transferred to a paper substrate upon self-assembly (figure 4.4g) Induction systems were used to generate time-dependent magnetic field, which is applied to the structure to trigger the self-assembly process. Figure 4.4i-l shows the optical images of the 2D microstructure during each fabrication steps as well as a complete assembled 3D structure: (I) A 30 nm Al_2O_3 supporting layer on the Cu/Cr/Glass substrate. (J) A 100 nm Ni electroplating seed layer pattern. (K) The electroplated Ni panels. (L) A totally self-assembled microstructure on a paper substrate.

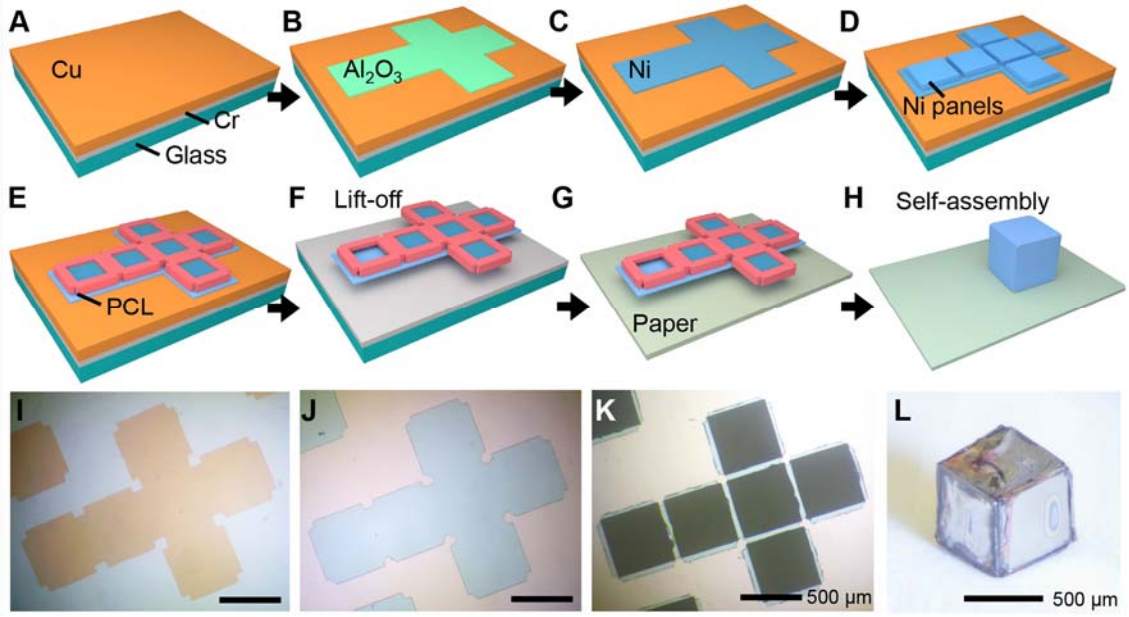

Figure 4.4 Fabrication details of the micro-scale structures for induction driven remotely controlled self-assembly.

4.4 Thermal analysis

4.4.1 Surface temperature modeling overview

To analytically characterize the eddy current heat generation of the Ni films, surface temperatures of the Ni panels were recorded and analyzed with an infrared camera (Seek Thermal CompactPro Thermal Imaging camera), shown in figure 4.5a and b. The panel size of the sample used is 500 μm × 500 μm with a Ni thickness of 15 μm. The induction input power for this temperature experiment is 200 W. The temperatures were taken at a specific point on the surface of the Ni panels (indicated in figure 4.4a and 4.4b) and were calibrated using a thermocouple to obtain the accurate temperature reading.

Upon turning on the power of the induction heating system, the surface temperature of the Ni panels remains at 19 ºC (figure 4.4a). When the induction magnetic is applying to the Ni panels, the surface temperature of the sample increases from 19 ºC to 37 ºC in just 10 sec (figure 4.4b). The temperature of its surroundings remains the same as the initial temperature of the sample (around 19 ºC). This rapid heat generation and surface temperature raise is the driven force of the self-assembly process.

4.4.2 Surface temperatures with different film thickness

To quantitatively analyze the temperature changes on the surface of the sample, the surface temperature of the sample with different Ni thicknesses (figure 4.4c), different Ni panel areas (figure 4.4d), and different induction input power (figure 4.4e) were measured and modeled used on equation 5 and 6. As the Ni thickness (d) increases, the eddy current power generation (P) also increases based on equation 5, leading to the increase of the surface temperature (T) (equation 6). Ni panels with various thicknesses (1 μm, 5 μm, and 10 μm) were tested with the induction input power of 120 W. The area (A_s) of each Ni panel is 500 μm × 500 μm. The surface temperatures (T) of the samples were measured using an infrared camera within the period of time from 0 sec to 60 sec (figure 4.4c). As expected, the 15 μm thick Ni sample reaches the highest temperature of 40 ºC at 60 sec, while the 5 μm and 1 μm thick Ni samples reach the highest temperatures of 30 ºC and 25 ºC respectively.

4.4.3 Surface temperatures with different panel areas

For the Ni samples with the same thickness (d =15 μm) but different panel areas (As) of 200 μm × 200 μm, 500 μm × 500 μm, and 1000 μm × 1000 μm, the highest temperature of 90 ºC can be achieved with the largest panel size (figure 4.4d). The surface temperature (T) decreases with the decrease of Ni panel size (A_s). This can be explained by equation 5 and 6, where the power (P) of induction increases when the area (A_s) of the metal thin film increases, leading to a high heat generation ($W = P \bullet t$), thus a high surface temperature (T).

4.4.4 Surface temperatures with different induction powers

Lastly, the Ni panel eddy current heat generation was studied under different induction input powers (figure 4.4e). The samples with 5 μm thick Ni (d) and a panel size (A_s) of 500 ×□500 μm^2 was tested under various induction input powers (80 W, 120 W, and 200 W). The induction magnetic field intensity (B_0) is proportional to the input power of the induction circuits. A high input power of the induction circuit can generate a strong magnetic field (B_0), which results in a high eddy current power generation (P) shown in equation 5. A high eddy current power generation can results in a large thermal energy generation and leads to a high surface temperature of the sample (equation 6). In figure 4.4e, a highest temperature of 60 ºC can be observed with the input power of 200 W, while the temperatures of the Ni samples with 80 W and 120 W input powers are 30 ºC and 40 ºC respectively. For all the temperature analysis, the surface temperature (T) of the

samples increases with an increase of induction exposure time (t). It can be explained by the heat generation equation $W = P \bullet t$. Also, it can be observed from figure 4.4c-e that the temperature increase starts to saturate at high temperature. This is because of the high conductive and convective heat loss of the Ni panels at a high temperature.

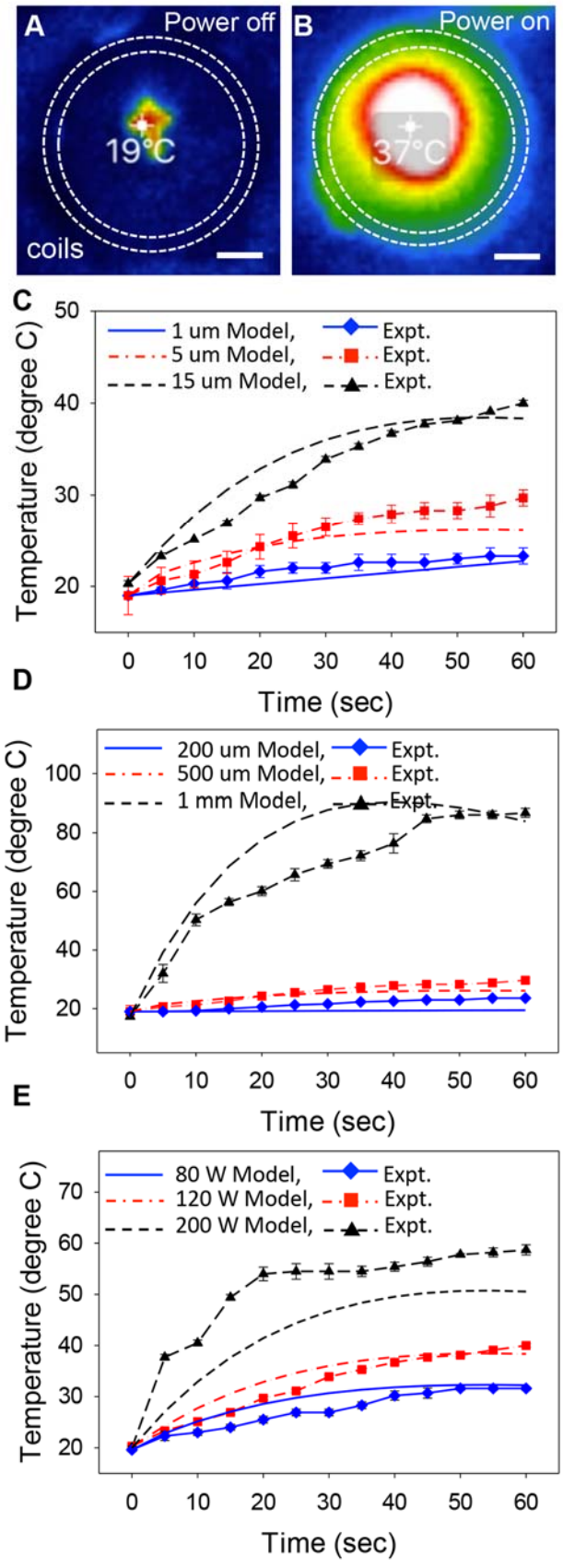
A
Power off
19°C
coils
B
Power on
37°C
C
Temperature (degree C)
1 um Model,
5 um Model,
15 um Model,
Expt.
Expt.
Expt.
Time (sec)
D
Temperature (degree C)
200 um Model,
500 um Model,
1 mm Model,
Expt.
Expt.
Expt.
Time (sec)
E
Temperature (degree C)
80 W Model,
120 W Model,
200 W Model,
Expt.
Expt.
Expt.
Time (sec)

Figure 4.5 Thermal analysis of the induction heating process for remotely controlled self-assembly

To verify the reliability of above temperature modeling and measurement, simulations of the surface temperatures of Ni thin films under induction radiations were conducted using COMSOL Multiphysics (figure 4.6). To simplify the simulation process, 2D Ni panels were replaced by Ni thin film plates with the sample total surface area in the simulator. The Ni plate was then placed on the paper substrate above the induction coils. Actual coil temperatures were monitored during the assembly process and then applied to the coil in the simulator. As shown in figure 4.6, the surface temperature of Ni plates increases from 18 ºC to 58 ºC in 60 sec. The simulated surface temperature agrees well with the temperature measurement of the Ni panels. The slight difference between the simulated and measured data is due to the shape difference between the Ni panels and the Ni plates and the variations of induction frequency and power in the measurement.

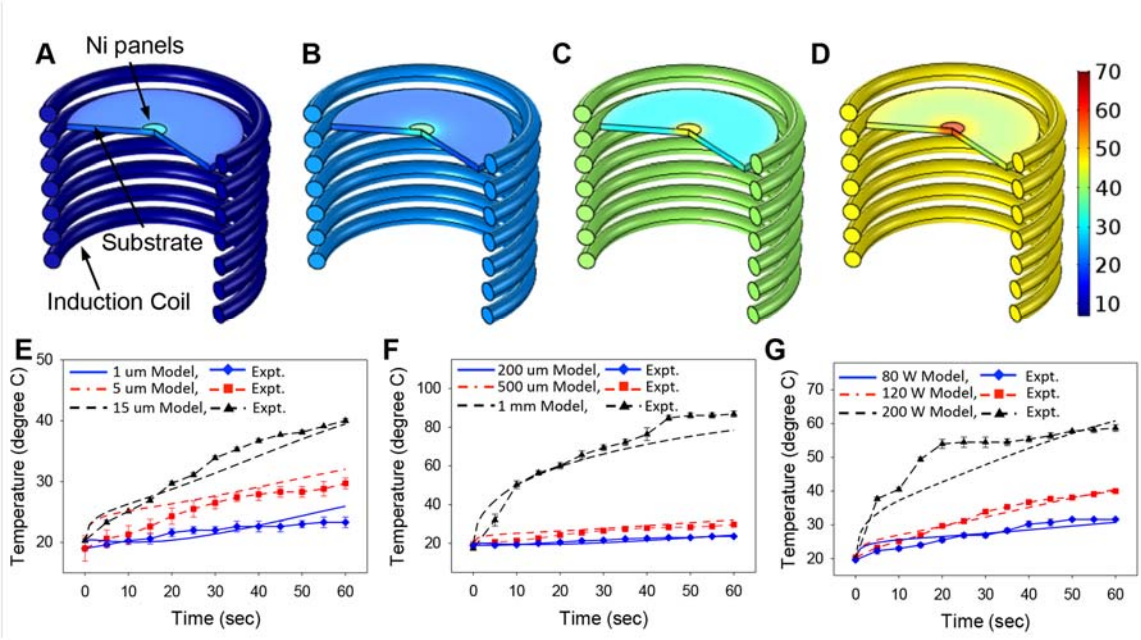

Figure 4.6 COMSOL modeling of the induction heating process for the remotely controlled self-assembly.

4.5 Self-assembly of cubic structures

4.5.1 Overview

The high surface temperature of the Ni panels (over the melting point of the PCL hinge material) results in the melting of the PCL hinges. The molten hinges generate surface tension forces to lift up the panels and trigger the self-assembly process. To analyze the folding performance of the Ni panels, the self-assembly process was monitored using a camera and a microscope (figure 4.7a-d). The sample used has a panel size (A_s) of 500 μm × 500 μm and a Ni thickness (d) of 20 μm. The input power of the induction circuit is 200 W. As shown in figure 4.7a-d, the folding of the Ni panels started

when the surface temperature of the sample exceeded the melting point of the PCL hinges (around 60 ºC). Under the induction magnetic field, the surface temperature of the Ni continues to increase due to eddy current heat generation within the Ni panels, leading to the further melt of the hinges and a completely self-assembly of the microstructure (figure 4.7d). The top panel of the cubic structure shows slower folding behavior compared to other panels (figure 4.7c) due to the higher position of the top panel above the induction coil, leading to a weaker magnetic field, thus a smaller heat generation. The magnetic field of a solenoid outside the coils can be expressed using Biot-Savart Law [179-182]: $B(z) \sim \mu_0 \cdot i \cdot A/(2 \cdot \pi \cdot z^3)$, where $B(z)$ is the magnetic field at a distance z away from the solenoid, μ_0 is the permeability of free space, i is the current inside the solenoid, and A is the cross-section area of the solenoid. It can be seen that the magnetic field strength B decreases exponentially with the increase of the distance z, leading to dramatic reduction of the heat generation based on equation 5 and 6. Thus the folding for the top panel is slower compared to other panels (equation 7).

4.5.2 Folding angle and angular speed analysis

The folding angle (figure 4.7e) and angular speed (figure 4.7f) of the Ni panels during the self-assembly process was also studied using a camera and a microscope and modeled based on equation 5-7. It is assumed that the folding angle of the panels is proportional to the surface temperature of the sample in a period of time after the surface temperature of the sample reaches the melting point of the hinge. It can be observed from figure 3e that the folding angle of the panels increases from 0 degree to 90 degree in 10

sec. It indicates that a totally assembled 3D micro-scale structure can be achieved in 10 sec. The folding speed of the Ni panels (figure 2f) initially increases with the increase of induction radiation time due to the constant increasing of the surface temperature. As the panels continue to fold up (away from the induction coil), the amount of heat generated is reducing because of the weak magnetic field (B_0) at a higher position, leading to the decrease of the folding speed. The maximum folding speed of 25 degree/sec is achieved at the induction radiation time of 4 sec. The folding speed continues decreasing to 0 degree/sec when the folding angle reaches to 90 degrees. The folding angle of the Ni panels is also monitored at different surface temperatures (T) (figure 4.7g). The folding angle of the panels remains at 0 degree before the surface temperature of the sample reaches 60 ^{o}C (melting point of the PCL hinges). After the folding angle reaches 90 degree, the increase of surface temperature will not affect the folding angle due to locking mechanism of the hinges and the panels. The measured measurement data in figure 4.7e-g agrees well with the modeling data.

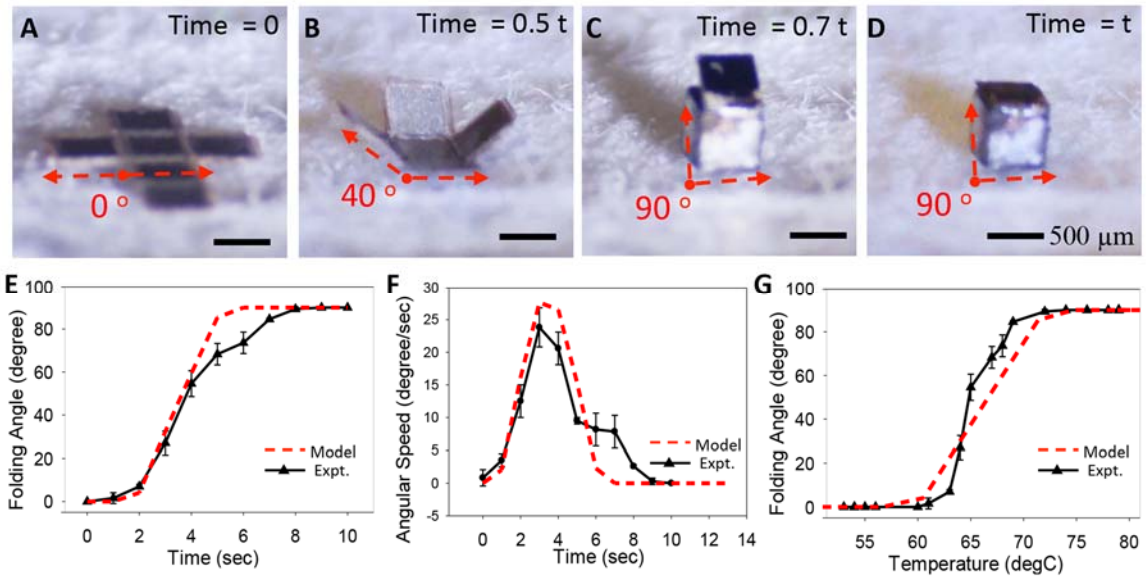

Figure 4.7 Remotely controlled self-assembly of micro-scale cubic structures using induction energies.

4.6 Reticulum beef tripe experiment

4.6.1 Beef tripe experiment overview

Induction driven remote-controlled self-assembly has the potential for biomedical application due to the biocompatibility of the induction energy source. In order to achieve self-assembly in biomedical applications, the induction magnetic field needs to penetrate through biomaterials and reaches to the sample to generate localized heat and trigger the self-assembly process. To show that the heat generation of induction driven self-assembly is localized on the sample and that induction magnetic field can penetrate through

biomaterials and realize self-assembly inside biological environments, the sample is self-assembled through reticulum beef tripe driven by induction energies (figure 4.8).

4.6.2 Self-assembly in beef tripe

The self-assembly through beef tripe is illustrated in figure 4.8a-d. Induction coil is used to provide the magnetic field for heat generation (figure 4.8a, b). The induction coils are connected with a water-cooling system to guarantee that the induction coils do not get heated. The sample to be assembled was placed inside the beef tripe honeycomb chamber on top of the induction coils (figure 4.8b). The induction magnetic field penetrates though the beef tripe and creates eddy current inside the Ni panels of the sample (figure 4.8b). The eddy current generates heat energy and melts the PCL hinges, triggering the self-assembly process of the microstructures inside the beef tripe honeycomb structure (figure 4.8c and d). Optical images show the beef tripe honeycomb structure (figure 4.8e), the 2D microstructure inside the beef tripe honeycomb (figure 4.8f), and the self-assembled 3D structure inside the beef tripe honeycomb (figure 4.8g). The self-assembly of microstructure inside beef tripe honeycomb chamber illustrates the ability of the induction magnetic field to penetrate through biomaterials and realize the assembly inside a confined bio-environment.

4.6.3 Thermal analysis

The thermal analysis of the beef tripe experiment is conducted using an infrared camera as shown in figure 4.8h-j. The surface temperature of the beef tripe is around 10 ºC. This is because of the refrigerated storage condition of the beef tripe upon the experiment (figure 4.8h). The surface temperature of the sample before self-assembly is at room temperature (around 25 ºC) (figure 4.8h). When the induction magnetic field is applied to the beef tripe and the sample, the surface temperature of the sample increases to 60 ºC while the surface temperature of the beef tripe remains the same (figure 4.8i and 4.8j). This further proves that the induction driven self-assembly can trigger the localized heat generation, which is beneficial for biomedical applications.

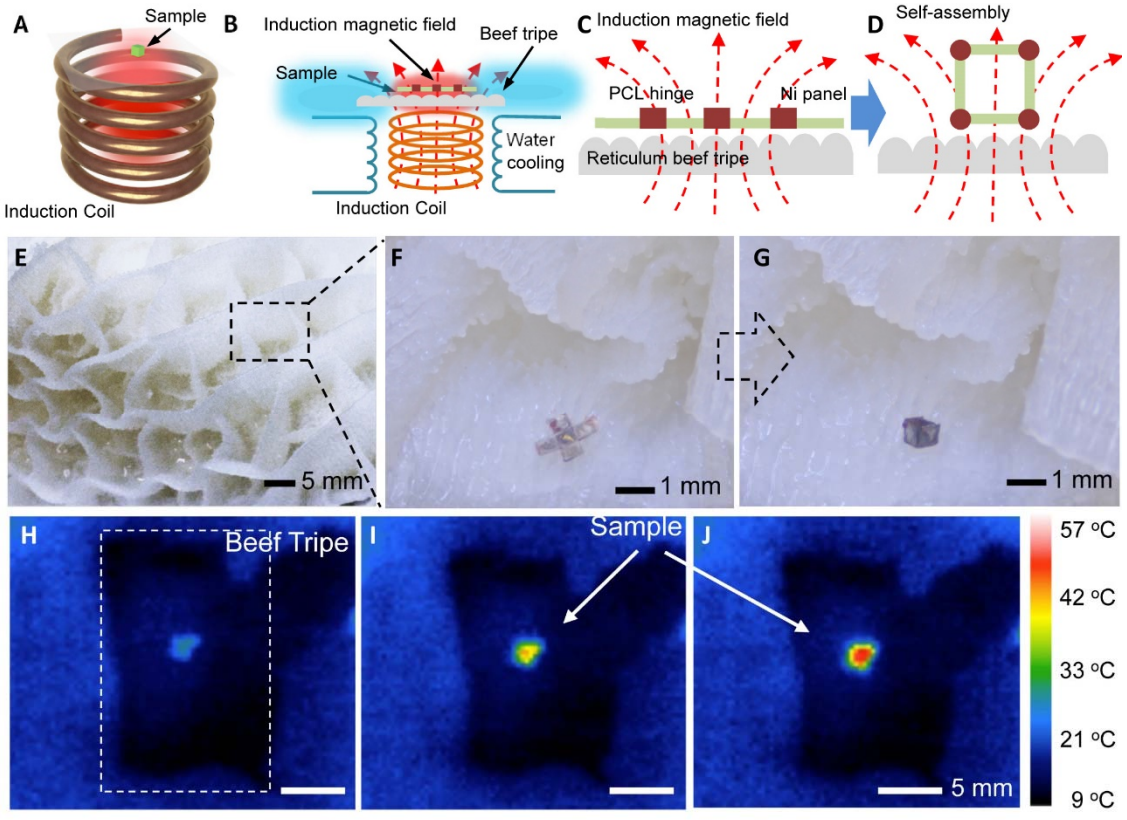

Figure 4.8 Reticulum beef tripe experiments for induction driven self-assembly. (A-D) Illustration of the induction driven self-assembly on beef tripe. (A) Magnetic field is generated using an induction coil. (B) The coil temperature remains low due to the water-

cooling system. A beef tripe is placed on top of the coil as a substrate. The sample to be self-assembled is placed on the beef tripe. (C) Magnetic field penetrates through the beef tripe and reaches the Ni panels of the sample. The eddy current is generated inside the Ni panels and produce heat. (D) Heat melts the PCL hinges and triggers the self-assembly process. (E) A honeycomb structure of the reticulum beef tripe. (F) A 5 face 2D structure placed in one of the honeycomb beef tripe chamber. (G) A self-assembled cubic structure in the beef tripe chamber. (H-J) infrared images of the beef tripe and the sample during the self-assembly process. The surface temperature of the beef tripe remains at low temperature of around 10 ºC and the surface temperature of the sample increases from (H) 20 ºC to (J) 55 ºC during the self-assembly process.

4.7 Ladybug experiment

4.7.1 Ladybug experiment overview

To further illustrate the localized heat generation of the induction driven self-assembly, ladybug is used during the self-assembly process (figure 4.9). A live ladybug is placed next to the sample to be self-assembled (figure 4.9a-c).

4.7.2 Self-assembly with ladybug

During the assembly process, the sample is self-assembled while the ladybug next to it remains live and undisturbed (figure 4.9a-c). This indicating that the heat generation for the self-assembly is localized on the surface of the Ni panels and does not affect the ladybug.

4.7.3 Thermal analysis

The infrared images (figure 4.9d-f) show that the surface temperature of the ladybug remains the same while the sample temperature increases from 20 ºC to around 60 ºC during the assembly process. To quantify the heat effect of the induction driven self-assembly, the surface temperature of the sample and the ladybug is recorded and plotted shown in figure 4.9g and h. The surface temperature of the ladybug remains 20 ºC during the self-assembly process (figure 4.9g, black line). The surface temperature of the sample increases from 12 ºC to 54 ºC in 25 sec (figure 4.9g, red line). Figure 4.9h shows the surface temperature of the ladybug at different sample temperature. The straight line in figure 5h further indicates that heat generated by the Ni panels does not affect the ladybug.

4.7.4 Advantages

The ability of the induction driven self-assembly to penetrate through biomaterials and realize self-assembly in a confined bio-environment as well as the localized heat generation indicate that the induction driven self-assembly limits the damage of heat to

living tissues and organs, which is suitable for biomedical applications like drug delivery systems, cell capture, and cell encapsulation.

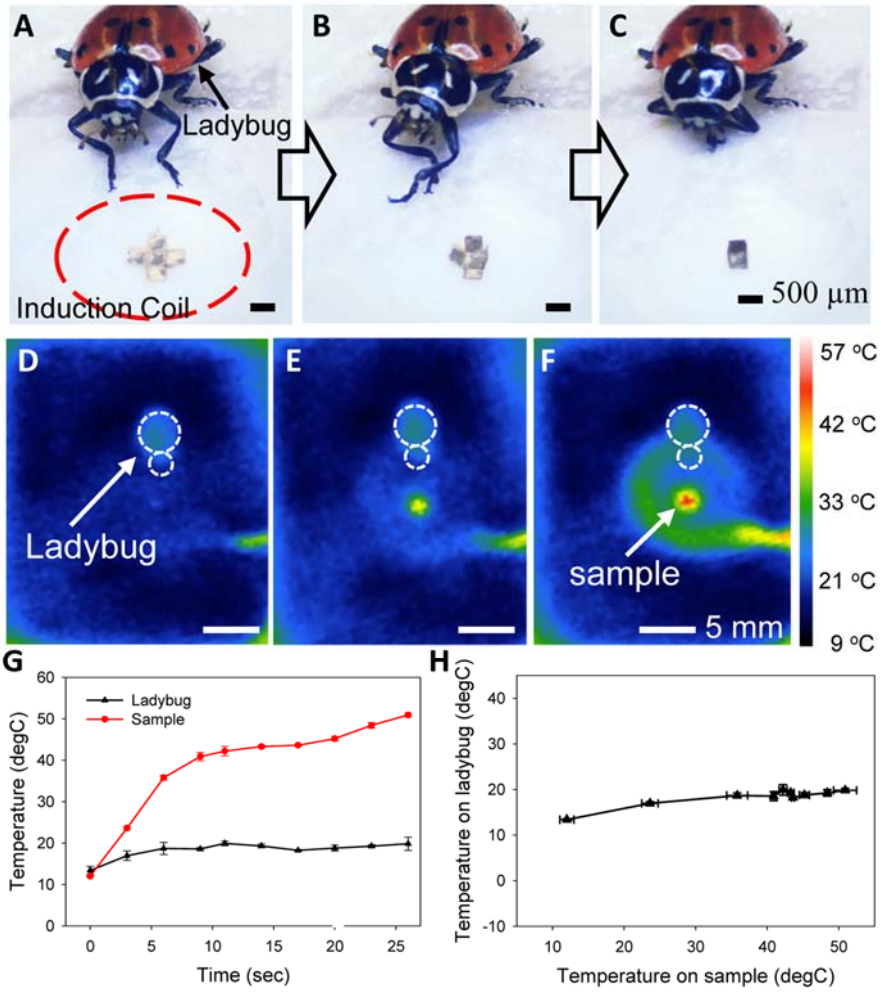

Figure 4.9 Ladybug experiment for the induction driven self-assembly. (A-C) Real-time optical image of the self-assembly process with a live ladybug placed close to the sample. The ladybug remains undisturbed during the self-assembly process (D-F) Infrared images of the ladybug and the sample during the self-assembly process. The surface temperature of the ladybug remains at around 20 ºC. The surface temperature of the sample increases

from (D) 20 ºC to (F) 55 ºC during the self-assembly process. (G) Surface temperature of the ladybug (black line) and the sample (red line) at different induction radiation time from 0 sec to 25 sec. (H) Surface temperature of the ladybug remains at 20 ºC at different sample temperatures.

Chapter 5

3D Metamaterial and Self-Assembly

5.1 Background of Metamaterial

5.1.1 Overview

Metamaterials (MMs) are artificial materials whose properties cannot be found in the natural world [202, 203]. They are usually engineered to contain arrays of metallic and dielectric components to exhibit negative permittivity and permeability [204-206]. Depends on the type of the MMs, they interact with different types of waves (electromagnetic wave, THz wave, light, sound). The structures of the MMs give them the ability to manipulate waves in such way that the waves can be bended, amplified, absorbed, or blocked. This unique ability makes the MMs ideal candidates for filters [207-209], modulators [210-212], amplifiers [213, 214], antenna [215, 216], sensors [217-225] and tunable devices [226, 227].

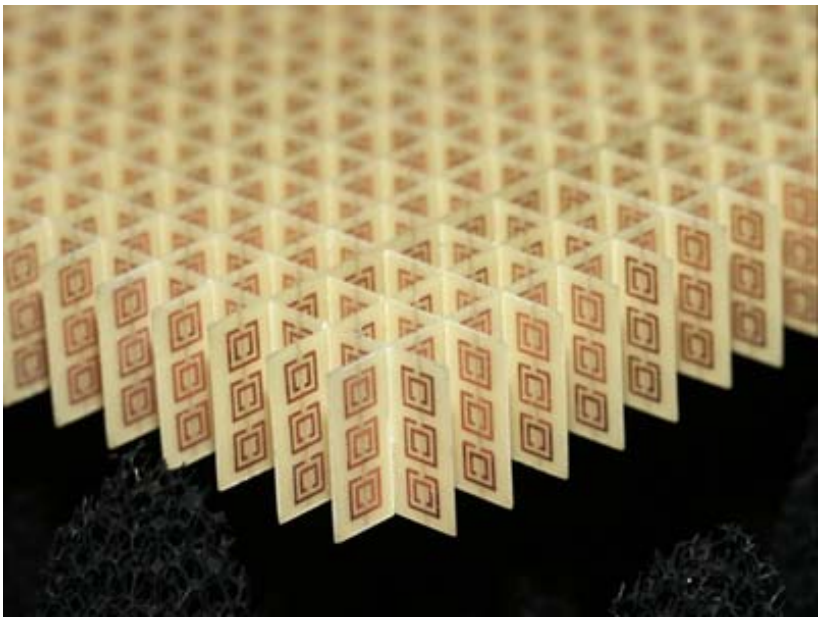

Figure 5.1 An example of a MM system consists of periodic metallic resonators and dielectric substrates. Each resonator/substrate component interacts with the electromagnetic wave and exhibits unique electromagnetic properties [228].

5.1.2 Types of metamaterials

MMs can be divided into different types depends on the frequency they are operating at and the purpose of the MMs: electromagnetic MMs, THz MMs, photonic MMs and tunable MMs. Electromagnetic MM is the most common and widely used MM [229]. Electromagnetic MM interacts with electromagnetic waves applied to the MM. Depends on the wavelength of the electromagnetic waves, electromagnetic MMs can be divided into THz MM (wavelength of micrometers) [230], microwave MM (wavelength of millimeters) [231-233], and photonic MM (wavelength of nanometers) [234-236]. When the electromagnetic wave is applied to the MM, the MM will resonate at certain

frequencies (resonant frequencies) and exhibit negative permittivity and negative permeability, which can be used for super lens [237-239] and electromagnetic cloaking [240-242].

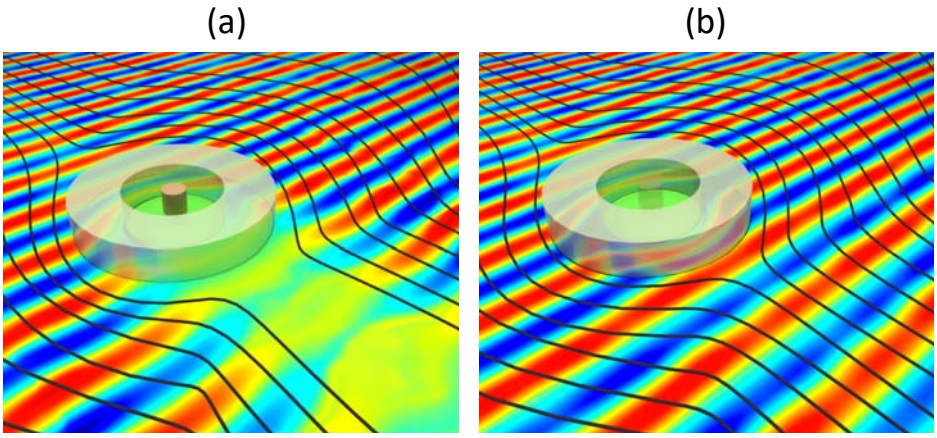

Figure 5.2 An example of electromagnetic cloaking using electromagnetic MMs.

THz MM is a particular electromagnetic MM that works with THz waves (with a wavelength between tens and thousands of micrometers). MMs working in THz regions have their advantages over other electromagnetic waves due to its small sizes (in micrometer scale). THz MM structures are compatible with micro-fabrication techniques and can be easily integrated into other devices. The dimension of the THz MM structures is also comparable to molecules, which is ideal for biomedical and chemical sensors. Photonic MM is a type of electromagnetic MM that interacts with optical waves (light). Photonic MM is especially useful for optical devices and has its applications in optical cloaking, super lens, and optical computing. Tunable MM refers to the types of MMs whose frequencies or resonant behaviors can be tuned based on the structural properties, material properties, and environmental properties of the MMs. Such tunable MMs can be used as MM tunable devices for filters, modulators, amplifiers, and antenna.

5.2 Split Ring Resonator (SRR) Metamaterials

5.2.1 Overview

One of the most common THz MM is split ring resonators (SRRs) [243, 244]. SRR is a 2D MM structure that contains a thin metallic ring with a narrow split to form a C shape (figure 5.3a) [245]. When the electromagnetic wave is applied to the SRR, it acts as a LC oscillation circuit with the capacitance inside the split and inductance along the ring. At resonant frequencies, the electromagnetic field penetrates through the split ring and induces current circulating inside the SRR. The time-dependent current charges and discharges the split and stores energy inside the SRR, which leads to resonant peaks (dips) at its transmission spectrum (figure 5.3b and c). Figure 5.3d-f shows optical images of a typical thin film SRR array with thousands of Gold (Au) C-shape SRR patterned on a Si substrate [245].

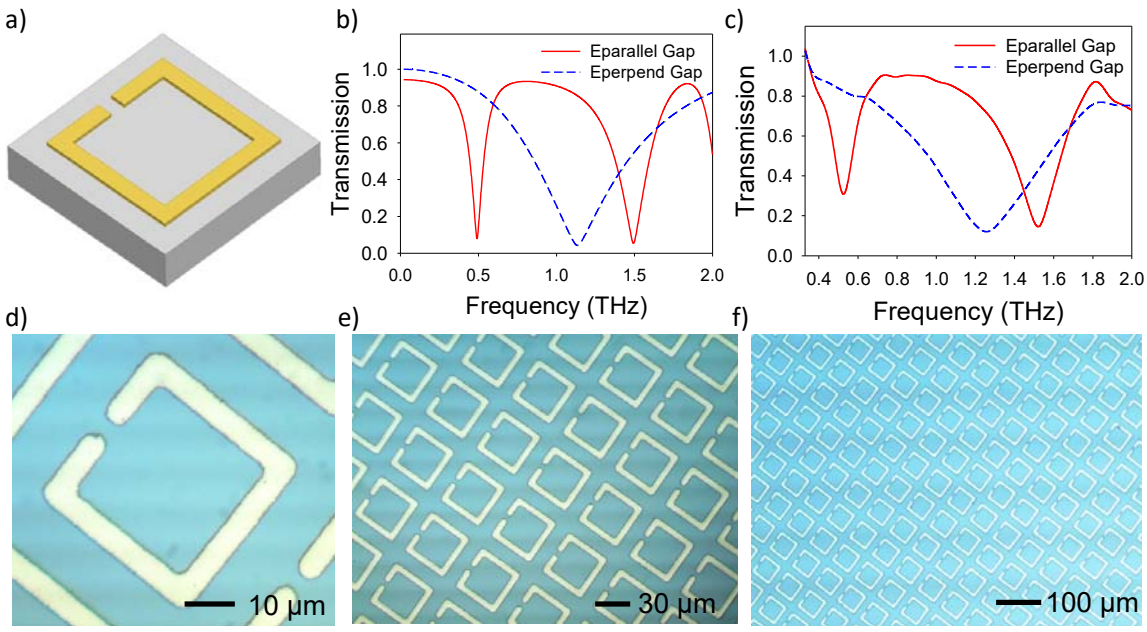

Figure 5.3 Traditional film-based SRRs [245]. (a) Schematic of film-based SRR. (b) Simulated transmission spectrum of film-based SRRs with three resonant modes. (c) Measured transmission spectrum of film-based SRRs with three resonant modes. (d-f) Images of film-based SRR array under an optical microscope. The dimension of film-based SRR is 36um*36um. The width of SRR arm is 4um and the split of the SRR is 4um. The film-based SRR is made of Au using electroplating process and the thickness of the deposited Au is around 300 nm.

5.2.2 Electric and magnetic responses

Depends on direction of the electromagnetic wave applied to the SRR, the electromagnetic responses of the SRR can be divided into electric responses and magnetic responses [246, 247]. Electric responses of the SRR refer to the situation where the electric field (*E*) of the incident wave is parallel to the split (figure 5.4a). The electric

field (*E*) couples with the split can generate current circulating the SRR. Magnetic responses of the SRR refer to the situation where the electric field (*E*) of the incident wave is perpendicular to the split (figure 5.4b). Since the SRR is symmetric to the electric field (*E*) in this case, the resonance is generated by the magnetic dipoles of the SRR. The electric and magnetic responses of the SRR can be reflected on the transmission spectrum. In figure 5.3b and c, the first resonant peak (first mode) and third resonant peak (third mode) of the SRR are electric responses (indicated in red color) while the second resonant peak (second mode) of the SRR is magnetic response (indicated in blue color).

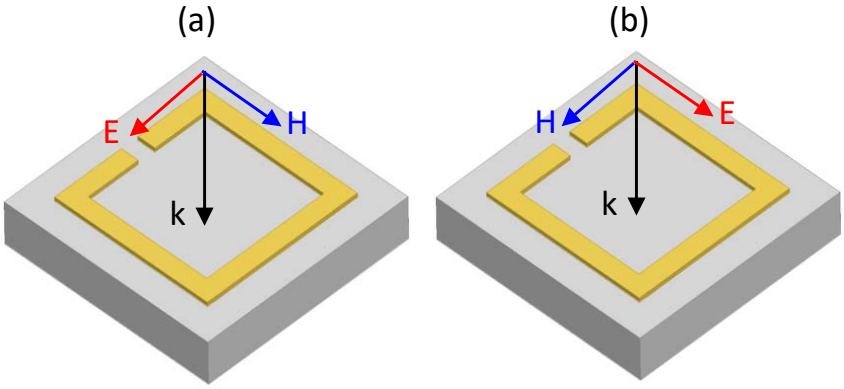

Figure 5.4 Electric and magnetic responses of SRR. (a) Electric response of the SRR with electric field (*E*) parallel to the split. (b) Magnetic response of the SRR with electric field (*E*) perpendicular to the split.

5.2.3 Quality factor of SRRs

To quantify the energy storage of the SRR and the sensitivity of the SRR to the electromagnetic waves, Q-factor is introduced. Q-factor is defined as the energy stored in the system over the energy dissipated per cycle [248, 249]:

$$Q \stackrel{\text{def}}{=} 2\pi \times \frac{energy\ stored}{energy\ dissipated\ per\ cycle} \quad (8)$$

Larger Q value means that more energy will be stored in the SRR and less energy will be dissipated into its surroundings, resulting in a sharper resonant peak in the transmission spectrum [250, 251]. The sharper resonant peak means that the resonant behaviors of the SRR are more sensitive to changes because small resonant frequency shifts can be easily distinguished and thus detected.

5.3 3D Metamaterials

5.3.1 Overview

3D MM refers to MM structures that are not limited to a 2D plane. Typical 3D MM can be created by patterning MM structures on a 3D object or stack multiple 3D MMs together to realize a 3D MM array [252]. Traditional 3D MM can be either fabricated using layer-by-layer technique, direct laser writing or projection lithography process. 3D MMs can be used for various applications like 3D sensors, 3D inclinometers and gyroscope, and 3D optical devices. By patterning SRRs with different configurations on each face of a cubic structure, unique isotropic and anisotropic properties of the 3D MMs can also be explored and utilized.

5.3.2 Drawbacks of 2D MMs

The simplest method to create a 3D MM is to pattern 2D SRRs and closed ring resonators (CRRs) on the faces of a 3D cubic structure (figure 5.5). Converting a 2D MM to 3D MM allows the 3D MM to exhibit unique 3D properties that the 2D MM does not have [225]. For example, the transmission responses of a MM depend on the rotation of the structure itself. When the 2D MM is rotating along X-, Y-, and Z-axis, the resonant frequencies and magnitudes of resonant peaks also changes, showing anisotropic behaviors. However, since the 2D MM structure is symmetric across the X-Y plane, the resonant responses complete overlap with each other at rotation angle ($n\pi+\theta$, n=1, 2, 3…), which indicates isotropic behaviors [225]. The uncertainty (isotropic or anisotropic) properties of the 2D SRR make it difficult to be used as 3D sensors and other 3D applications.

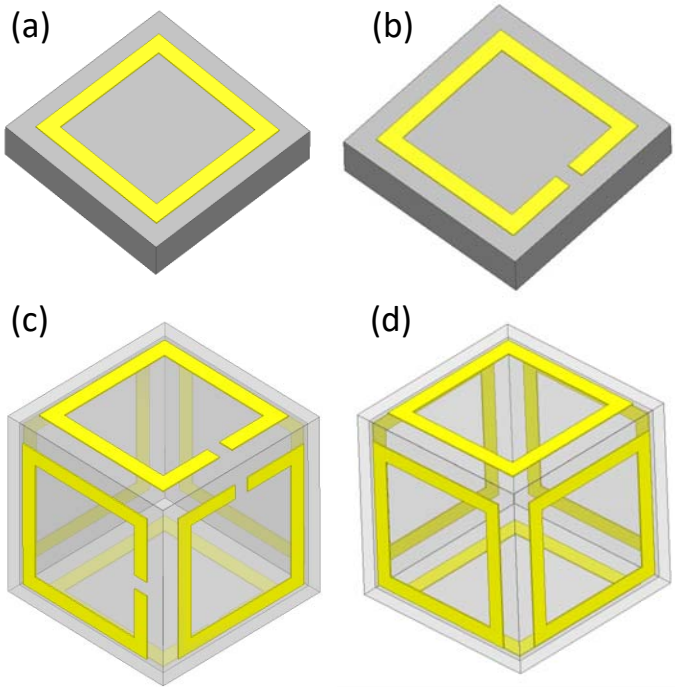

Figure 5.5 Comparison between 2D MMs and 3D MMs.

5.3.3 3D asymmetric metamaterial

To solve above problems of the 2D MMs, novel 3D asymmetric MMs are developed [225]. SRR structures with different sizes and directions are patterned on the 3D cubic surfaces to realize an asymmetric MM (figure 5.6). Since all the SRRs on each face of the cube are tilted, the 0 degree and 180 degree symmetry is broken, results in complete anisotropic behaviors of the 3D MM. Since the tilted SRRs on each face of the cubic structure have different sizes, the resonant frequencies of each SRR are also different. Each rotation of the 3D MM corresponds to a set of resonance amplitudes of L_1, L_2 and L_3. The rotation angles of the 3D MM can be easily determined by checking the resonance amplitudes of each peak. The anisotropic behaviors of the 3D MM make it ideal candidates for 3D inclinometers and gyroscopes to detect rotation angles and tilts.

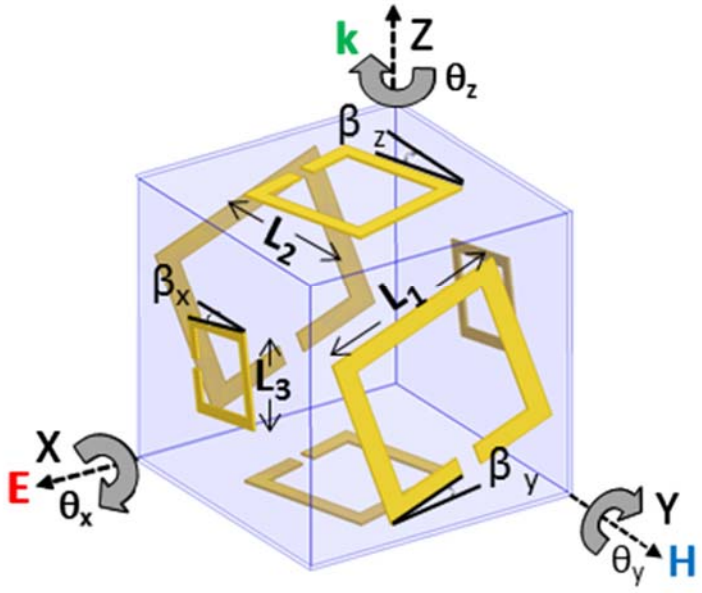

Figure 5.6 3D asymmetric cubic SRR MM [225].

5.4 Self-assembled 3D Metamaterials

5.4.1 Overview

In order to fabricate such complex 3D SRR structure, self-assembly technique is used [225]. Using self-assembly allows the build of complex 3D structures from 2D components (SRRs, panels, and hinges). Since the fabrication of the 2D components is a traditional bottom-to-up micro-fabrication process, it is easier to make all the structures in 2D and then transform the 2D structures into 3D structures using self-assembly technique.

5.4.2 Fabrication strategies

The detailed process is shown in figure 5.7 [225]. The 2D structure was first fabricated on a silicon substrate with a 10 nm Cr and 300 nm Cu layer deposited on top. The Cu layer is used as a sacrificial layer for releasing the structure from the substrate and an electroplating seed layer for Au SRR patterning. First, the 300 nm thick Au SRR patterns were fabricated using photolithography and Au electroplating process. Then 10 μm SU-8 2010 (MicroChem) panels and 21 μm SPR-220 7.0 (MEGAPOSIT) hinges were patterned sequentially on top of the Au SRRs (figure 5.7a). For the SU-8 2010 panel patterning, a spin coating of SU-8 2010 at 1000 rpm was used. The SU-8 was then pre-baked at a temperature of 95 ºC for 2.5 min and exposed to UV light (365 nm) for 15 sec. A post exposure bake was then followed using 95 ºC for 3.5 min. The exposed SU-8 2010 was then developed using SU-8 developer for 2 min and rinsed thoroughly with DI water. For the SPR-220 7.0 hinges, The SPR-220 7.0 resist was spin-coated with a speed of 1000

rpm followed by another spin-coating of 1000 rpm to achieve a 21 μm thickness that we need. The SPR-220 7.0 was then baked at 60 ºC for 30 sec, 115 ºC for 90 sec and then 60 ºC for 30 sec. The sample was left undisturbed for 3 hours before an exposure of UV light for 100 sec. The purpose of the 3 hours waiting is to allow the SPR-220 7.0 to absorb water from the atmosphere to prevent cracking. The exposed SPR-220 7.0 was developed with AZ developer to achieve the final hinge patterns. Upon self-assembly, the Cu sacrificial layer was etched away using Cu etchant and the structures were transferred to a water environment. Heat was applied to the water using a hotplate and melted the SPR-220 hinges to trigger the self-assembly process (figure 5.7b-c). Optical images (figure 5.7d) show the Au SRRs, 2D structure arrays and a 2D single structure contains Au SRRs, SU-8 panels and SPR-220 hinges. A fully self-assembled 3D cubic structure is shown in figure 5.8 [225].

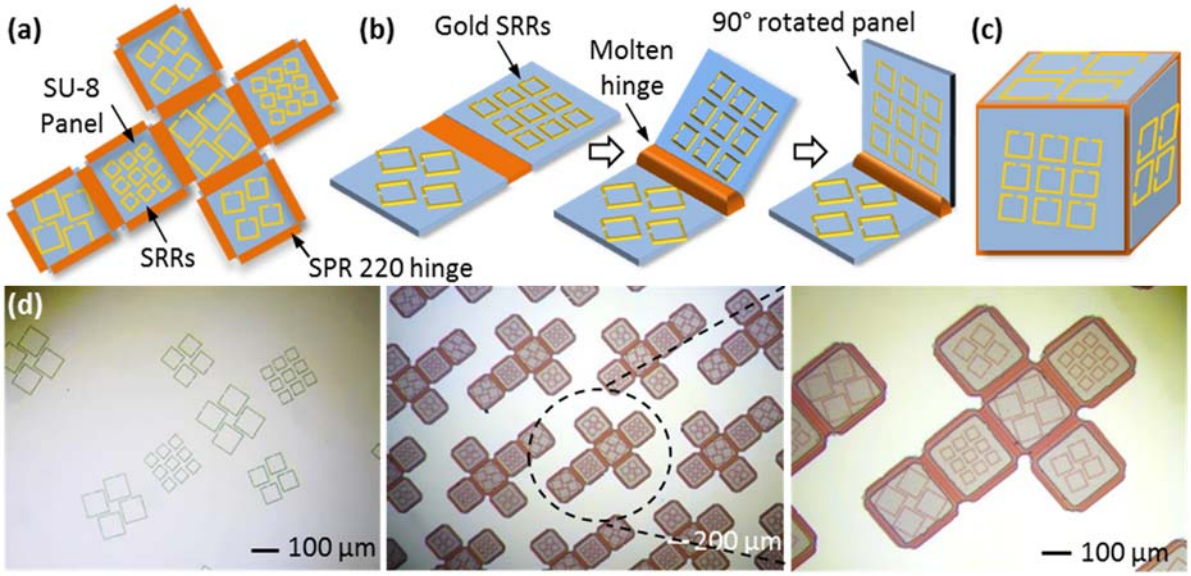

Figure 5.7 Fabrication process of 3D asymmetric SRR MM [225].

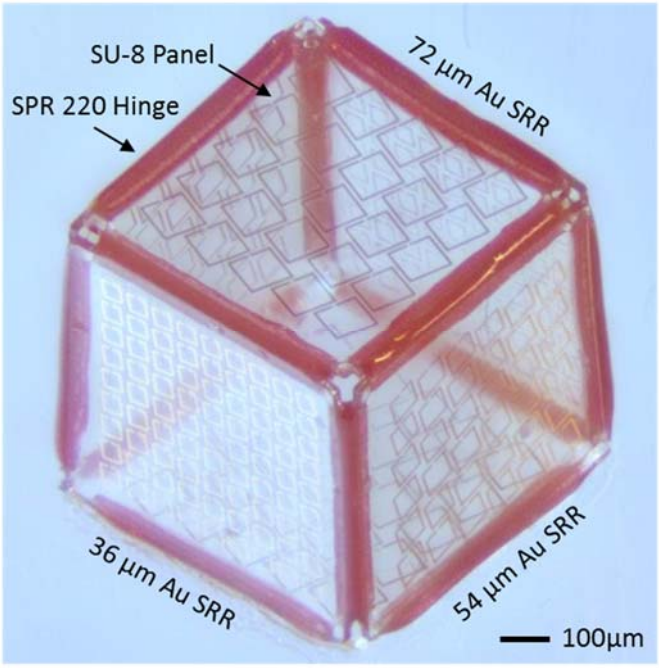

Figure 5.8 Self-assembled 3D asymmetric MM structure [225].

5.4.3 3D isotropic metamaterials

Combining self-assembly and THz SRR to create 3D MM structures is essential since it generates unique properties that cannot be seen in 2D MM devices. By configuring the shape of the resonators on the cubic structures, 3D fully isotropic MM structure can also be created [224]. Figure 5.9 shows a design of 3D X-shape MM structure. Different from traditional 3D MM that contains 2D resonators on each face of the cubic structure (figure 5.9a), resonators with a X shape design is patterned in a way that the entire 3D structure forms 3 Au resonator loops (Octagram) with splits at each corner of the cubic structure (figure 5.9b). Since each split is equally positioned at the corners of the cubes in all directions, the 3D X-shape MM is fully isotropic in all directions (figure 5.9c).

Achieving fully isotropic behaviors of the 3D MM is essential for designing 3D sensors because the position and tilt of the 3D MM structure is not always fix. If the 3D MM resonant behavior is fully isotropic, the position and tilt of the 3D structure will not affect the sensing process. Utilizing the isotropic and anisotropic behaviors of the 3D MM, we can create devices like 3D sensors, 3D inclinometers, and 3D isotropic devices.

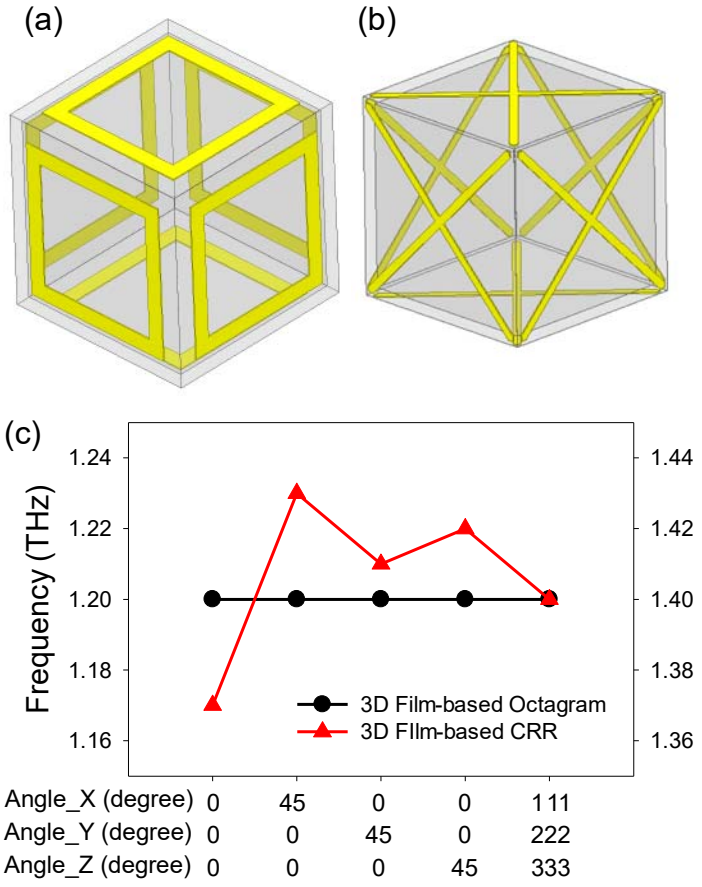

Figure 5.9 3D X-shape MM shows fully isotropic behaviors. (a) A traditional 3D CRR MM (b) A novel 3D Octagram MM with X-shape resonators on each face of the cubic structure (c) The resonant frequency comparison between 3D CRR MM and 3D Octagram MM at different rotation angles.

The fabrication process of the 3D X-shape MM is similar to the fabrication of 3D asymmetric MM [224, 225]. The details are shown in figure 5.10. 300 nm thick Au X-shape resonators were first patterned on a Cu/Cr/Si substrate using Au electroplating method. The Cu sacrificial layer and the Cr adhesion layer on top of the silicon substrate were 300 nm thick and 10 nm thick respectively. 10 µm thick SU-8 2010 panels and 21 µm thick SPR-220 7.0 hinges were then patterned on top of the Au resonators using photolithography process. Detailed process of the SU-8 2010 and SPR-220 7.0 patterning can be found in chapter 5.4.2. The entire structure (Au resonators, SU-8 2010 panels, and SPR-220 7.0 hinges) was released from the substrate by etching the Cu sacrificial layer using Cu etchant. The structure was then transferred from Cu etchant to DI water multiple times to fully remove the Cu etchant. A petri dish containing DI water and the fabricated 2D structure was then placed on a hot plate. The temperature of the hot plate was increased from 60 ºC to 200 ºC until the DI water started to boil. The heat melted the SPR-220 hinges and triggered the self-assembly process. The Au X-shape resonators, SU-8 panels, SPR-220 hinges, and a completed assembled 3D cubic structure are shown in the optical images in figure 5.10.

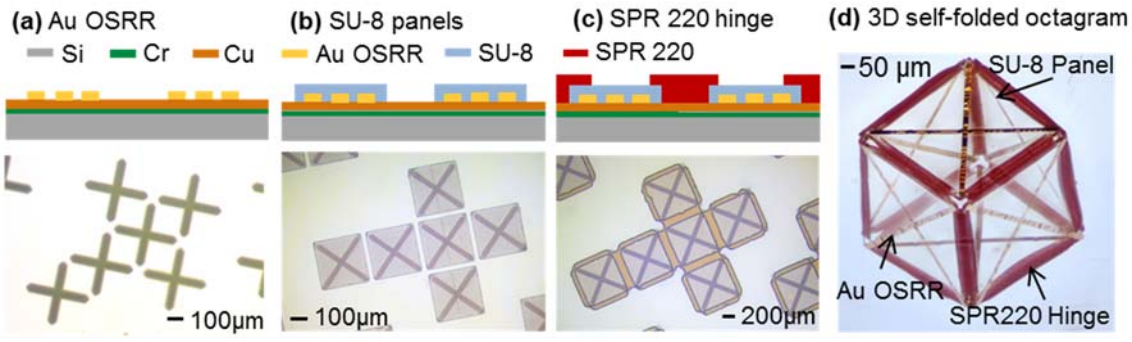

Figure 5.10 Fabrication of 3D X-shape MM [224].

Chapter 6

Advanced THz Metamaterial

6.1 Drawbacks of existing metamaterials

6.1.1 Sensitivity

THz MMs are good candidates for the sensing and detecting chemicals and biomaterials [253-257], temperature [258], strain [259], alignment and position [260]. THz MMs can also be used as frequency agile devices by tuning the resonant frequency from permittivity changes of its surroundings [261]. The sensitivity and selectivity of the THz MMs largely depends on their Q-factors that define the sharpness of the resonant peaks, which results in the detection of minute amount of substance changes. Even though THz MMs show great potentials for sensing and frequency-agile applications due to their dimensions comparable to chemicals and various biomedical substances, the Q-factor of the currently developed THz MMs is relatively (normally below 10 [261, 262]) compared to mechanical resonators (typically between 10^4 and 10^7), which limits their sensitivities [263].

One of the approaches to improve the Q-factors of the THz MM is to reduce energy losses of the MMs to the environment by optimizing the material and structural properties of the MM [264]. Common energy loss mechanisms of the MMs include: Ohmic loss of the conductors inside the MMs [265], dielectric loss from the substrate [266], and radiation loss of the MMs [267]. One method to reduce the energy loss of the MMs is to

break the symmetry of the MMs by introducing asymmetric split resonators (ASRs) [268, 269]. The asymmetric design of the MMs can reduces radiation losses and enhances the Q-factor of the MMs up to 30 [270-273]. A similar method of improving Q-factor is to introduce multiple modes (odd mode and even mode) in the MMs to form a multiple modes coupling super unit [274]. This method can increases the Q-factor by a factor of 5 compared to traditional THz MMs. However, to realize highly sensitive THz MM devices, the Q-factor of the THz MMs needs to be further enhanced (10 times and more).

6.1.2 Frequency shift

In addition to the Q-factor of the MMs that largely affects the sensitivity of the MMs, frequency shift is another factor to measure how sensitive the MM sensor is. Common method to characterize the frequency shift of a MM is to analyze the resonant frequency of the peak changes in the THz transmission spectrum when substances with different permittivities are applied to the MM. Highly sensitive MM sensors requires the MM structure to be able to detect minute permittivity changes (even single molecules [275-278]) of the substance with a large frequency shift. However, this is extremely difficult to be realized with traditional film-based MM because the resonant peaks of the film-based MMs are relatively broad, which makes the detection of small amounts of substances impossible, especially when the volume or concentration of the substance around the MMs is not high enough.

6.1.3 Selectivity

Selectivity is another factor that evaluates the performance of the THz MM devices. Selectivity measures the ability of the MM sensors to detect multiple substances [279]. In order for the MM to detect multiple substances, surface modifications of the MM structures are required to enable the special binding between each substance and the MM surface. Since the surface areas of the film-based THz MMs are relatively small and most of the signals of the THz MMs are focused on the split, the selectivity of the film-based THz MMs is very low. This prohibits the THz MMs from having the ability to precisely detect molecules and chemical substances.

6.2 Nanopillar-based SRR metamaterials

6.2.1 Design of nanopillar-based SRRs

In order to improve the sensitivity and selectivity of the MMs, the Q-factor of the MMs need to be enhanced. As mentioned in previous chapters, common methods of improving Q-factors of the MM include breaking the symmetry of the MM structures and exciting both odd and even modes of the MM [270-274]. However, the Q-factor can be improved a few times using such methods, which does not meet the requirement of ultra-high sensitive MMs. To address the issues of current high Q MMs, a novel nanopillar-based THz SRR MMs is introduced, which uses displacement currents to flow between the metallic nanopillars and increases the energy storage inside the dielectric nano gaps between the nanopillars. The enhanced energy storage in the nanopillar-based MM leads

to a high Q-factor of up to 450 (more than 30 times higher than the Q-factor of a traditional film-based MM) [245]. The nanopillar-based MM consists of nanopillar arrays that form a C-shape SRR. The nano gaps (a few nanometers to a few tens of nanometers) between the Au nanopillars are made of vacuum or dielectric materials with various permittivities. Due to the large surface areas of the nanopillars compared to a continuous metal thin film, the nanopillar-based MM offers an increase of the overall charge separations ($+q$ and $-q$) on the nanopillar surfaces, which results in the increase of the total energy storage in the nano gaps. The enhancement of the total energy storage in the nanopillar-based MM provides a high Q-factor compared to film-based MM that only have energy storage inside the single split of the SRR. In addition, by introducing dielectric materials in the SRR, the Ohmic loss of the entire structure also reduces, which further improves the Q-factor. Thus a high Q-factor of about 450 can be achieved for the nanopillar-based MM, which is ideal for high sensitive MM devices.

6.2.2 Electromagnetic induced displacement current

Resonance in the nanopillar-based SRR MMs is driven by displacement current, which is typically defined as the integral of electric flux between two conductors due to time-varying electric fields. Displacement current is not real electric current that is essentially moving charges in a conductor but it shares similar properties and characteristics as an actual current and is originated from the time-varying electromagnetic field around it. A typical example to explain the displacement current is a capacitor with two parallel conducting plates (figure 6.1a) [280]. The charges are separated by the

dielectric gap between the two plates and are accumulated on each side of the plate (+q and -q). The charge difference between the two plates creates an electric field with a direction from the positive charge (+q) to the negative charge (-q), which induces a current, namely displacement current across the gap between the two plates. The density of the displacement current (J_d) can be defined as the time derivative of the electric field displacement (D) across the plates: $J_d = \partial D/\partial t$. Same concept can be applied to the nanopillars (figure 6.1b). When the electromagnetic field is applied to the Au nanopillar arrays, electric field can be generated inside the nano gaps between the nanopillars and induces displacement current inside the nano gaps. The displacement current in the nano gaps and the electric current in the Au nanopillars form a complete current looping along C-shaped nanopillar-based SRR MMs. Different nanopillar shapes (e.g., circle, hexagon, and square) can be considered to create nanopillar-based MM (figure 6.1c). To illustrate the possibility of fabricating the nanopillar-based MM, circular nanopillar-based MM were fabricated shown in figure 6.1d. Each SRR is formed by thousands of platinum nanopillars fabricated using an anodic aluminum oxide template on a Si substrate [281-283]. The potential problem with circular shaped nanopillars is that the distance between the two adjacent nanopillars (the nano gap size) is not uniform along the edges of the circular nanopillars, which makes the displacement current too weak to pass through the nano gaps. Thus, rectangular nanopillars (figure 6.1e) were chosen to replace the circular nanopillars to demonstrate resonant behaviors induced by displacement current in SRRs.

6.2.3 Geometric configurations and parameters

The square nanopillars with nanoscale gaps are patterned on a Si substrate to form a C-shaped SRR [245]. When the THz electromagnetic field penetrates through the nanopillar-based SRR (normal incident with the electric field (*E*) parallel with one arm of the SRR, figure 6.1e), it generates loops of current (displacement current and electric current) circuiting inside the SRR (figure 6.1b). The current oscillating inside the SRR stores energy in the nano gaps and creates resonant behaviors of the SRR (figure 6.1f). Therefore, the nanopillar-based SRR can be seen as an inductive-capacitive (LC) circuit, which has resonant responses to the incident electromagnetic wave. The displacement current (I_d) generated inside the nano gaps between two Au nanopillars can be defined by the following equation [284],

$$I_d = -J_d \cdot A = -\frac{\partial D}{\partial t} \cdot A = -\frac{\omega \varepsilon A}{d} \cdot V_0 \sin \omega t \quad (9)$$

Where J_d is the displacement current density, ω is the angular resonant frequency, ε is the permittivity of the space between the two conductors, d is the distance between the two nanopillars, V_0 is the magnitude of voltage between the two nanopillars, and t is time. Lastly, A is the area of the nanopillar facing against each other; both the width (l) and the height (H) of the nanopillar affect this parameter (figure 6.1e).

6.2.4 Resonant behaviors

To prove that the nanopillar-based MMs are driven by displacement current and have the similar resonant behaviors as the traditional film-based MMs, nanopillar-based SRRs were designed and simulated. The transmission spectrum of the nanopillar-based SRRs is shown in figure 6.1f using ANSYS HFSS (High Frequency Structural Simulator,

version: 13.0.2) commercial software [245]. Three different resonant modes (ω_1: 1st, ω_2: 2nd and ω_3: 3rd) can be clearly seen based on the surface current distributions of the nanopillar-based MMs, which are the same surface current distributions as the current distributions of the traditional film-based SRRs. This indicates that the nanopillar-based SRRs work the same way as the film-based SRRs.

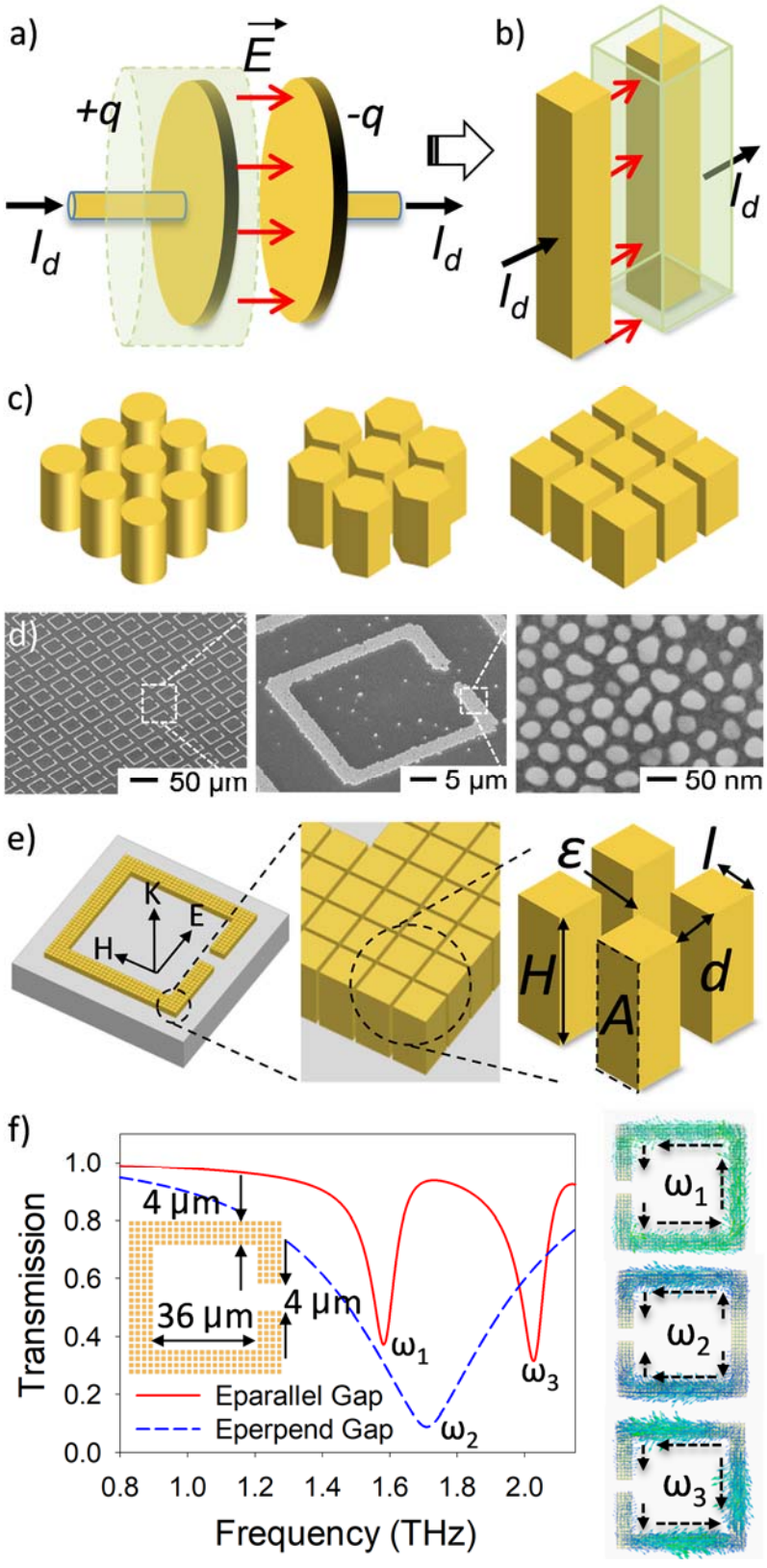
a)
b)
c)
d)
e)
f)
+q
-q
$\vec{E}$
I_d
50 μm
5 μm
50 nm
K
E
H
ε
l
H
A
d
4 μm
36 μm
4 μm
Transmission
Frequency (THz)
Eparallel Gap
Eperpend Gap
ω1
ω2
ω3

Figure 6.1 Illustration and SEM images of nanopillar-based MMs utilizing displacement current [245]. (a) Displacement current (I_d) induced between two conducting plates with time-dependent electric field (E) generated by separated charges ($+q$ and $-q$). (b) Displacement current (I_d) induced between two metallic nanopillars. This displacement current is derived from the same concept as displacement current between two plates. (c) Nanopillar arrays with different configurations (circle, hexagon and square). (d) SEM images of circular nanopillar-based SRR array. Each SRR is formed by thousands of Au nanopillars fabricated using an anodic aluminum oxide template. (e) Schematic of square-nanopillar-based SRR. The geometry and a material property are defined by the height (H), width (l), interface area (A), nano-gap size (d) and permittivity (ε). (f) Simulated transmission spectra of a nanopillar-based SRR (with split size of 4 um, SRR length of 36 um, and SRR arm width of 4 um) and the surface current distributions at the first three resonant frequencies. First mode (ω_1) and third mode (ω_3) of the SRR are for the electric field parallel to the split, while second mode (ω_2) is for the electric field perpendicular to the split.

6.3 Transmission and frequency responses

To further exam nanopillar-based SRRs, the effect of the geometric parameters of the nanopillar-based SRR on the resonant behaviors was analyzed using the HFSS simulator [245]. The nanopillar-based SRR was simulated with different nano gap sizes (d = 25 nm, 30 nm, and 35 nm) while the thickness of the nanopillars (H) and the permittivity

(ε) of the nano gaps were fixed (H = 500 nm, and ε = 9.8 (Al_2O_3)). It is expected that the amplitude of the resonant peak increases with the decrease of the nano gap size (d) due to the increase of the displacement current (I_d) in equation 9. This trend can be seen in the simulation results in figure 6.2a. As can also be seen in figure 6.2a, the resonant frequency (f) of the nanopillar-based SRR increases with the increase of the nano gap size (d), which can be explained by the fact that the increase of the nano gap size (d) results in the decrease of the total capacitance ($C = \varepsilon \cdot A/d$) of the SRR, leading to the increase of the resonant frequency ($f \sim 1/\sqrt{C}$). The nanopillar-based SRRs with different Au nanopillar thicknesses (H = 300 nm, 500 nm, and 700 nm) were also tested with a fixed nano gap size (d) of 25 nm and a nano gap permittivity (ε) of 9.8 (figure 6.2b). In figure 6.2b, as the Au nanopillar thickness (H) decreases, the transmission amplitude of the nanopillar-based SRR decreases and the resonant frequency increases. The changes of the nanopillar thickness (H) will affect the area (A) facing between two nanopillars, resulting in the changes in displacement current (I_d) based on equation 9 and the changes in the total capacitance of the SRR. When the size of the nano gap increases to a limit (critical gap d_c), the displacement current becomes too weak to pass through the nano gaps and the resonant behaviors disappears, as shown in figure 6.2c and d. The critical gap size (d_c) of the nanopillar-based SRR also depends on the permittivity (ε) of the nano gap (figure 6.2c) and the thickness (d) of the nanopillar (figure 6.2d). This can be explained using equation 9: the increase of the permittivity (ε) of the nano gaps and the increase of the nanopillar height (H) lead to the enhancement of the displacement current (I_d). Thus the nanopillar-based SRR with larger permittivity of the nano gap and thicker Au nanopillars will have a larger critical gap size compared to the rest of the SRRs (figure 6.2c and d). Simulation

results shown in figure 6.2 also indicate methods to adjust the resonance and resonant frequencies of the nanopillar-based SRRs to achieve desired resonant frequencies and strong resonant behaviors.

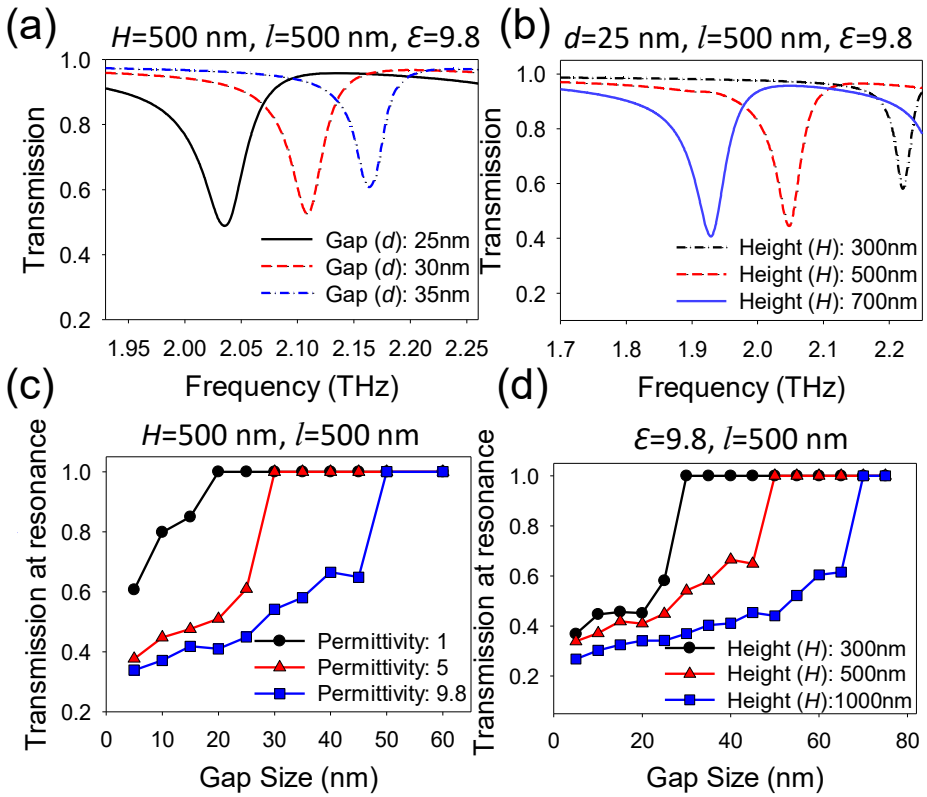

Figure 6.2 Transmission properties of nanopillar-based SRRs with varied parameters [245]. First modes (ω_1) of nanopillar-based SRRs in transmission spectra were obtained by simulation. Influences of (a) nano gap size of SRRs and (b) height of SRRs on transmission amplitude. Transmission amplitude of nanopillar-based SRRs with varied nano-gap size, (c) permittivity, and (d) height.

6.4 Quality factor analysis

To analyze the Q-factor of the nanopillar-based SRRs, the nanopillar-based SRRs with different parameters were simulated using HFSS simulator and the Q-factors for each simulation were calculated and plotted with first mode (ω_1) and third mode (ω_3) (figure 6.3). In figure 6.3, the thickness of the nanopillar (H) (figure 6.3a), the width (l) of the nanopillar (figure 6.3b), the permittivity (ε) of the nano gap (figure 6.3c), and the size of the nano gap (d) all largely affect the Q-factor of the nanopillar-based SRRs. Firstly, the Q-factor increases with the increase of the nano gap sizes (d, d = 0 indicates film-based SRR). This is because the energy storage inside the nanopillar-based SRR can be defined as $U = q^2/2C$, where q is the electric charges inside the capacitor and $C = \varepsilon \cdot A/d$ is the capacitance of the capacitor. The energy storage in the SRR (U) increases with a decrease of the capacitor (C) and thus an increase of the nano gap size (d). Both thickness (H) and width (l) of nanopillars affect the area (A) of the nanopillars facing each other. An increase of the thickness (H) or the width (l) of the nanopillar will result in the increase of the interface area (A), leading to an increase of the capacitance (C) of the SRR. The increase of the capacitance (C) leads to the decrease of the energy storage (U), thus a decrease of the Q-factor (figure 6.3a and b). Similarly, an increase of the permittivity (ε) of the nano gaps also leads to the increase of the capacitance (C) of the SRR, which results in the decrease of the energy storage (U) and the Q-factor of the nanopillar-based SRRs (figure 6.3c). Since the usage of the nanopillars and the nano gaps between them, the energy storage of the nanopillar-based SRRs improves dramatically, which results in a high Q-factor of more than 300 for the 1st mode and more than 450 for the 2nd mode (figure 6.3b),

which is 33 and 32 times higher than that of thin-film-based typical SRRs (d = 0, Q-factors of 9 and 14 at 1st and 3rd mode, respectively). The Q-factor enhancement with nanopillar-based SRRs is much higher compared to the Q-factor achieved by breaking the symmetry of the SRR structures and by introducing coupling between SRR units. In addition, the nano-scale gaps created by the Au nanopillar arrays are suitable for biomedical application and biochemical sensing applications due to the size of the nano gaps comparable to the biomolecules and the chemicals.

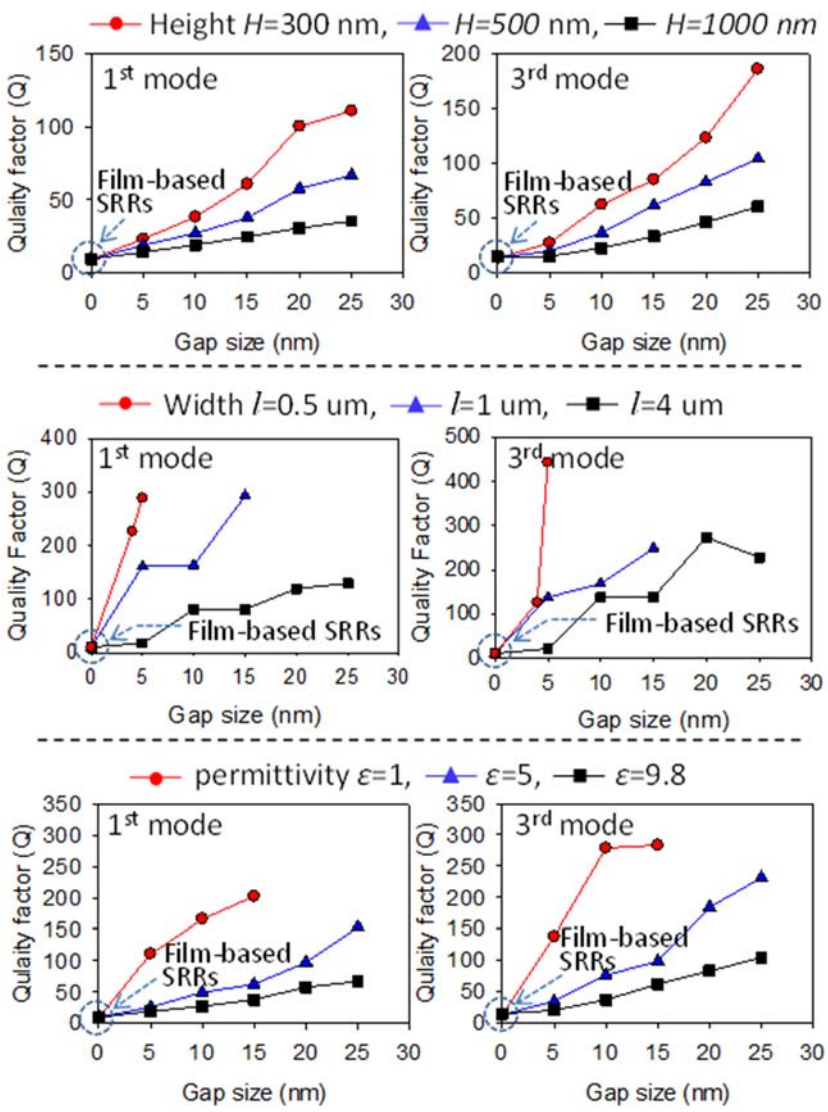

Figure 6.3 Q-factor characterization of nanopillar-based SRRs with varied parameters [245]. The Q-factors of thin-film-based SRRs (nano-gap size = 0 nm) are also presented in the figures. The nano-gap size varies from 5 nm to 25 nm for each simulation and Q-factor of both first mode (ω_1) and third mode (ω_3) of nanopillar-based SRRs are shown. The dependence of Q-factor of nanopillar-based SRRs on (a) the height of nanopillars, (b) permittivity of the nano-gaps and (c) the width of nanopillars. A maximum Q-factor of nanopillar-based SRRs of more than 450 is observed which is more than 32 times higher than that of thin-film-based SRRs.

6.5 Film- and nanopillar-based SRRs Comparisons

Another important factor that affects the sensitivity of nanopillar-based SRRs is frequency shift [245]. A large frequency shift under different permittivity (ε) of the substance means that the nanopillar-based SRR can be used to detect the substance with minute amount of substance presented. Because of the large surface areas of the nanopillar arrays compared to the thin film SRR, a large frequency shift can be introduced, which makes the nanopillar-based SRR more sensitive to the substance changes around the SRR (figure 6.4). The effective sensing area of the traditional film-based SRR is only focused at the split of the SRR, which is relatively small compared to the entire dimension of the SRR. On the other hand, the effective sensing area of the nanopillar-based SRR is distributed to each nano gaps between the nanopillars, which significantly enhances the frequency shifts and the sensitivity. In addition, the surface area of the nanopillars can be further improved by changing the geometric parameters of the nanopillar-based SRRs (H, and l). A surface area of 2500 time larger than the film-based SRR can be easily achieved by tuning the parameters of the SRR. The frequency shifts of the nanopillar-based SRR and film-based SRR with a fixed height (H = 500 nm), width (l = 500 nm), and gap size (d = 10 nm) are shown in figure 6.4a. It can be observed that as the permittivity of the nano gaps increases from 1 to 9.8, the resonant frequency shifts to the left. The resonant frequency shift for the film-based SRRs is only around 0.3 THz. However the frequency shifts of the nanopillar-based SRR is 3 THz, which is 10 times larger than the frequency

shift of the film-based SRR. To quantitatively compare the frequency shift between the nanopillar-based SRR and the film-based SRR, the frequency shifts of both the nanopillar- and the film-based SRR at each permittivity change intervals were plotted in figure 6.4b. The largest frequency shifts difference between the nanopillar-based SRR and the film-based SRR occurs at the permittivity interval of 2.5 to 5 with a frequency shift difference of 17 time (0.34 THz for the nanopillar-based SRR and 0.02 THz for the film-based SRR, figure 6.4b). The large frequency shift of the nanopillar-based SRR shows the high sensitivity of the nanopillar-based SRR to the permittivity changes of the substance around it, which allows the SRR to be able to detect minute substances. In addition, the large frequency shift makes the nanopillar-based SRR ideal candidate for frequency-agile devices.

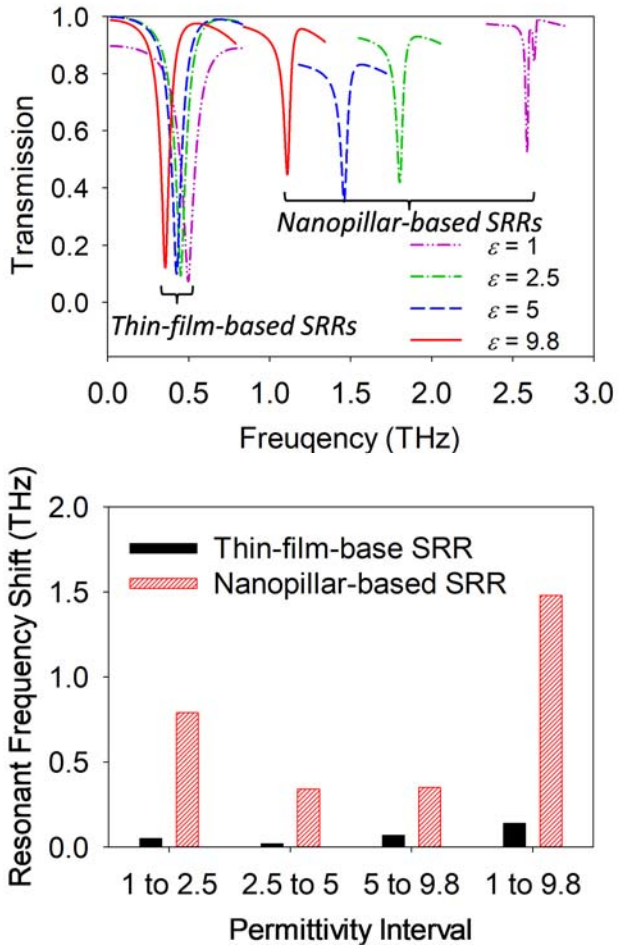

Figure 6.4 Characterization of resonant frequency shifts using simulation [245]. (a) Resonant frequency (ω_1) shifts of nanopillar-based SRRs and film-based SRRs on transmission spectrum with varied permittivities (ε = 1, 2.5, 5 and 9.8). (b) Quantitative comparison (histogram) of the resonant frequency shift between nanopillar-based SRRs (red bars) and film-based SRRs (black bars) with 4 different permittivity intervals.

6.6 Fabrication process and measurements

6.6.1 Fabrication process

In order to experimentally demonstrate the resonant behaviors of the nanopillar-based SRRs, the slit-based SRRs were fabricated (figure 6.5) [245]. The slit-based SRRs consist of Au slits with 10 nm thick Al_2O_3/air nano gap between them. The slit-based SRR and the nanopillar-based SRR shares the same concept: using nano gaps to enhance the energy storage of the SRR and increases the Q-factor. Both of them uses displacement current to conduct current and form loops of current inside the SRR. The schematic of the slit-based SRR is shown in figure 6.5a-d. The two adjacent Au slits were built by a sequential Au electroplating process with a Al_2O_3 atomic layer deposition (ALD) process between them to achieve a 10 nm Al_2O_3 gap between the two Au slits. Figure 6.5a shows the first layer of the Au slit with a thickness of 400 nm on a high-resistive (560 – 840 Ω·cm) Si substrate. Figure 6.5b shows the 100 layer (around 10 nm) of ALD Al_2O_3 layer after the 1st Au electroplating and the 2nd Au electroplating of 300 nm thick Au slits. The second layer of Au completely filled the gaps between the first Au slits and defines the nano gap of ALD Al_2O_3, which results in closely packed Au-Al_2O_3-Au sandwich structures (figure 6.5c and d). Since the ALD system allows for the control of the Al_2O_3 thicknesses of 0.1 nm (1 layer of the ALD cycle) and the ALD layer is uniform though the entire sample, it is easy to realize nanometer-scale gaps between the Au slits with a high aspect-ratio (figure 6.5e and f). Lastly, the C-shape SRR can be patterned using a lithography process and the excessive Au slits and Al2O3 gaps were etched away outside the C-shape using ion-milling process (figure 6.5g and h). If the air nano gap is preferred,

the Al_2O_3 gap can be removed by putting the sample in a HF solution. Figure 6.5e-h shows the scanning electron microscope (SEM) images of the fabricated slit-based SRR array as well as the 10 nm Al_2O_3 gap between the Au slits defined on the Si substrate. A 5 nm Al_2O_3 gap can also be realized (figure 6.6). A detailed fabrication process is shown in figure 6.6.

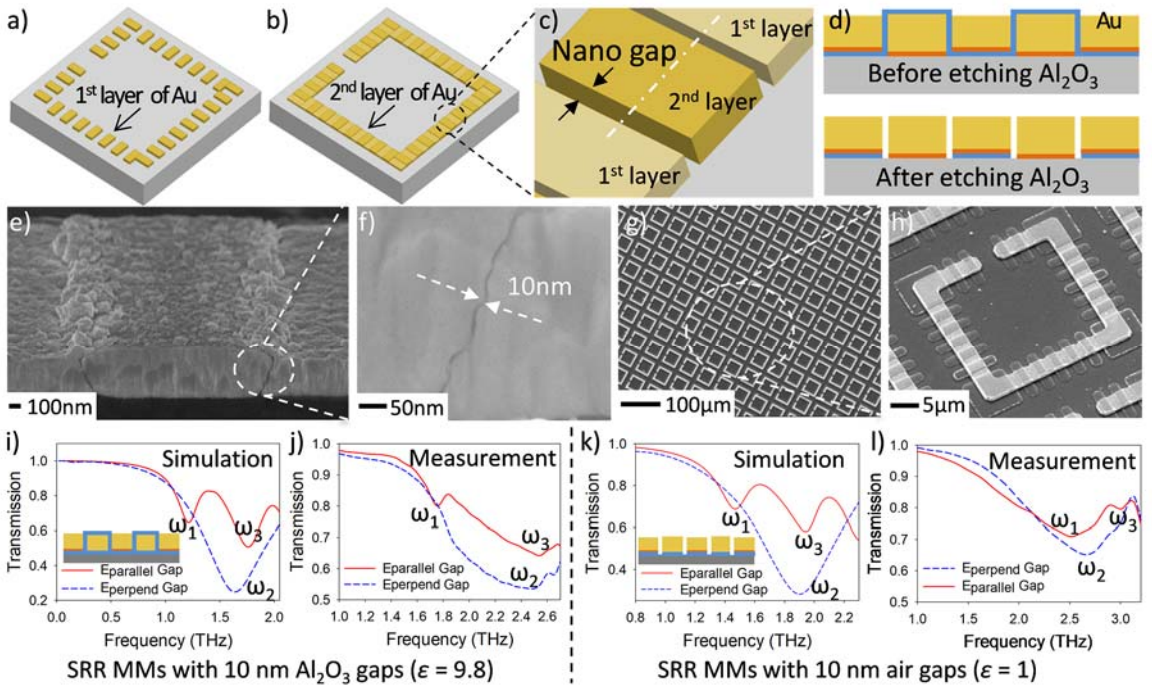

Figure 6.5 Fabrication scheme and experimental characterization of slit-based SRRs [245]. (a-d) Fabrication scheme of slit-based SRRs, which involves (a) electroplating deposition of first Au slit layer on high-resistive Si substrate and (b) ALD of nano-scale Al_2O_3 layer followed by electroplating deposition of second Au slit layer. (c, d) Nano gap is defined by ALD Al_2O_3 (blue) between two Au slit layers (yellow). Al_2O_3 can also be removed using wet etching process to make air gaps between Au slits. (e-h) SEM images of slit-based SRR array with 10 nm nano gaps between Au slits. Simulated (i) and

measured (j) transmission spectra of slit-based SRRs with 10 nm Al_2O_3 gaps clearly show three resonant modes. Simulated (k) and measured (l) transmission spectra of slit-based SRRs with 10 nm vacuum gaps also show three resonant modes. Both measured spectra match with simulation results. The measurement is performed using THz time-domain spectroscopy in Los Alamos National Laboratory.

6.6.2 Measurement

Transmission spectra of the slit-based SRR samples were characterized by a simulator (figure 6.5i and k) and THz time-domain spectroscopy (figure 6.5j and l) with (figure 6.5i and j) and without the Al_2O_3 layer (figure 6.5k and l) [245]. To measure a high Q-factor resonance, a longer time scan can be taken by either adding a thicker substrate of few tens of millimeters or removing the substrate completely to enable a free standing sample. Alternatively, a high-resolution continuous-wave THz spectrometer can be employed for the sample measurements. For the slit-based SRRs with a 10 nm Al_2O_3 gap, 3 resonant peaks can be clearly observed in both the simulated (figure 6.5i) and experimental transmission spectra (figure 6.5j). For the slit-based SRR with a 10 nm air gap, three resonant peaks can also be seen in both the simulation (figure 6.5k) and the experiment (figure 6.5l). In both cases, the resonant frequency of the air gap slit-based SRR is higher than the frequency of the slit-based SRR with an Al_2O_3 gap. This is due to the fact that the decrease of the permittivity of the nano gap (ε from 9.8 to 1) results in the decrease of the total capacitance (C) of the SRR, which leads to increase of the resonant frequency (f) (figure 6.5k and l). Since the slit-based SRR has less slits and nano gaps compared to the nanopillar-based SRR, the Q-factor enhancement of the slit-based SRR is

not as large as the nanopillar-based SRR. Yet a high Q-factor of 38.6 can still be achieved using the slit-based SRR, which is 4.4 times higher than the Q-factor of a traditional film-based SRR. The resonant behaviors of slit-based SRRs obtained by THz measurements match the resonant behaviors of the slit-based SRRs from the simulation results, which fully supports the theories of the displacement current driven resonance in SRR MMs.

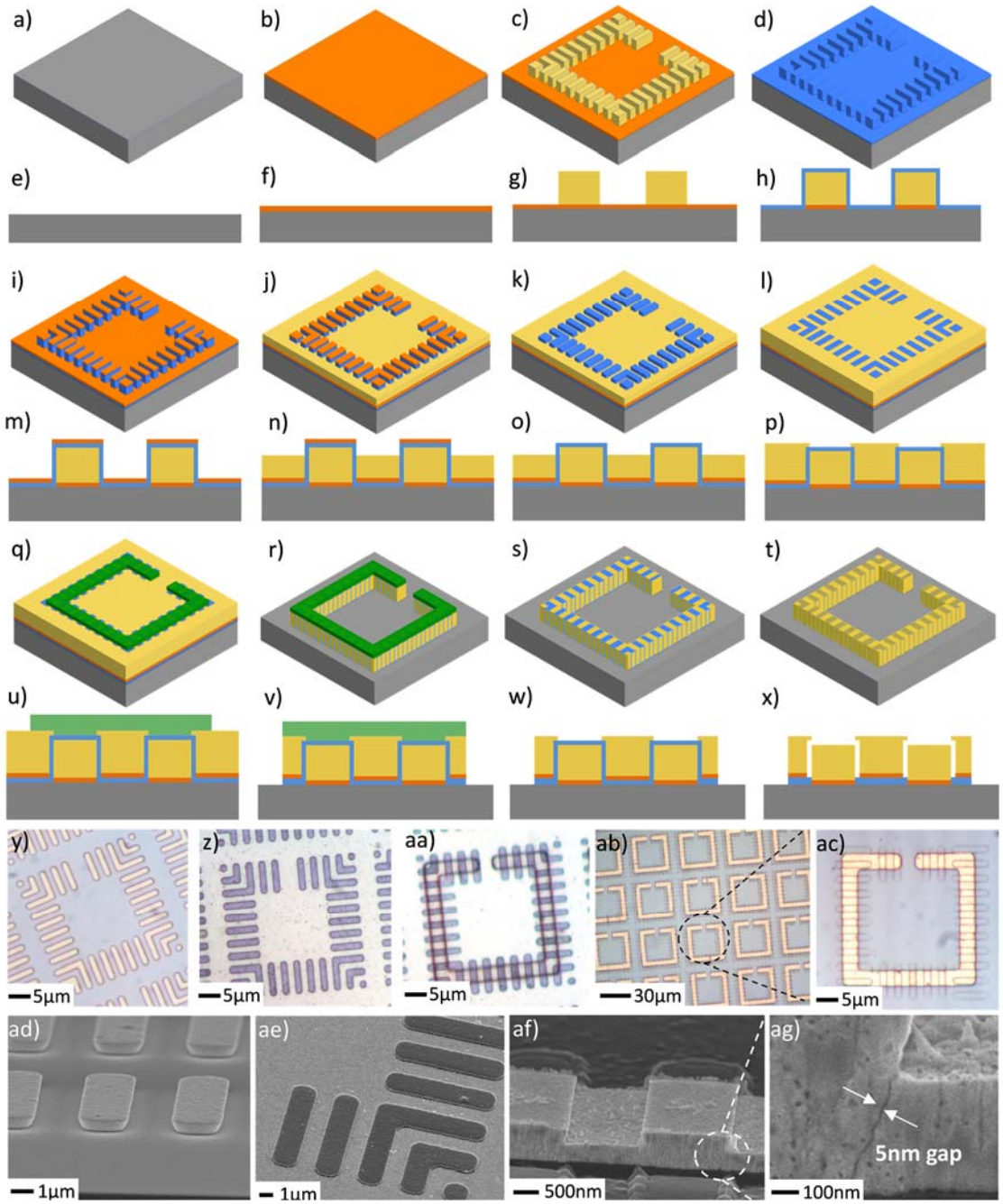

Figure 6.6 Details of the fabrication process of slit-based SRRs [245]. (a, e) High-resistive (560 - 840 Ohm·cm) Si substrate. (b, f) 5 nm Cr and 10 nm Cu deposited on Si substrate using an E-beam evaporation process. (c, g) 400 nm thick Au slits (the width of

the Au slit is 2 μm and the length of the slit is 4 μm) patterned on Cu layer using photolithography and electroplating process. (d, h) Cr and Cu were etched away using wet etching process followed by deposition of 5 nm Al_2O_3 between each Au slit (Blue color in schematic) with an ALD system. (i, m) Another 5 nm Cr and 10 nm Cu layer deposited on top of Au and Al_2O_3 using an E-beam evaporation process. Since E-Beam evaporation was used to directly deposit Cr and Cu without rotating the sample, Cr and Cu are only deposited on the top surface of the structure. (j, n) An Au electroplating process was used to deposit a second layer of Au between the first Au slits to form Al_2O_3 nano-gaps between first and second layers of Au. (k, o) Cr and Cu on top of the sample were etched away using a wet etching process. (l, p) An additional layer of Au was deposited to fully fill the gap between two Au layers. (q, u) SRR C-shape was patterned with S1813 photoresist on top of the sample using photolithography process. (r, v) Au outside the C-shape was etched away using an ion milling process. (s, w) S1813 photoresist was removed using acetone completing the fabrication of the slit-based SRR with 5 nm Al_2O_3 nano gaps (t, x) Al_2O_3 can be further etched away using HF solution to create air nano gaps. (y) An optical image of first layer of Au slits on Si substrate. (z) An optical image of the second layer of Au deposited between first Au slits. (aa) An optical mage of SRR C-shape comprised of S1813 photoresist on top of the sample. (ab) A slit-based-SRR array after ion milling process. (ac) A zoomed-in optical image of single slit-based SRR. (ad) A SEM image of first layer of Au slits deposited on Si substrate. (ae) A SEM image of the second layer of Au deposited between the first Au slits. (af) A cross-sectional SEM image of slit-based SRRs after an ion milling process. (ag) A SEM images showing 5 nm gap between two Au slits.

6.7 Nanopillar-based closed ring resonators

6.7.1 Overview

High Q SRR MM using nanopillars with nano-scale gaps has been discussed in precious sections. A high Q value of more than 400 can be achieved by using nanopillars and displacement currents in the SRRs. A high Q-factor of the MM means that the MM has a high signal-to-noise ratio, which leads to high sensitivity and selectivity as MM sensors and MM frequency tunable devices. However, the Q-factor of current nanopillar-based SRR is still not high enough to develop ultra-sensitive sensors using THz MM devices.

An ultra-high Q MM, a nanopillar-based CRR is designed, simulated and fabricated to achieve an ultra-high Q of around 14000. Nanopillar-based CRR has a Q-factor more than 30 times higher than the Q-factor of nanopillar-based SRR. The designed nanopillar-based CRR shares the concept of nanopillar-based SRR, which using nanoscale gaps (5 nm to 200 nm) between Au nanopillars to reduce the energy loss due to electrical current passing through conductors (Au nanopillars) [245]. A strong electric field can be trapped inside the nano gaps, leading to a high Q-factor. However, an ultra-high Q-factor can be achieved by closing the split of the nanopillar-based SRR to form a nanopillar-based CRR. When the electromagnetic wave is perpendicular to the SRR plane, two different modes can be excited depending on the orientation of the electric field [285-288]. If the electric field is parallel to the split of the SRR, due to the asymmetry of SRR along the electric

field, different charge densities will be generated on the arms with and without the split. The charge density difference produces a loop of current around the SRR. In such situation, the SRR acts as a LC circuit with the inductance (L) along the SRR arms and the capacitance (C) in the split of the SRR. The resonance excited by the electric field parallel to the split is called electric field excited magnetic response (EEMR). On the other hand, if the electric field is parallel to the two continuous SRR arms without the split, the SRR is symmetric along the electric field. Since the charges are equally distributed along the two continuous arms of the SRR, no loop current will be generated. However, current does oscillate in the two continuous SRR arms following the electric field. This resonance of the SRR is called electric field excited response (ER) [286]. For EEMR of the SRRs, the charge densities of the split arm is much smaller than that of the continuous arm due to the split breaking the electric field, leading to a much smaller total charge density (q) compared to that of the ER of the SRRs. Since the energy stored in the SRR (U) is the sum of the energy stored in each small capacitors (consists of two Au nanopillars and the nano gap between them) of the SRRs, the U is proportional to q^2 ($U=q^2/2C$) [289]. Thus the Q-factor of the ER is much higher than the Q-factor of the EEMR of the SRRs. By closing the split of the nanopillar-based SRR to form the nanopillar-based CRR, the nanopillar-based CRR is always in ER mode regardless of the orientation of the electric field. Thus an ultra-high Q-factor can be achieved. In addition, a circular shape nanopillar is used to further increase the spaces between the Au nanopillars, which further improve the Q-factor.

6.7.2 Theory

The nanopillar-based CRR is illustrated in figure 6.7a-c. An array of the nanopillar-based CRR is built on a Si substrate with the electromagnetic wave perpendicular to the CRR plane and electric and magnetic field parallel with the CRR arms (figure 6.7a). The electric field applied to the nanopillar-based CRR generates displacement current inside the nano gaps between each two Au nanopillars. The displacement current in the nano gaps and the electrical current in the Au nanopillars form the total current oscillating inside the CRRs, resulting in the resonant behaviors (figure 6.7b and 6.7c). Figure 6.7d and 6.7e show the geometric configurations of the conventional film-based CRR and the nanopillar-based CRR respectively. The geometric parameters of the CRR include the width of the CRR (W), the width/length of the CRR (a), the size of the nanopillar (d), the diameter of the nanopillar (D) and the permittivity of the nano gap (ε). The transmission spectra of the film-based CRR (black line) and the nanopillar-based CRR (red line) is compared and shown in figure 6.7f. It can be clearly seen that the resonant peak of the nanopillar-based CRR is much sharper than that of the film-based CRR. The electric field distributions of the film-based CRR and nanopillar-based CRR are also studied (figure 6.7g-i). A much higher field enhancement (7×10^6 V/m) can be seen inside the nano gaps of the nanopillar-based CRRs, which is 10 times larger than that of the film-based CRR (with a maximum electric field intensity of 7×10^5 V/m). This illustrates that the nano gaps of the nanopillar-based CRR improves that energy storage of the CRR, which leads to a high Q-factor (equation 8).

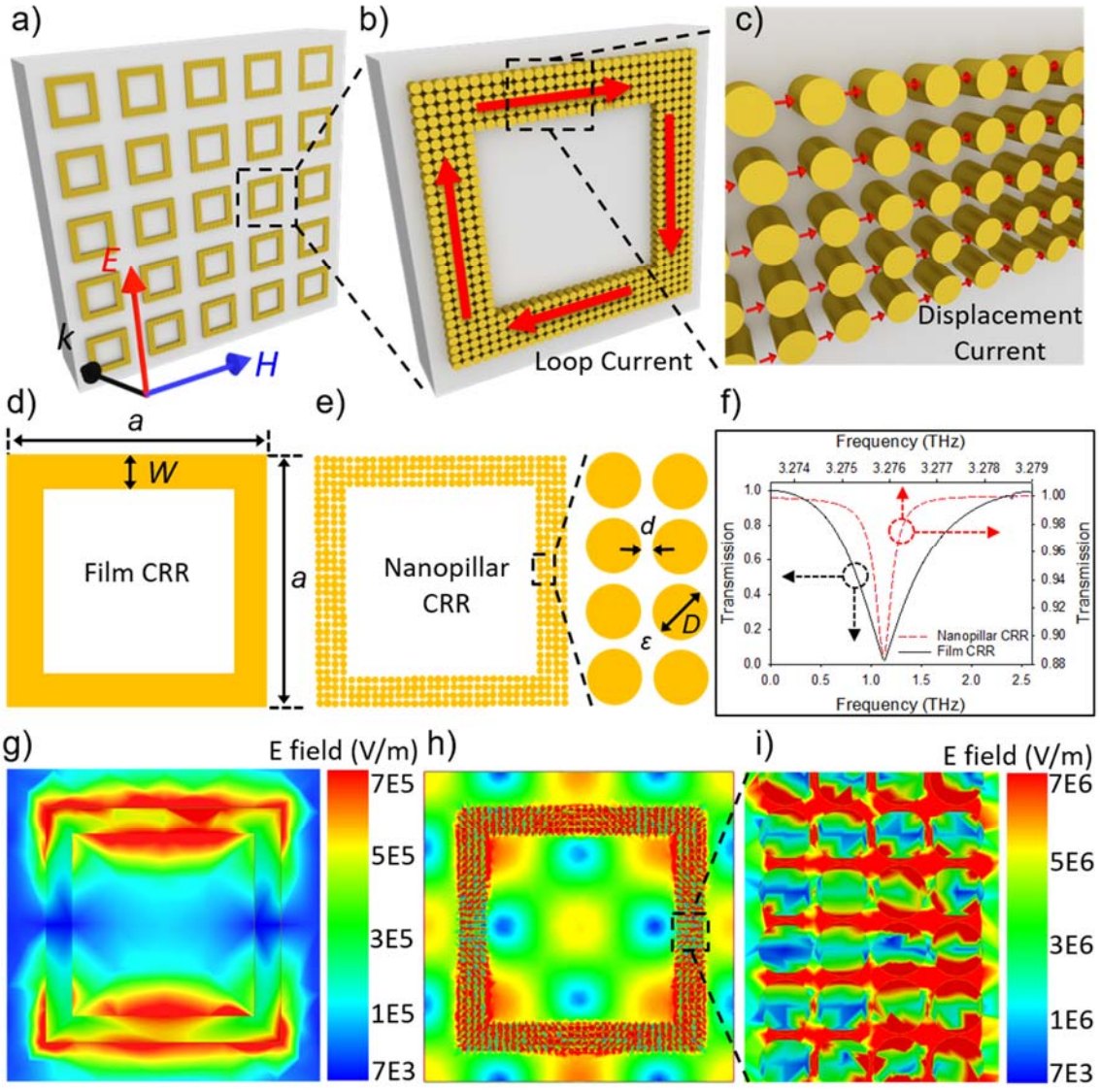

Figure 6.7 Illustration of nanopillar-based CRR. (a) An array of nanopillar-based CRR. (b) A single nanopillar-based CRR. (c) The Au nanopillars and nano gaps between them. (d) Film-based CRR and (e) nanopillar-based CRR with different configurable parameters. (f) Transmission spectra of both film and nanopillar-based CRRs. Electric field distribution of (g) film-based CRR and (h, i) nanopillar-based CRR.

6.7.3 Fabrication process

The Nanopillar-based CRR is fabricated on a Si substrate. The detailed fabrication process is shown in figure 6.8. First, a thin layer of photoresist PMMA A3 (MicroChem) was spun coated on the Si substrate (figure 6.8a) at 3000 rpm to achieve a thickness of 200 nm. Circular Nanopillars were then patterned on the photoresist using electron beam (e-beam) lithography and lift-off process (figure 6.8b). A 30 nm thick Au was deposited on the sample using e-beam evaporation process (figure 6.8c). The photoresist was then lifted off by immerging the sample in acetone and rinsed using deionized (DI) water (figure 6.8d). Scanning electron microscope (SEM) images show the array of nanopillar-based CRRs (figure 6.8e), a zoomed-in image of a single nanopillar-based CRR (figure 6.8f) and the Au nanopillars (figure 6.8g). The diameter of the Au nanopillar is 1 μm and the thickness of the Au nanopillar is 30 nm. Figure 6.8h also shows the 50 nm gap between two Au nanopillars. The well-defined nanopillars and nano gaps indicate the successful fabrication process of nanopillar-based CRRs. A nanopillar-based CRR array with a large area can also be achieved, showing the feasibility of designing and fabricating large devices using such structures.

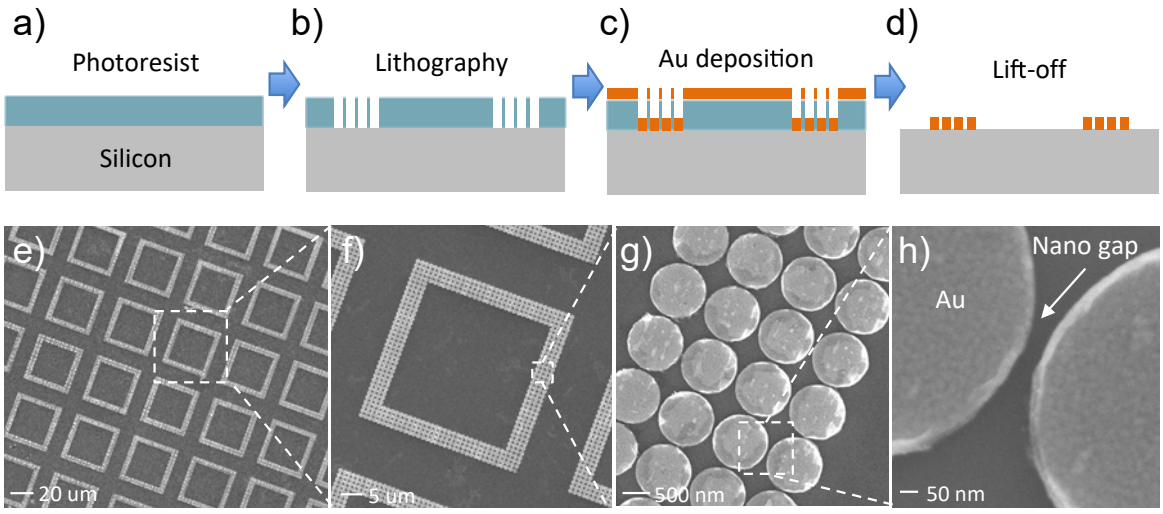

Figure 6.8 Fabrication process of the nanopillar-based CRRs. (a-d) Fabrication of nanopillar-based CRRs using E-beam lithography, E-beam evaporation and lift-off methods. (e) A SEM image of an array of nanopillar-based CRRs. (f) A SEM image of a single nanopillar-based CRR. (g) A SEM image of an array of Au nanopillars. (h) A SEM image shows the 50 nm gap between two Au nanopillars.

6.7.4 Transmission and frequency comparison

To analyze the resonant behaviors of the nanopillar-based CRRs, transmission spectra of the nanopillar-based CRRs with various geometric parameters were studies (figure 6.9a-d). The geometric parameters of the nanopillars include the size of the nano gaps (d) between the nanopillars, the thickness of the nanopillars (h), the diameter of the circular nanopillar (D), and the permittivity of the media (ε) where the nanopillar-based CRR is located (including permittivity of the nano gaps). As shown in figure 6.9a, the magnitude of the resonant peak of the nanopillar-based CRRs increases with an increase

of the nano gap sizes (from 5 nm to 100 nm). This can be explained by the equation (9) of displacement current (I_d) in the CRRs. When the nano gap size (d) increases, displacement current (I_d) decreases, results in the decrease of the resonant magnitude. On the other hand, the resonant frequency (f) of the nanopillar-based CRR increases with the increase of the nano gap size (d) due to the decrease of the capacitance (C) of the CRR, leading to the increase of the angular frequency of the CRR (ω):

$$f = \frac{\omega}{2\pi} = \frac{1}{2\pi\sqrt{LC}} = \frac{1}{2\pi\sqrt{L\varepsilon\frac{A}{d}}} \tag{10}$$

Where f is the frequency of the electromagnetic wave, L is the inductance of the CRR (H), and C is the capacitance of the CRR (F). Figure 6.9b and 6.9c show the effect of Au nanopillar thickness (h) and diameter (D) on the resonant behaviors of the nanopillar-based CRRs (with an increase of h from 100 nm to 1000 nm and an increase of D from 0.5 μm to 1=2 μm). The resonant magnitude decreases with the increase of h and/or D. This is because that h and D determine the side area of the nanopillars ($A = h*D$). The increase of h and/or D results in the increase of A, leading to the decrease of I_d based on equation (9). In addition, the resonant frequency (f) decreases with the increase of h and/or D, which can be explained from equation (10): the increase of h and/or D leads to the increase of A, which decreases f. The permittivity of the media (ε) also plays an important role in tuning the resonant behavior of the nanopillar-based CRRs. The resonant magnitude is proportional to ε and inversely related to ε (figure 6.9d). This can also be demonstrated by equation (9) and equation (10). The resonant frequency (red line) and magnitude (black line) of the nanopillar-based CRRs are also quantitatively analyzed, shown in figure 6.9e-

6.9h. It is noted that the value of the transmission of the opposite to the resonant magnitude of the CRRs (1 means totally reflected or absorption and 0 means totally transmitted). It can be observed from figure 6.9e – 6.9h that the resonant magnitude and frequency have the opposite response to all the geometric parameters (d, h, D, and ε), which agrees well with the theory in equation (9) and equation (10).

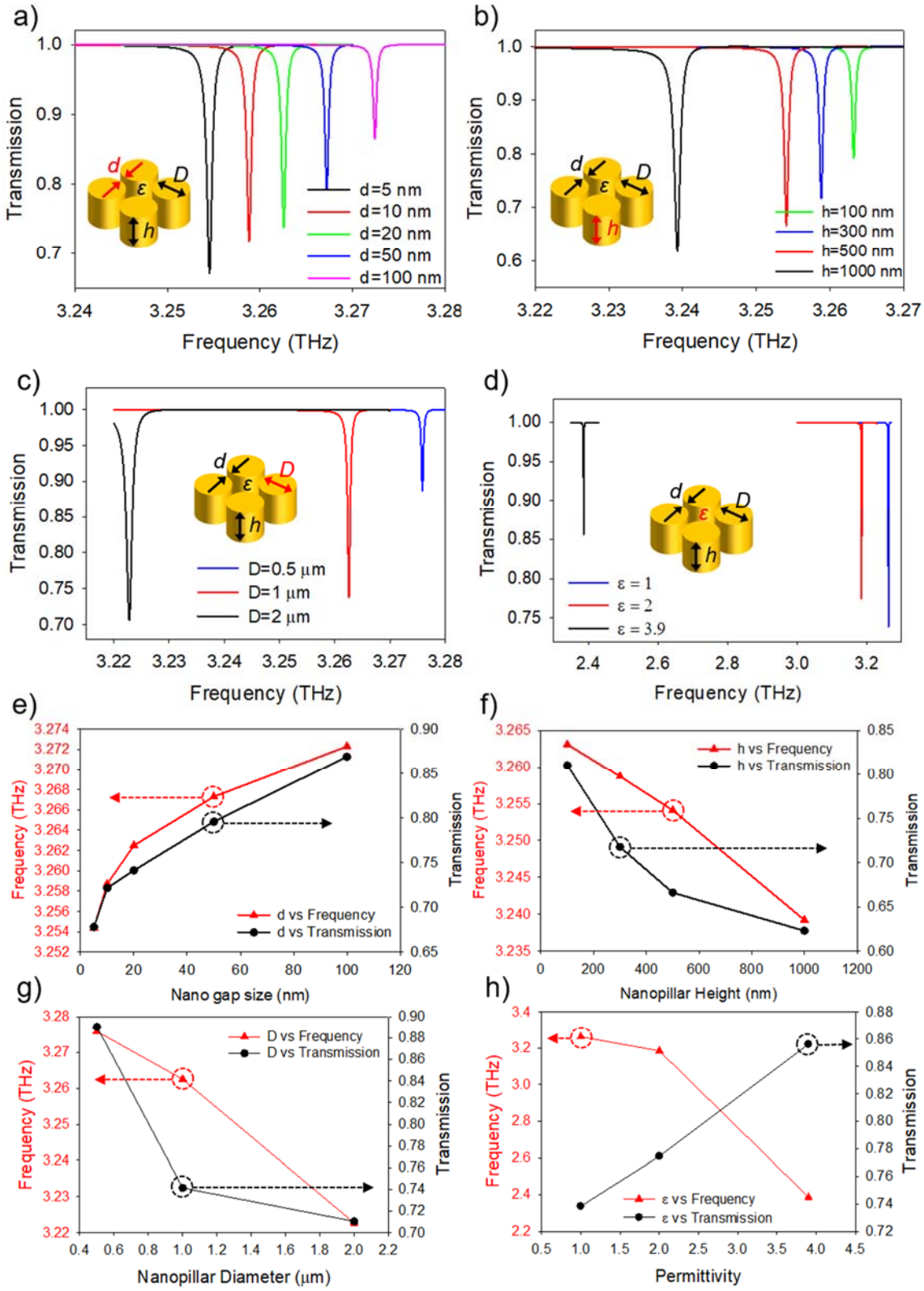
a)
Transmission
Frequency (THz)
d=5 nm
d=10 nm
d=20 nm
d=50 nm
d=100 nm
b)
Transmission
Frequency (THz)
h=100 nm
h=300 nm
h=500 nm
h=1000 nm
c)
Transmission
Frequency (THz)
D=0.5 μm
D=1 μm
D=2 μm
d)
Transmission
Frequency (THz)
ε = 1
ε = 2
ε = 3.9
e)
Frequency (THz)
Transmission
Nano gap size (nm)
d vs Frequency
d vs Transmission
f)
Frequency (THz)
Transmission
Nanopillar Height (nm)
h vs Frequency
h vs Transmission
g)
Frequency (THz)
Transmission
Nanopillar Diameter (μm)
D vs Frequency
D vs Transmission
h)
Frequency (THz)
Transmission
Permittivity
ε vs Frequency
ε vs Transmission

Figure 6.9 Transmission analysis of the nanopillar-based CRRs. (a-d) Transmission spectra of nanopillar-based CRRs with (a) different nano gap size, (b) different nanopillar thickness, (c) different nanopillar diameter, and (d) different permittivity. (e-h) Resonant frequency and magnitude comparisons of the nanopillar-based CRRs with (e) different nano gap size, (f) different nanopillar thickness, (g) different nanopillar diameter, and (h) different permittivity.

6.7.5 Ultra-high quality factor

To quantitatively and qualitatively analyze the Q-factor of the nanopillar-based CRRs, the Q-factor of the nanopillar-based CRRs with different geometric parameters is also studied (Figure 6.10). The Q-factor of the nanopillar-based CRRs largely depends on the energy storage (U) inside the CRRs. Since nanopillars and nano gaps are used to construct the CRRs, thousands of capacitors (between every two Au nanopillars) are formed inside the CRRs. The total energy stored in the nanopillar-based CRR can be regarded as the sum of the energy stored in each capacitor made of Au nanopillars and nano gaps. The energy storage of such capacitors can be expressed with the charges (q) of the Au nanopillars and the capacitance (C) of the capacitors:

$$U = \frac{q^2}{2C} = \frac{q^2}{2\varepsilon \frac{A}{d}} \tag{11}$$

It is assumed that the total charges of the CRR (q) does not change due to the same electromagnetic field applied to all nanopillar-based CRRs and the same configuration of the CRR structure. The total energy storage (U) of the nanopillar-based CRR is inversely

proportional to the total capacitance (C) of the CRR. Thus the Q-factor of the nanopillar-based CRR is inversely proportional to the total capacitance (C) of the CRR. Figure 6.10a and 6.10b illustrate the Q-factor change with different nanopillar thickness (h) of 300 nm, 500 nm and 1000 nm. Since the side area (A) of the nanopillar increases with the thickness of the nanopillar (h), the capacitance (C) of the CRR also increases, leading to the decrease of the Q-factors (figure 6.10a). The increase of the nano gap size (d) decreases the C value, results in the increase of the Q-factors (figure 6.10b). A three-dimensional 3D plot (figure 6.10b) demonstrates the effects of both h and d on Q-factors of the nanopillar-based CRRs. It is clearly shown that the highest Q of around 12000 can be achieved with the largest nano gap size (d) and smallest nanopillar thickness (h). The diameter of the nanopillars (D) and the permittivity (ε) of the media are fixed to 0.5 μm and 1 respectively in this case. Similarly, the diameter (D) of the nanopillars also increases the A of the nanopillars, thus increases the Q of the nanopillar-based CRRs (figure 6.10c). The 3D plot of figure 6.10d shows that a highest Q of around 14000 can be achieved by increasing the size (d) of the nano gaps and decreasing the diameter (D) of the nanopillars. The thickness of the nanopillars (h) and the permittivity (ε) of the media are fixed to 300 nm and 1 respectively in this case. Figure 6.10e and 6.10f indicate the change of permittivity (ε) to the Q-factors. The total C value of the nanopillar-based CRR is proportional to ε. Thus the increase of ε results in a lower Q value (figure 6.10e). A highest Q of around 12000 can be achieved with a large nano gap size (d) of 200 nm and a low permittivity (ε) of 1. The thickness (h) and diameter (D) of the nanopillars are fixed to 300 nm and 0.5 μm respectively in this case. Since a larger charge distribution can be achieved using nanopillar-based CRRs compared to the nanopillar-based SRRs, an ultra-high Q-factor of

around 14000 can be obtained. Such ultra-high Q is more than 45 times of the reported Q-factor of the nanopillar-based SRRs (with a Q-factor of around 300).

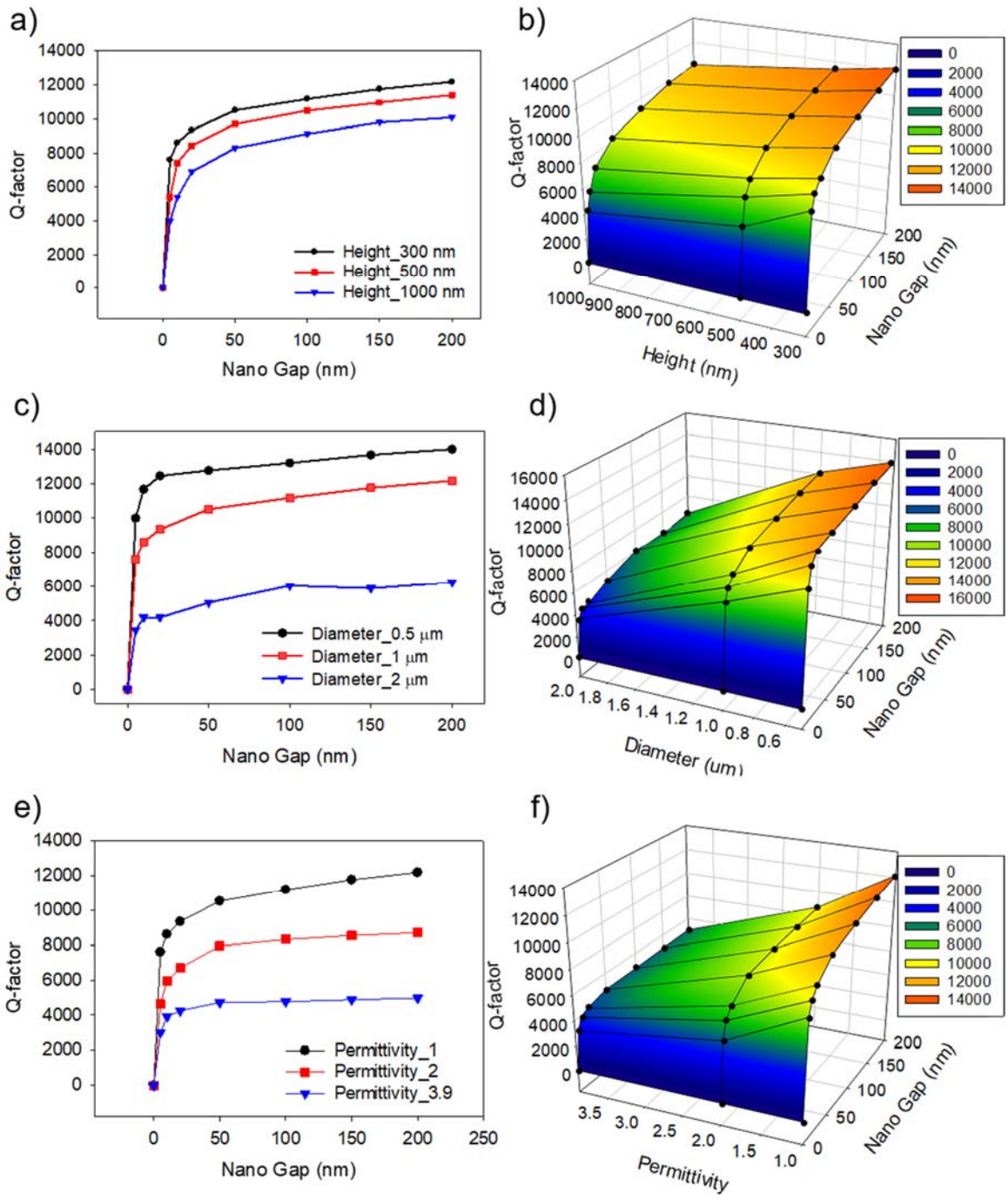

Figure 6.10 Q-factor analysis of the nanopillar-based CRRs. (a, b) Q-factors of the nanopillar-based CRRs with different nanopillar thicknesses. (c, d) Q-factors of the

nanopillar-based CRRs with different nanopillar diameters. (e, f) Q-factors of the nanopillar-based CRRs with different permittivity.

6.7.6 Nanopillar configuration discussion

To illustrate the importance of the nano gaps and nanopillars to the Q-factors of the nanopillar-based CRRs, the shape and configurations of the nanopillars inside the CRRs are studied (figure 6.11). The shapes of the nanopillars include circle, square, triangle and hexagon (figure 6.11a-d). The total number of the nanopillars inside the CRR and the size of the nano gaps remain the same for comparison. Different shapes of nanopillars result in the difference in the total volume of the Au nanopillars in the CRR (figure 6.11e). Since the increase of the volume of the Au nanopillars introduces more Ohmic losses to the CRR, the Q-factor of the nanopillar-based decreases (figure 6.11e and 6.11f). It is noted that the Q-factor of the CRR with the circular nanopillars has a significant Q-factor improvement over other nanopillar shapes (square, triangle and hexagon). This is due to the fact that the sidewall of the circular nanopillar is in an arc shape. The nano gap size (d) of the nanopillars only defines the shortest distance between the two nanopillars. However the actual space between the two circular nanopillars is much larger than d. On the other hand, the space between square/triangle/hexagon is strictly defined by the nano gap size (d). The large space between circular nanopillars leads to the decrease of the capacitance (C) of the CRR, which enhances the Q-factor (figure 6.11e and 6.11f). Figure 6.11g illustrates the relationship among volume of the nanopillars, nano gap sizes and Q-factors

of the nanopillar-based CRRs. A highest Q of around 12000 can be achieved with the smallest volume of Au nanopillars (circular shape nanopillars) and the largest nano gap size of 200 nm.

Two different configurations (aligned nanopillar and zigzag nanopillar) of the nanopillars inside the CRRs are shown in figure 6.11h and 6.11i respectively. The nanopillars in both configurations are arranged in such way that the current flow in the CRR is always in parallel with the nano gap (figure 6.11j). Since different configurations of nanopillars results in the changes in the capacitance of the nanopillar-based CRRs, the Q-factor will also change accordingly. The simulated Q-factors of the aligned nanopillar-based CRRs (black line) and the zigzag nanopillar-based CRRs (red line) are plotted, shown in Figure 6.11k. It is shown that the zigzag nanopillar-based CRR has a Q-factor higher than that of the aligned nanopillar-based CRRs under various nano gap sizes (d, 5 nm to 200 nm). The total capacitance of the nanopillar-based CRRs with aligned (black line) and zigzagged (red line) configuration is modeled and calculated, shown in figure 6.11l. The zigzag nanopillar-based CRR has a lower total capacitance compared to the aligned nanopillar-based CRR due to the total shorter distance among nanopillars ($C = \varepsilon A/d$). Assuming the charge densities (q) does not change between aligned and zigzag nanopillar-based CRRs, the energy stored (U) in the zigzag nanopillar-based CRR is larger than that of the aligned nanopillar-based CRR based on equation 11, leading to a higher Q-factor. Figure 6.11m shows the Q-factor difference between the aligned and zigzag nanopillar-based CRRs at different nano gap sizes. The decrease of the nano gap size increases the Q-factor difference between the aligned and the zigzag nanopillar-based CRRs. A largest Q-factor difference of around 3000 can be achieved at the nano gap size

of 5 nm. This phenomenon can be explained by the total capacitance difference between the aligned and the zigzag nanopillars (figure 6.11n). The total capacitance difference reaches to its maximum of 0.06 pF at a nano gap size of 5 nm, leading to a maximum Q-factor difference of around 3000. The changes of Q-factors of the nanopillar-based CRRs under different conditions provide a comprehensive approach to understand how nanopillar-based MM works. The ability to tune the resonant behaviors and Q-factors by adjusting the shapes and the configurations of the nanopillars inside the CRRs provides a unique and easy method to design tunable MM devices and sensors, which is suitable for various applications like THz MM filters and modulators, plasmonic devices and biomedical MM sensors.

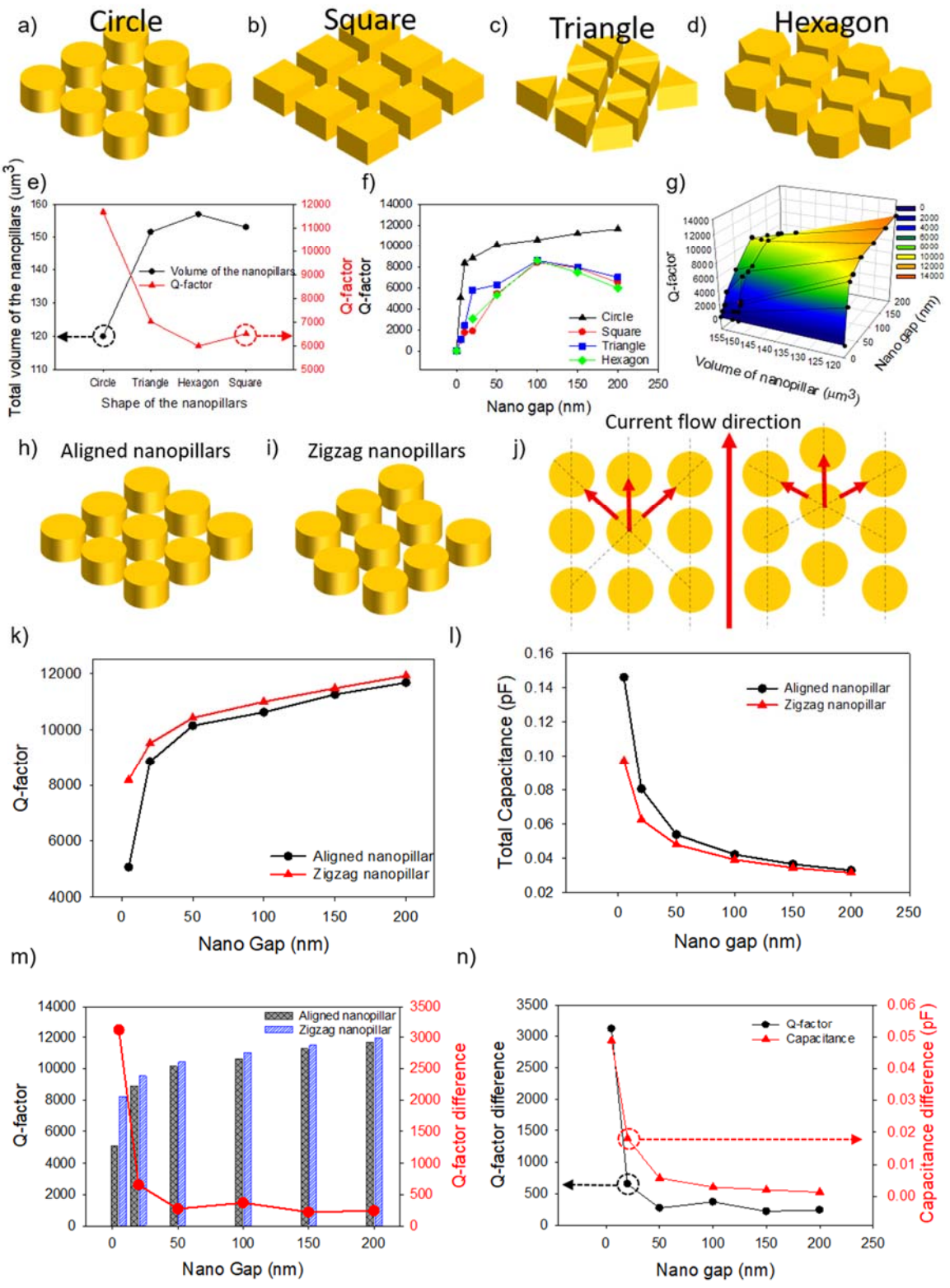

Figure 6.11 Nanopillar shape and configuration analysis. (a-d) Different nanopillar shapes of (a) circle, (b) square, (c) triangle, and (d) hexagon. (e) Total volume of the nanopillar

and Q-factor of the nanopillar-based CRR with different nanopillar shapes. (f) Q-factor of the nanopillar-based CRR with different nanopillar shapes at different nano gap sizes. (g) A 3D plot of the Q-factors with different nano gap sizes and different total volume of the nanopillars. Different configurations of the nanopillars with (h) aligned and (i) zigzag nanopillars. (j) Top view of the aligned and zigzag nanopillars and the current flow direction. (k) Q-factor of the nanopillar-based CRR with different nanopillar configurations. (l) Total capacitance of the nanopillar-based CRRs with different nanopillar configurations. (m) Q-factor difference between the aligned and the zigzag nanopillar-based CRRs at different nano gap sizes. (n) Comparison between Q-factor difference and total capacitance difference of the aligned and zigzag nanopillar-based CRRs at different nano gap sizes.

6.7.7 Example of high Q 3D MM – electromagnetic cloaking

One 3D MM application is electromagnetic cloaking by using the MM structure to manipulate the path of electromagnetic wave around the MM structure. This can be realized by designing a 3D thick MM shell with unique permeability and permittivity that are related to their coordinates in the cylindrical region of the MM shell (figure 6.12). The permittivity and permeability of the MM within the cloaking shell can be expressed using the following equations [290]:

$$\varepsilon_r = \frac{r - R_1}{r} \tag{12}$$

$$\varepsilon_\phi = \frac{r}{r - R_1} \tag{13}$$

$$\mu_z = \left(\frac{R_2}{R_2 - R_1}\right)^2 \frac{r - R_1}{r} \tag{14}$$

Where *R1* and *R2* are the inner and outer radiuses of the cloaking shell (figure 6.12a), ε_r and ε_ϕ and μ_z are the permittivity and permeability in cylindrical coordinate, and r is the one axis in the cylindrical coordinate defining the distance between the origin and a random point in the coordinate.

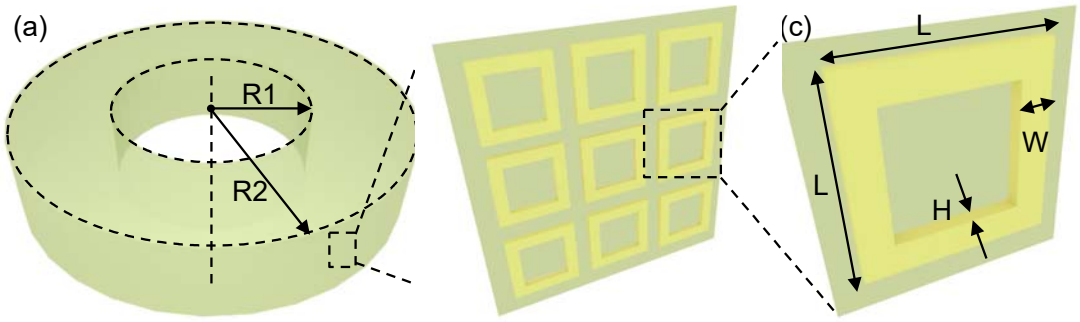

Figure 6.12 Electromagnetic cloaking using 3D MM designs. (a) 3D cloaking shell structure with inner radius R1 and outer radius R2. (b) The cloaking structure can be made of array of MMs (e.g., CRRs). (c) The CRR is made of Au ring with a length *L*, a width *W*, and a thickness *H*.

To characterize the MM cloaking system, electric field passing through the MM cloak was modeled using finite-difference time-domain (FDTD) method [291]. The modeling was conducted using MATLAB and the script can be found in appendix A. The electromagnetic wave flows from the bottom of the field (Y = 0 mm) towards to the top of the field (Y = 1000 mm) (figure 6.13). The MM cloak structure lies in the middle of the field with a center coordinate of (400 mm, 400 mm). The inner radius (*R1*) of the cloak is 100 mm and the outer radius (*R2*) of the cloak is 200 mm (figure 6.13). When the

electromagnetic wave travels through the MM cloak structure, the electromagnetic field interacts with the cloak ruled by the material properties (permittivity and permeability) of the cloak. The cloak material properties are engineered in a way (equation 12-14) that all the electromagnetic fields inside the cloak ($R1 < r < R2$) are steered around the outer boundary of the cloak ($r = R2$) so that any objects placed inside the cloak ($r < R1$) does not impact the path of the electromagnetic wave. The Q-factor of the MM cloak affects cloaking effect (figure 6.13). Figure 6.13 shows the electric field distributions around the MM cloak with different Q-factors (Q = 10, 30, 100, and 1000). The loss tangent ($tan\delta$) of the MM cloak also depends on the Q-factor of the MM [292]:

$$\tan\delta \propto \frac{1}{Q} \tag{15}$$

In ideal cases, the loss tangent ($tan\delta$) of the MM is zero, which makes the MM cloak a perfect absorber [293]. The perfect absorber results in the zero scattering at the boundaries of the cloak ($r = R2$), leading to a perfect cloaking effect (electric field does not affect by the cloak). On the other hand, as the loss tangent ($tan\delta$) of the MM increases, the scattering of the cloak boundary ($r = R2$) also increases, leading to a large interference between the MM cloak and the electromagnetic field around it [293]. Combing equation 15 and the scattering of the cloak, it can be concluded that a large Q-factor of the MM results in the decrease of the cloak boundary scattering, thus leading to a better cloaking effect (figure 6.13).

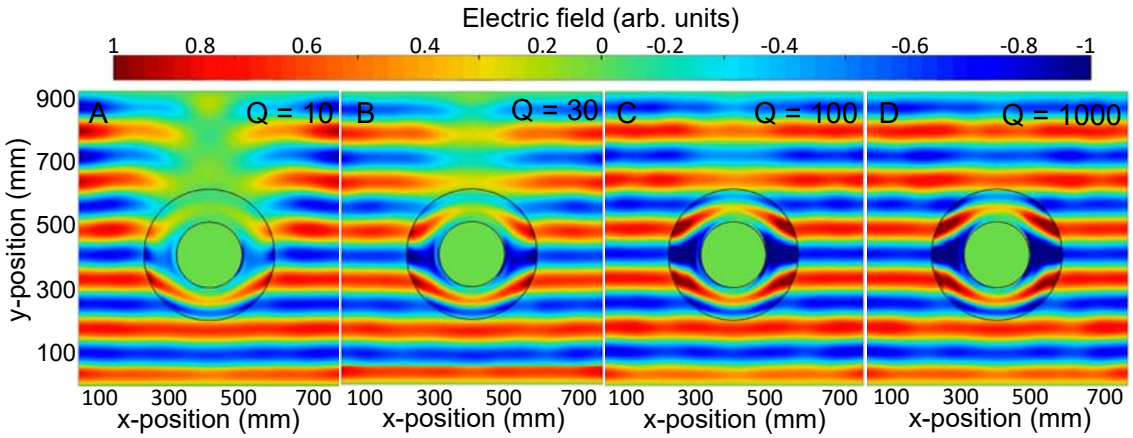

Figure 6.13 Modeled Electric field across the MM cloak with different Q-factor values of the MM. The electromagnetic field flows from the bottom of the field (Y = 0 mm) towards to the top of the field (Y = 1000 mm). (a) MM cloak with a Q of 10. (b) MM cloak with a Q of 30. (c) MM cloak with a Q of 100. (d) MM cloak with a Q of 1000.

Figure 6.14 shows the amplitude of the electric field before and after entering the MM cloak. When there is no loss in the MM cloak (ideal), the amplitude of the electric field remains the same on both side of the cloak (figure 6.14a). For a MM with a Q of 10, the scattering of the cloak boundary is large, leading to a small amplitude of the electric field after the electromagnetic field passed the cloak. Figure 6.14b shows the amplitude changes as well as the percentage of the electric field amplitude compared to its value before entering the cloak. It can be clearly seen that increasing the Q-factor of the MM leads to an electric field amplitude closer to its original values and improves the cloaking effect of the MM cloak. The use of high Q MM improves the cloaking effect for the MM cloak system, which makes near perfect cloaking and even perfect cloaking possible. The perfect cloaking system with high Q MM can be used for various applications like passive sensing and camouflage technique [294].

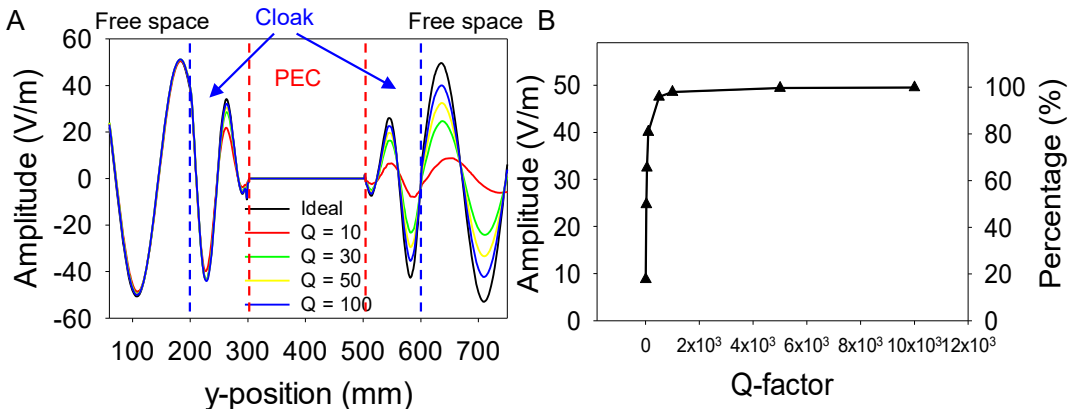

Figure 6.14 Electric field amplitude comparison before and after the electromagnetic wave enters the cloak with different Q-factors.

Chapter 7

3D Self-Assembled Nanopillar-Based Metamaterials

7.1 Design of nanopillar-based 3D metamaterials

7.1.1 Overview

It is noticed from previous chapters that 3D MMs are ideal candidates for 3D sensors due to their unique isotropic and anisotropic behaviors. However, the Q-factor of such 3D MM sensors is usually low, which limits the sensitivity of the 3D MM sensors. It is proved in chapter 6 that by designing nanopillar-based SRRs and CRRs, the Q-factor can be improved dramatically. It is reasonable to come up with the idea of combining these two methods to create 3D MM sensors with nanopillar-based resonator designs.

Figure 7.1 illustrates the idea of 3D nanopillar-based MM structures. X shape resonators are made of thousands of Au nanopillars with 5 nm gaps between them. The nanopillar array forms X-shapes on each face of the cubic structure. Figure 1.7 shows an illustration of the self-assembly process of the nanopillar-based X-shape MM as well as the SEM images of the Au nanopillar array and the 5 nm gap between the nanopillars.

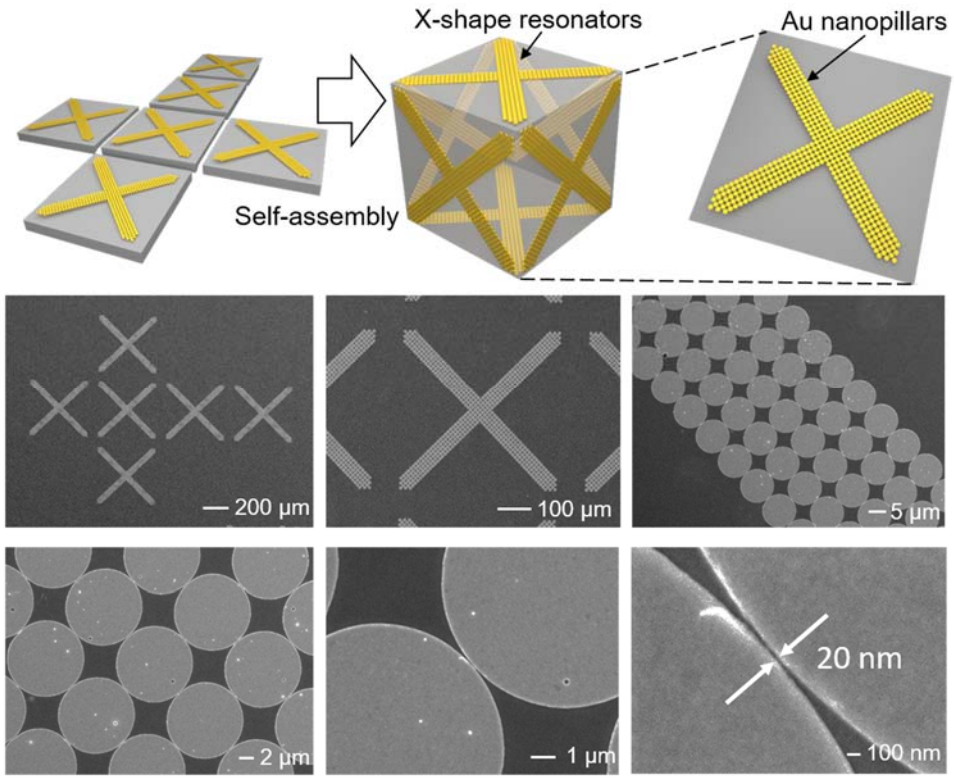

Figure 7.1 3D nanopillar-based X-shape MM using self-assembly technique.

7.1.2 Fabrication strategy

Details of the fabrication process are shown in figure 7.2. First 10 nm Cr adhesion layer and 300 nm Cu sacrificial layer were deposited on a Si substrate (figure 7.2a). Au nanopillars were then patterned on the Cu layer using electron-beam (e-beam) lithography, e-beam evaporation, and lift-off process (figure 7.2b). On top of the Au nanopillars, a 30 nm Al_2O_3 supporting layer and 15 µm SU-8 panels were patterned (figure 7.2c). The purpose of the 30 nm Al_2O_3 is to support the structure (SU-8 panels and SPR-220 hinges) as well as preventing the hinge from sticking to the substrate. A 24 µm thick SPR-220 hinge layer was then patterned between the SU-8 panels on top of the Al_2O_3 supporting

layer (figure 7.2d). The Cu sacrificial layer was then partially etched so that only the center of the structure is attached to the substrate (figure 7.2e). The sample was placed on a hotplate to realize the self-assembly process (figure 7.2f-h). The self-assembled structure can be released from the substrate by etching away the Cu between the structure and the substrate (figure 7.2i). Optical images show the Au nanopillar array (figure 7.2j), Al_2O_3 supporting layer (figure 7.2k), SU-8 panels (figure 7.2l), and SPR-220 hinges (figure 7.2m). Figure 7.2n shows the partially etched Cu supporting the entire structure on a substrate. The self-assembled structure is shown is figure 7.2o.

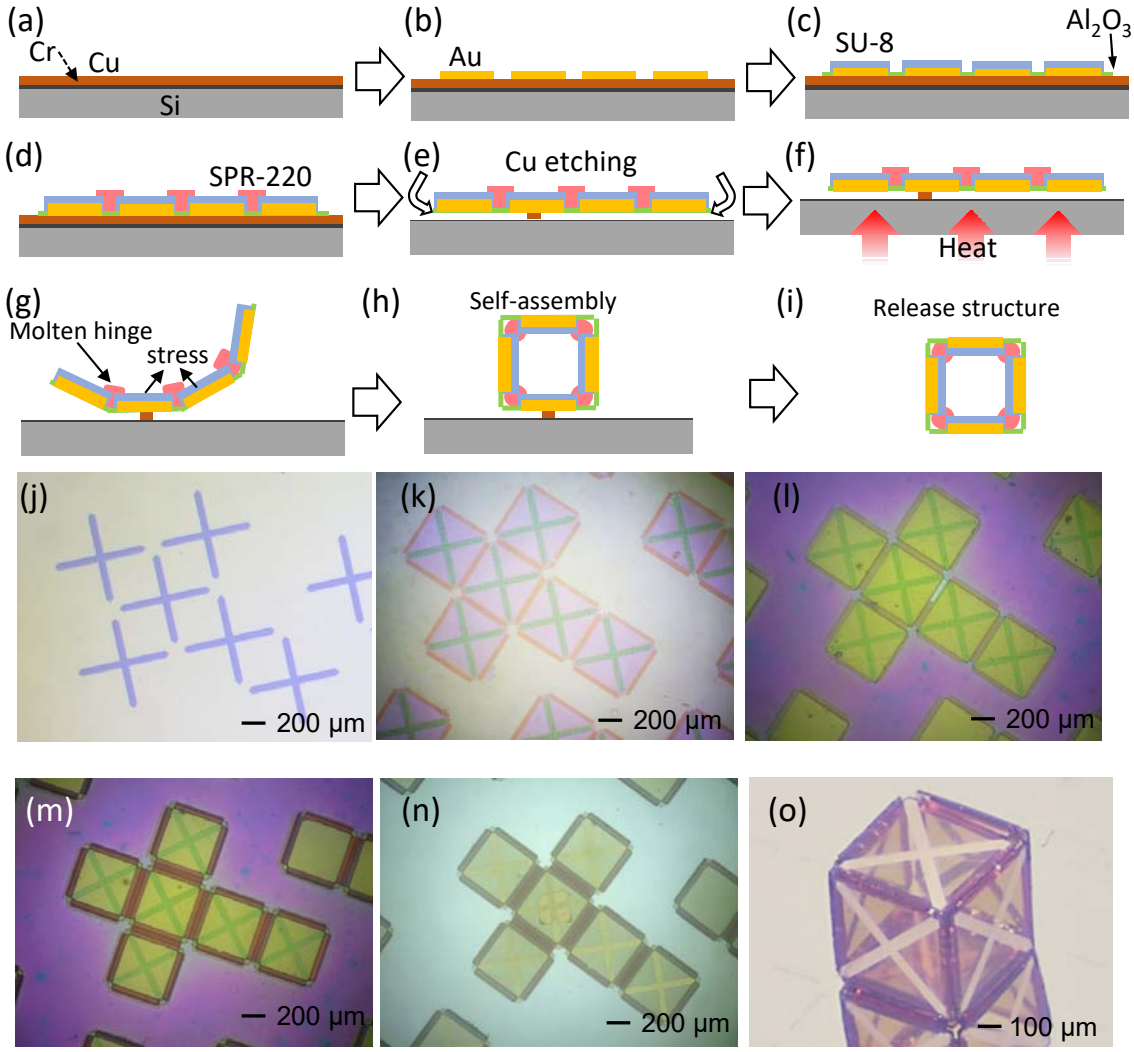

Figure 7.2 Fabrication of 3D nanopillar-based MM using self-assembly process.

7.1.3 Transmission responses

An illustration of the 3D nanopillar-based X-shape MM is shown in figure 7.3a. The 3D nanopillar-based MM contains thousands of Au nanopillars that are patterned in X-shapes on each face of the 3D cubic structure. When the THz electromagnetic field is applied to the 3D nanopillar-based MM, displacement current can be generated inside the nano gaps (figure 7.3b), leading to a resonant behavior. Due to the high Q induced by the nanopillars and the nano gaps, a sharp resonant peak with the Q-factor of around 9000 can be achieved (figure 7.3c), which is much higher than the Q-factor of the 3D film-based MM (with a Q-factor of around 30). Similar to film-based 3D X-shape MM, the 3D nanopillar-based X-shape MM also has isotropic behaviors at different rotation angles. Figure 7.4 shows the simulated transmission responses of the 3D X-shape MM and its rotation along X-, Y-, and Z-axis (figure 7.4a). 6 random rotation angles were applied to the 3D structure along X-, Y- and Z-axis. The resonant frequency responses of the film-based MM and the nanopillar-based MM (first resonant peak and second resonant peak) are shown in figure 7.4b. It can be seen that for all cases, the resonant frequencies remain the same when the 3D structure is rotated, proving that both film-based X-shape MM and nanopillar-based X-shape MM have fully isotropic behaviors. Figure 7.4c and 7.4d illustrate the resonant magnitude and Q-factor changes based on different rotation angles. By comparing both figure 7.4c and figure 7.4d, it is noticed that when the Q-factor of the MM is low, the relative magnitude of the MM is high, which agrees with previous theories. In addition, a highest Q-factor of around 9000 can be achieved using 3D

nanopillar-based MM, which is much higher compared to the Q-factor of a film-based MM (Q-factor = 30). The ultra-high Q of 3D nanopillar-based X-shape MM as well as its fully isotropic behaviors makes it ideal for ultra-sensitive 3D sensors for detecting biomedical and chemical substances.

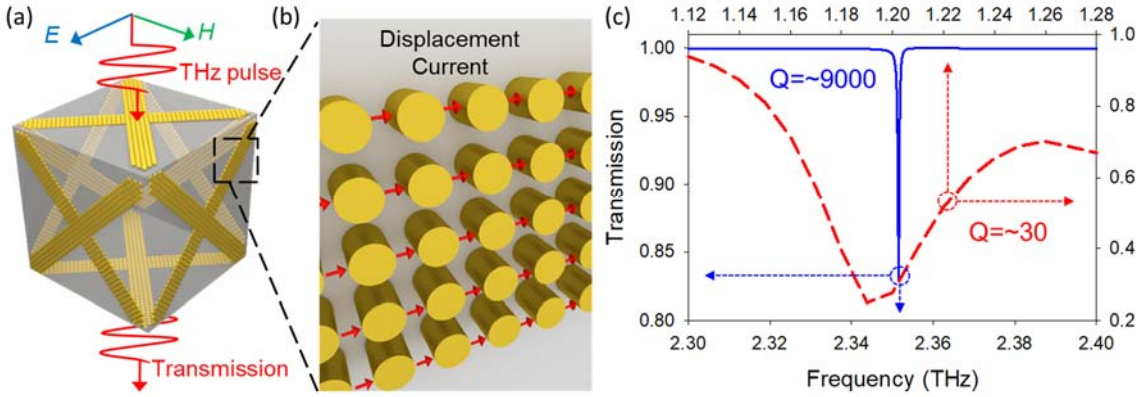

Figure 7.3 Comparison between 3D nanopillar-based MM and 3D film-based MM. (a) Illustration of the 3D nanopillar-based MM with X-shape nanopillar-based resonators patterned on each face of the 3D cubic structure. (b) An illustration of the displacement current generated within the Au nanopillars. (c) Transmission spectrum shows the resonant peaks of 3D nanopillar-based MM (blue solid line) and 3D film-based MM (red dashed line). The Q-factor of the 3D nanopillar-based MM is around 9000 while the Q-factor of the film-based MM is around 30.

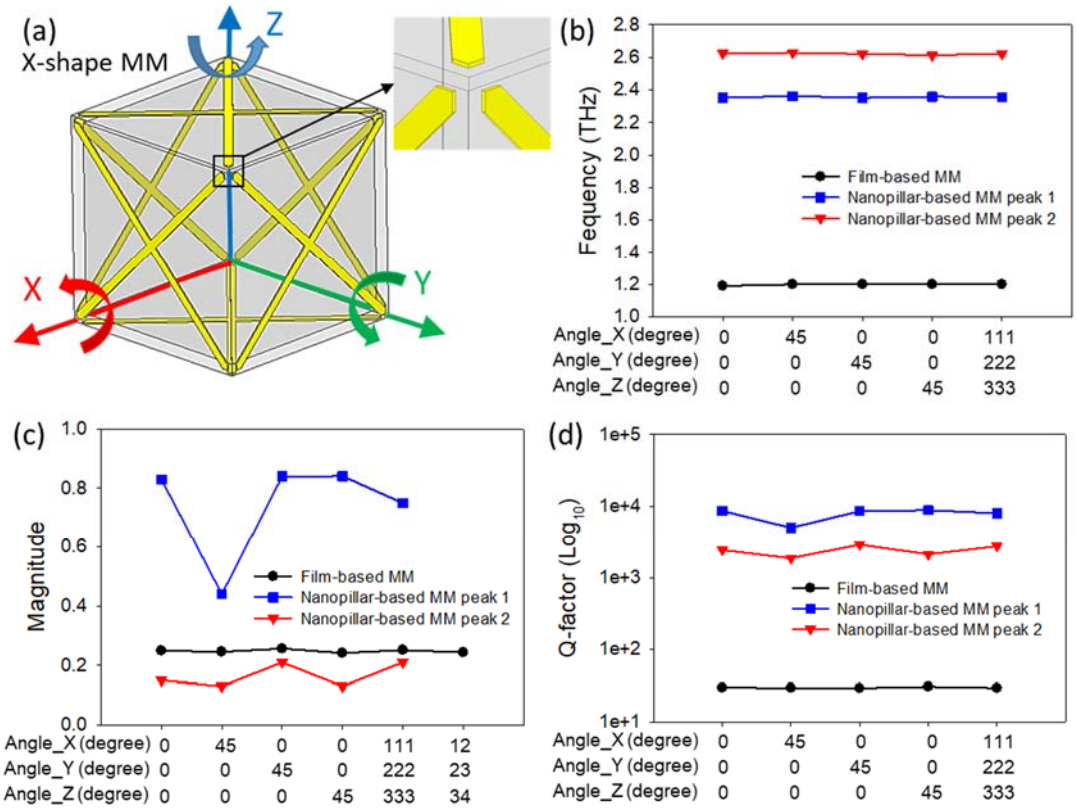

Figure 7.4 3D X-shape MM and its characters. (a) Illustration of the rotation axis of the 3D structure. (b) Resonant frequency comparison of the film-based 3D X-shape MM and the 3D nanopillar-based X-shape MM. (c) Resonant Magnitude comparison of the film-based 3D X-shape MM and the 3D nanopillar-based X-shape MM. (d) Q-factor comparison of the film-based 3D X-shape MM and the 3D nanopillar-based X-shape MM.

7.2 Frequency shifts

Frequency shift is another factor to be considered for the sensitivity and selectivity of the 3D MM sensors. Figure 7.5 illustrates the frequency shifts of the 3D MMs with the presents of materials with different permittivity. It can be concluded that when the permittivity changes from 1 to 3.9, the nanopillar-based 3D X-shape MM has a frequency shift of 1 while the film-based 3D X-shape MM only has a frequency shift of 0.4. Similarly, when the permittivity changes from 1 to 5, the nanopillar-based 3D X-shape MM has a frequency shift of 1.2 while the film-based 3D X-shape MM has a frequency shift of around 0.6. Larger frequency shifts of the nanopillar-based 3D X-shape MM makes the transmission response more sensitive to permittivity changes around the MM, leading to ultra-high sensitivity when used as a 3D sensor. The nanopillar-based 3D X-shape MM are suitable for various applications like biomedical sensors, 3D sensors, and frequency agile devices.

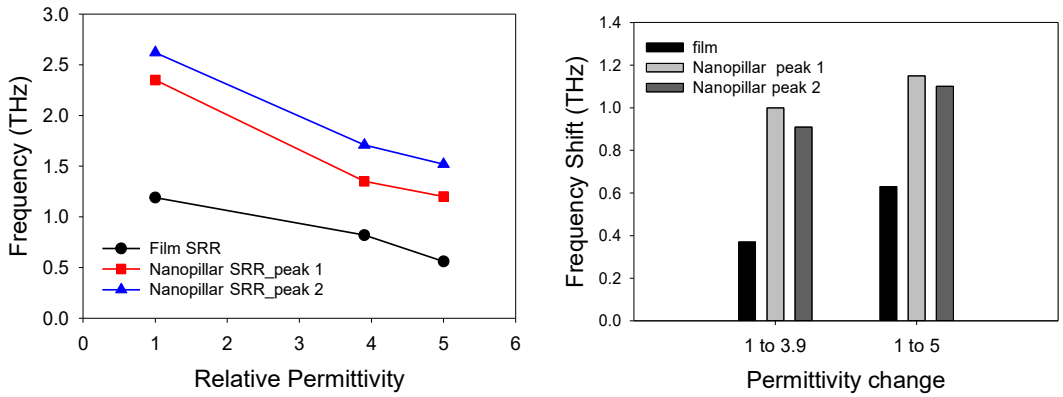

Figure 7.5 Frequency comparisons between film-based 3D X-shape MM and nanopillar-based 3D X-shape MM.

Chapter 8

Conclusion

8.1 Looking behind

In this thesis, a novel self-assembly technique – remotely controlled self-assembly using electromagnetic fields (microwave and induction energies) is presented. No physical contact is needed to trigger the assembly process, which increases the manipulative ability of the self-assembly. Folding angles of the 3D micro-scale cubic structures with different Cr thicknesses show that the self-assembly process can be easily and precisely controlled by tuning the reaction time of the electromagnetic energy and the thickness of the conducting thin film. By applying different Cr thicknesses on microstructures with multiple hinges, various folding angles can be realized simultaneously. The realization of multiple folding angles in a single structure is crucial for building complex micro-scale structures and micro-scale actuators.

High frequency magnetic field can trigger the self-assembly process by penetrating through biomaterials without harming the biomaterials. The heat is generated by eddy current within the Ni panels, limiting the heat from spreading to the environment. The PCL material used in the hinges has a low melting point of 60 ^{o}C, which further reduces the damage of heat to living tissues and organs during the self-assembly process. All these advantages of induction driven self-assembly makes it ideal candidate for biomedical applications.

To utilizing the self-assembly technique to explore advanced 3D MMs, novel THz MMs, utilizing displacement current driving its resonant frequencies, were designed, fabricated and characterized. Forming the SRRs or CRRs with metal nanopillars induces displacement current along the nanopillar array or slits, which increases stored energy. This dramatically enhances Q-factor. An ultra-high Q of more than 14000 can be achieved using nanopillar-based CRRs. Enlarged effective surface area also increases resonant frequency shifts in response to substance changes around the MMs. Significantly enlarged Q-factor and large resonant frequency shifts improve sensitivity and selectivity of the MM sensors. Therefore, the nanopillar-based MMs could be an ideal candidate for ultra-sensitive biomedical and biomolecular sensors like label-free biosensors for sensing of DNA and protein, and biomolecular detectors of hormones and antigens. It can also be applied in highly sensitive chemical and gas sensing. In addition, the nanopillar-based MMs with large frequency shifts are suitable for frequency-agile devices such as spatial light modulators and tunable optical filters.

Novel ultra-sensitive THz MMs and 3D MMs combined with remote-controlled self-assembly allows creating diverse sensors and devices for 3D optoelectronic, 3D MMs, and ultra-high sensitive biomedical sensors. These applications will not only pursuit novel sensors, micro-scale robotics and machines using advanced manufacturing techniques but also can also be used as new types of data storage, transformation and analysis for new generation of informatics technologies by patterning data storage and analysis units on the 3D self-assembled structures.

8.2 Looking ahead

The continuous study of remotely controlled self-assembly gives us more opportunities to create complex remotely controlled 3D devices for biomedical applications. More detailed *in-vivo* experiments will be needed to further test the biomedical capability of such devices and how the living tissues and organs will respond to the self-assembly process. In addition, advanced remotely controlled self-assembly technique with reversible properties will be beneficial for applications like micro-robots, micro-actuators and drug delivery systems for medical applications.

With the help of nanopillar-based THz MMs, 3D self-assembled structures can be used as ultra-sensitive 3D sensors. However, since the ultra-high Q-factors of such devices, the resonant peaks are extremely sharp, which makes it really difficult to detect the transmission spectrum of the nanopillar-based MMs. High resolution THz spectroscopy or novel THz measuring systems are required to carry ultra-high sensitive THz sensing to a new level.

Bibliography

[1] Pelesko, John A. *Self Assembly: The Science of Things that Put Themselves Together* Chapman and Hall/CRC, 2007.

[2] Aggarwal, Gagan, Qi Cheng, Michael H. Goldwasser, Ming-Yang Kao, Pablo Moisset De Espanes, and Robert T. Schweller. "Complexities for Generalized Models of Self-Assembly." *SIAM Journal on Computing*34, no. 6 (2005): 1493-1515.

[3] Campbell, Dean J., ER Freidinger, JM Hastings, and MK Querns. "Spontaneous Assembly of Soda Straws." *Journal of Chemical Education* 79, no. 2 (2002): 201.

[4] Fialkowski, Marcin, Kyle JM Bishop, Rafal Klajn, Stoyan K. Smoukov, Christopher J. Campbell, and Bartosz A. Grzybowski. *Principles and Implementations of Dissipative (Dynamic) Self-Assembly* (2006).

[5] Reif, John H., Sudheer Sahu, and Peng Yin. "Complexity of Graph Self-Assembly in Accretive Systems and Self-Destructible Systems." Springer, 2005.

[6] Whitesides, G. M. and B. Grzybowski. "Self-Assembly at all Scales." *Science (New York, N.Y.)* 295, no. 5564 (Mar 29, 2002): 2418-2421.

[7] Philp, Douglas and J. Fraser Stoddart. "Self-assembly in Natural and Unnatural Systems." *Angewandte Chemie International Edition in English* 35, no. 11 (1996): 1154-1196.

[8] Kuhn, Hans and Jürg Waser. "Molecular self-organization and the Origin of Life." *Angewandte Chemie International Edition in English* 20, no. 6-7 (1981): 500-520.

[9] Eigen, Manfred and Peter Schuster. "The Hypercycle." *Naturwissenschaften* 65, no. 1 (1978): 7-41.

[10] Lindsey, Jonathan S. "Self-assembly in Synthetic Routes to Molecular Devices. Biological Principles and Chemical Perspectives: A Review." *Cheminform* 22, no. 38 (1991).

[11] Whitesides, GM. "GM Whitesides, JP Mathias, and CT Seto, Science 254, 1312 (1991)." *Science* 254, (1991): 1312.

[12] Kugler, Peter N. and Michael T. Turvey. *Information, Natural Law, and the Self-Assembly of Rhythmic Movement* Routledge, 2015.

[13] Whitesides, G. M. and M. Boncheva. "Beyond Molecules: Self-Assembly of Mesoscopic and Macroscopic Components." *Proceedings of the National Academy of Sciences of the United States of America* 99, no. 8 (Apr 16, 2002): 4769-4774.

[14] Gibson, Daniel G., Lei Young, Ray-Yuan Chuang, J. Craig Venter, Clyde A. Hutchison III, and Hamilton O. Smith. "Enzymatic Assembly of DNA Molecules Up to several Hundred Kilobases." *Nature Methods* 6, no. 5 (2009): 343.

[15] Shappee, Benjamin J. and KZ Stanek. "A New Cepheid Distance to the Giant Spiral M101 Based on Image Subtraction of Hubble Space Telescope/Advanced Camera for Surveys Observations." *The Astrophysical Journal* 733, no. 2 (2011): 124.

[16] NASA Content Administrator, ed. (31 May 2012). "The Pinwheel Galaxy". NASA. Retrieved 4 March 2017.

[17] Comte, G., G. Monnet, and M. Rosado. "An Optical Study of the Galaxy M 101-Derivation of a Mass Model from the Kinematic of the Gas." *Astronomy and Astrophysics* 72, (1979): 73-81.

[18] Giannakopoulou-Creighton, Jean, Michel Fich, and Christine D. Wilson. "Star Formation in the Giant H II Regions of M101." *The Astrophysical Journal* 522, no. 1 (1999): 238.

[19] Dwek, Eli and Isabelle Cherchneff. "The Origin of Dust in the Early Universe: Probing the Star Formation History of Galaxies by their Dust Content." *The Astrophysical Journal* 727, no. 2 (2011): 63.

[20] Figer, Don F. *Massive Star Formation in the Galactic Center* (2008).

[21] Alberts B, Johnson A, Lewis J, Raff M, Roberts K, Walter P (2014). *Molecular Biology of the Cell* (6th ed.). Garland. p. Chapter 4: DNA, Chromosomes and Genomes.

[22] Saenger W (1984). *Principles of Nucleic Acid Structure*. New York: Springer-Verlag.

[23] Watson, JD and FHC Crick. "Molecular Structure of Nucleic Acids: A Structure for Deoxyribose Nucleic Acid." *Jama* 269, no. 15 (1993): 1966-1967.

[24] Mandelkern, Marshal, John G. Elias, Don Eden, and Donald M. Crothers. "The Dimensions of DNA in Solution." *Journal of Molecular Biology* 152, no. 1 (1981): 153-161.

[25] Gregory, SG, KF Barlow, KE McLay, R. Kaul, D. Swarbreck, A. Dunham, CE Scott, KL Howe, K. Woodfine, and CCA Spencer. "The DNA Sequence and Biological Annotation of Human Chromosome 1." *Nature*441, no. 7091 (2006): 315.

[26] Watson, James D. and Francis HC Crick. "Molecular Structure of Nucleic Acids." *Resonance* 9, no. 11 (2004): 96-98.

[27] Maiti, Motilal and Gopinatha Suresh Kumar. "Molecular Aspects on the Interaction of Protoberberine, Benzophenanthridine, and Aristolochia Group of Alkaloids with

Nucleic Acid Structures and Biological Perspectives." *Medicinal Research Reviews* 27, no. 5 (2007): 649-695.

[28] Sinden, Richard R. *DNA Structure and Function* Elsevier, 2012.

[29] Gibson, Daniel G. "Enzymatic Assembly of Overlapping DNA Fragments." In *Methods in Enzymology*. Vol. 498, 349-361: Elsevier, 2011.

[30] Cartwright, Reed A. "DNA Assembly with Gaps (Dawg): Simulating Sequence Evolution." *Bioinformatics* 21, no. Suppl_3 (2005): iii31-iii38.

[31] Leong, Timothy G., Aasiyeh M. Zarafshar, and David H. Gracias. "Three-dimensional Fabrication at Small Size Scales." *Small* 6, no. 7 (2010): 792-806.

[32] Carter, Forrest L. "Further Considerations on “molecular” Electronic Devices." *The NRL Program on Electroactive Polymers, Second Annual Report. NRL Memorandum Report* 4335, (1980): 35-52.

[33] Barker, JR. "Prospects for Molecular Electronics." *Microelectronics International* 4, no. 3 (1987): 19-24.

[34] Haarer, Dietrich. "How to Tailor Molecular Electronics Or Why is Nature Taking the ‘soft’ approach?" *Angewandte Chemie International Edition in English* 28, no. 11 (1989): 1544-1547.

[35] Haddon, R. C. and A. A. Lamola. "The Molecular Electronic Device and the Biochip Computer: Present Status." *Proceedings of the National Academy of Sciences of the United States of America* 82, no. 7 (Apr, 1985): 1874-1878.

[36] Miller, Joel S. "Molecular Materials II Part A. Molecular Electronics?" *Advanced Materials* 2, no. 8 (1990): 378-379.

[37] Elghanian, R., J. J. Storhoff, R. C. Mucic, R. L. Letsinger, and C. A. Mirkin. "Selective Colorimetric Detection of Polynucleotides Based on the Distance-Dependent Optical Properties of Gold Nanoparticles." *Science (New York, N.Y.)* 277, no. 5329 (Aug 22, 1997): 1078-1081.

[38] Mullin, John William. *Crystallization* Elsevier, 2001.

[39] Kim, Jin-Yeol, Min-Hee Kwon, Jae-Taek Kim, Sijoong Kwon, Dae-Woo Ihm, and Young-Kun Min. "Crystallization Growth and Micropatterning on Self-Assembled Conductive Polymer Nanofilms." *The Journal of Physical Chemistry C* 111, no. 30 (2007): 11252-11258.

[40] Lubelli, Barbara and Mario R. de Rooij. "NaCl Crystallization in Restoration Plasters." *Construction and Building Materials* 23, no. 5 (2009): 1736-1742.

[41] Ferreira, A., N. Faria, F. Rocha, S. Feyo De Azevedo, and A. Lopes. "Using Image Analysis to Look into the Effect of Impurity Concentration in NaCl Crystallization." *Chemical Engineering Research and Design*83, no. 4 (2005): 331-338.

[42] Van't Land, CM and BG Wienk. "Control of Particle Size in Industrial NaCl-Crystallization." In *Industrial Crystallization*, 51-60: Springer, 1976.

[43] Moore, Emily B. and Valeria Molinero. "Structural Transformation in Supercooled Water Controls the Crystallization Rate of Ice." *Nature* 479, no. 7374 (2011): 506.

[44] T. Petras, "Properties of Salt tutorial", MR. P Chemistry, (2018) Retrieved from: www.sartep.com.

[45] Lin, Keh Ying and Wen Jong Ma. "Residual Entropy of Two-Dimensional Ice on a Ruby Lattice." *Journal of Physics A: Mathematical and General* 16, no. 11 (1983): 2515.

[46] Theoulakis, P. and A. Moropoulou. "Salt Crystal Growth as Weathering Mechanism of Porous Stone on Historic Masonry." *Journal of Porous Materials* 6, no. 4 (1999): 345-358.

[47] Schaefer, Vincent J. "The Preparation of Snow Crystal replicas—VI." *Weatherwise* 9, no. 4 (1956): 132-135.

[48] Cölfen, Helmut and Stephen Mann. "Higher-order Organization by Mesoscale self-assembly and Transformation of Hybrid Nanostructures." *Angewandte Chemie International Edition* 42, no. 21 (2003): 2350-2365.

[49] Glasser, Leslie. "Lattice and Phase Transition Thermodynamics of Ionic Liquids." *Thermochimica Acta* 421, no. 1-2 (2004): 87-93.

[50] Layton, MM and Andrew Herczog. "Nucleation and Crystallization of NaNbO3 from Glasses in the Na2O-Nb2O5-SiO2 System." *Journal of the American Ceramic Society* 50, no. 7 (1967): 369-375.

[51] Gutiérrez, María C., María L. Ferrer, and Francisco del Monte. "Ice-Templated Materials: Sophisticated Structures Exhibiting Enhanced Functionalities obtained After Unidirectional Freezing and Ice-Segregation-Induced Self-Assembly." *Chemistry of Materials* 20, no. 3 (2008): 634-648.

[52] Im, Sang Hyuk and O. Ok Park. "Three-Dimensional Self-Assembly by Ice Crystallization." *Applied Physics Letters* 80, no. 22 (2002): 4133-4135.

[53] U.S. Department of Commerce, “How do snowflakes form? Get the science behind snow”, *National Oceanic and Atmospheric Administration* (2016). Retrieved from: www.noaa.gov.

[54] Erb, Randall M., Jonathan S. Sander, Roman Grisch, and André R. Studart. "Self-Shaping Composites with Programmable Bioinspired Microstructures." *Nature Communications* 4, (2013): 1712.

[55] Vander Wall, Stephen B. and Russell P. Balda. "Coadaptations of the Clark's Nutcracker and the Pinon Pine for Efficient Seed Harvest and Dispersal." *Ecological Monographs* 47, no. 1 (1977): 89-111.

[56] Tomback, Diana F. "Dispersal of Whitebark Pine Seeds by Clark's Nutcracker: A Mutualism Hypothesis." *The Journal of Animal Ecology* (1982): 451-467.

[57] Mutke, Sven, Javier Gordo, and Luis Gil. "Variability of Mediterranean Stone Pine Cone Production: Yield Loss as Response to Climate Change." *Agricultural and Forest Meteorology* 132, no. 3-4 (2005): 263-272.

[58] Benkman, Craig W. "Wind Dispersal Capacity of Pine Seeds and the Evolution of Different Seed Dispersal Modes in Pines." *Oikos* (1995): 221-224.

[59] Emons, Anne Mie C. and Bela M. Mulder. "How the Deposition of Cellulose Microfibrils Builds Cell Wall Architecture." *Trends in Plant Science* 5, no. 1 (2000): 35-40.

[60] Burgert, Ingo and Peter Fratzl. "Plants Control the Properties and Actuation of their Organs through the Orientation of Cellulose Fibrils in their Cell Walls." *Integrative and Comparative Biology* 49, no. 1 (2009): 69-79.

[61] Forterre, Yoël, Jan M. Skotheim, Jacques Dumais, and Lakshminarayanan Mahadevan. "How the Venus Flytrap Snaps." *Nature* 433, no. 7024 (2005): 421.

[62] Ionov, Leonid. "Biomimetic 3D Self-Assembling Biomicroconstructs by Spontaneous Deformation of Thin Polymer Films." *Journal of Materials Chemistry* 22, no. 37 (2012): 19366-19375.

[63] Lang, Robert J. *Origami Design Secrets: Mathematical Methods for an Ancient Art* AK Peters/CRC Press, 2011.

[64] Beech, Rick. *Origami: The Complete Guide to the Art of Paperfolding* Lorenz Books, 2004.

[65] Miura, Koryo. "A Note on Intrinsic Geometry of Origami." *Research of Pattern Formation* (1989): 91-102.

[66] Lang, Robert J. "Origami: Complexity in Creases (again)." *Engineering and Science* 67, no. 1 (2004): 5-19.

[67] Kawasaki, Toshikazu. "On the Relation between Mountain-Creases and Valley-Creases of a Flat Origami."1991.

[68] Lang, Robert J. *Origami Design Secrets: Mathematical Methods for an Ancient Art* AK Peters/CRC Press, 2011.

[69] Filipiak, David J., Anum Azam, Timothy G. Leong, and David H. Gracias. "Hierarchical Self-Assembly of Complex Polyhedral Microcontainers." *Journal of Micromechanics and Microengineering* 19, no. 7 (2009): 075012.

[70] Azam, Anum, Timothy G. Leong, Aasiyeh M. Zarafshar, and David H. Gracias. "Compactness Determines the Success of Cube and Octahedron Self-Assembly." *PloS One* 4, no. 2 (2009): e4451.

[71] Grzybowski, Bartosz A., Christopher E. Wilmer, Jiwon Kim, Kevin P. Browne, and Kyle JM Bishop. "Self-Assembly: From Crystals to Cells." *Soft Matter* 5, no. 6 (2009): 1110-1128.

[72] Jeong, Kwang-Un, Ji-Hyun Jang, Dae-Yoon Kim, Changwoon Nah, Joong Hee Lee, Myong-Hoon Lee, Hao-Jan Sun, Chien-Lung Wang, Stephen ZD Cheng, and Edwin L. Thomas. "Three-Dimensional Actuators Transformed from the Programmed Two-Dimensional Structures Via Bending, Twisting and Folding Mechanisms." *Journal of Materials Chemistry* 21, no. 19 (2011): 6824-6830.

[73] Stoychev, Georgi, Nikolay Puretskiy, and Leonid Ionov. "Self-Folding all-Polymer Thermoresponsive Microcapsules." *Soft Matter* 7, no. 7 (2011): 3277-3279.

[74] Bassik, Noy, Beza T. Abebe, Kate E. Laflin, and David H. Gracias. "Photolithographically Patterned Smart Hydrogel Based Bilayer Actuators." *Polymer* 51, no. 26 (2010): 6093-6098.

[75] Felton, Samuel M., Michael T. Tolley, ByungHyun Shin, Cagdas D. Onal, Erik D. Demaine, Daniela Rus, and Robert J. Wood. "Self-Folding with Shape Memory Composites." *Soft Matter* 9, no. 32 (2013): 7688-7694.

[76] Fernandes, Rohan and David H. Gracias. "Self-Folding Polymeric Containers for Encapsulation and Delivery of Drugs." *Advanced Drug Delivery Reviews* 64, no. 14 (2012): 1579-1589.

[77] Stoychev, Georgi, Sébastien Turcaud, John WC Dunlop, and Leonid Ionov. "Hierarchical multi-step Folding of Polymer Bilayers." *Advanced Functional Materials* 23, no. 18 (2013): 2295-2300.

[78] Pickett, G. T. "Self-Folding Origami Membranes." *EPL (Europhysics Letters)* 78, no. 4 (2007): 48003.

[79] Smela, E., O. Inganas, and I. Lundstrom. "Controlled Folding of Micrometer-Size Structures." *Science (New York, N.Y.)* 268, no. 5218 (Jun 23, 1995): 1735-1738.

[80] Jeong, Kwang-Un, Ji-Hyun Jang, Dae-Yoon Kim, Changwoon Nah, Joong Hee Lee, Myong-Hoon Lee, Hao-Jan Sun, Chien-Lung Wang, Stephen ZD Cheng, and Edwin L. Thomas. "Three-Dimensional Actuators Transformed from the Programmed Two-Dimensional Structures Via Bending, Twisting and Folding Mechanisms." *Journal of Materials Chemistry* 21, no. 19 (2011): 6824-6830.

[81] Hawkes, E., B. An, N. M. Benbernou, H. Tanaka, S. Kim, E. D. Demaine, D. Rus, and R. J. Wood. "Programmable Matter by Folding." *Proceedings of the National Academy of Sciences of the United States of America* 107, no. 28 (Jul 13, 2010): 12441-12445.

[82] Cho, Jeong-Hyun, Teena James, and David H. Gracias. "Curving Nanostructures using Extrinsic Stress." *Advanced Materials* 22, no. 21 (2010): 2320-2324.

[83] Tyagi, Pawan, Noy Bassik, Timothy G. Leong, Jeong-Hyun Cho, Bryan R. Benson, and David H. Gracias. "Self-Assembly Based on chromium/copper Bilayers." *Journal of Microelectromechanical Systems* 18, no. 4 (2009): 784-791.

[84] Cho, Jeong-Hyun, Dibakar Datta, Si-Young Park, Vivek B. Shenoy, and David H. Gracias. "Plastic Deformation Drives Wrinkling, Saddling, and Wedging of Annular Bilayer Nanostructures." *Nano Letters* 10, no. 12 (2010): 5098-5102.

[85] Cho, Jeong-Hyun, Anum Azam, and David H. Gracias. "Three Dimensional Nanofabrication using Surface Forces." *Langmuir* 26, no. 21 (2010): 16534-16539.

[86] Gracias, David H. and Jeong-Hyun Cho. *Self-Assembly of Lithographically Patterned Polyhedral Nanostructures and Formation of Curving Nanostructures* (2012).

[87] Dai, Chunhui, Daeha Joung, and Jeong-Hyun Cho. "Plasma Triggered Grain Coalescence for Self-Assembly of 3D Nanostructures." *Nano-Micro Letters* 9, no. 3 (2017): 27.

[88] Shenoy, Vivek B. and David H. Gracias. "Self-Folding Thin-Film Materials: From Nanopolyhedra to Graphene Origami." *MRS Bulletin* 37, no. 9 (2012): 847-854.

[89] Cho, Jeong-Hyun, Michael D. Keung, Niels Verellen, Liesbet Lagae, Victor V. Moshchalkov, Pol Van Dorpe, and David H. Gracias. "Nanoscale Origami for 3D Optics." *Small* 7, no. 14 (2011): 1943-1948.

[90] Akiyama, Terunobu, Dominique Collard, and Hiroyuki Fujita. "Scratch Drive Actuator with Mechanical Links for Self-Assembly of Three-Dimensional MEMS." *Journal of Microelectromechanical Systems* 6, no. 1 (1997): 10-17.

[91] Srinivasan, Uthara, Michael A. Helmbrecht, Christian Rembe, Richard S. Muller, and Roger T. Howe. "Fluidic Self-Assembly of Micromirrors Onto Microactuators using Capillary Forces." *IEEE Journal of Selected Topics in Quantum Electronics* 8, no. 1 (2002): 4-11.

[92] Fang, Jiandong, Kerwin Wang, and Karl F. Bohringer. "Self-Assembly of PZT Actuators for Micropumps with High Process Repeatability." *Journal of Microelectromechanical Systems* 15, no. 4 (2006): 871-878.

[93] Rubenstein, M., A. Cornejo, and R. Nagpal. "Robotics. Programmable Self-Assembly in a Thousand-Robot Swarm." *Science (New York, N.Y.)* 345, no. 6198 (Aug 15, 2014): 795-799.

[94] Jones, Chris and Maja J. Mataric. "From Local to Global Behavior in Intelligent Self-Assembly."IEEE, 2003.

[95] Emerich, Dwaine F. and Christopher G. Thanos. "Nanotechnology and Medicine." *Expert Opinion on Biological Therapy* 3, no. 4 (2003): 655-663.

[96] Liu, Ying, Jan Genzer, and Michael D. Dickey. "“2D Or Not 2D”: Shape-Programming Polymer Sheets." *Progress in Polymer Science* 52, (2016): 79-106.

[97] Ionov, Leonid. "Soft Microorigami: Self-Folding Polymer Films." *Soft Matter* 7, no. 15 (2011): 6786-6791.

[98] Gracias, David H. "Stimuli Responsive Self-Folding using Thin Polymer Films." *Current Opinion in Chemical Engineering* 2, no. 1 (2013): 112-119.

[99] Ionov, Leonid. "3D Microfabrication using Stimuli-Responsive Self-Folding Polymer Films." *Polymer Reviews* 53, no. 1 (2013): 92-107.

[100] Stoychev, Georgi, Svetlana Zakharchenko, Sébastien Turcaud, John WC Dunlop, and Leonid Ionov. "Shape-Programmed Folding of Stimuli-Responsive Polymer Bilayers." *ACS Nano* 6, no. 5 (2012): 3925-3934.

[101] Martinez, Ramses V., Carina R. Fish, Xin Chen, and George M. Whitesides. "Elastomeric Origami: Programmable paper-elastomer Composites as Pneumatic Actuators." *Advanced Functional Materials* 22, no. 7 (2012): 1376-1384.

[102] Lu, Yen-Wen and Chang-Jin Kim. "Microhand for Biological Applications." *Applied Physics Letters* 89, no. 16 (2006): 164101.

[103] Kusuda, Shinya, Satoshi Sawano, and Satoshi Konishi. "Fluid-Resistive Bending Sensor having Perfect Compatibility with Flexible Pneumatic Balloon Actuator."IEEE, 2007.

[104] Tu, Hongen, Hanqing Jiang, Hongyu Yu, and Yong Xu. "Hybrid Silicon-Polymer Platform for Self-Locking and Self-Deploying Origami." *Applied Physics Letters* 103, no. 24 (2013): 241902.

[105] Liu, Yang, Makoto Takafuji, Hirotaka Ihara, Meifang Zhu, Mingshan Yang, Kai Gu, and Wenli Guo. "Programmable Responsive Shaping Behavior Induced by Visible Multi-Dimensional Gradients of Magnetic Nanoparticles." *Soft Matter* 8, no. 12 (2012): 3295-3299.

[106] Boncheva, Mila, Stefan A. Andreev, L. Mahadevan, Adam Winkleman, David R. Reichman, Mara G. Prentiss, Sue Whitesides, and George M. Whitesides. "Magnetic Self-Assembly of Three-Dimensional Surfaces from Planar Sheets." *Proceedings of the National Academy of Sciences* 102, no. 11 (2005): 3924-3929.

[107] In, Hyun Jin, Hyungwoo Lee, Anthony J. Nichol, Sang-Gook Kim, and George Barbastathis. "Carbon nanotube-based Magnetic Actuation of Origami Membranes." *Journal of Vacuum Science & Technology B: Microelectronics and Nanometer Structures Processing, Measurement, and Phenomena* 26, no. 6 (2008): 2509-2512.

[108] Iwase, Eiji and Isao Shimoyama. "Multistep Sequential Batch Assembly of Three-Dimensional Ferromagnetic Microstructures with Elastic Hinges." *Journal of Microelectromechanical Systems* 14, no. 6 (2005): 1265-1271.

[109] Yi, Yong Wuk and Chang Liu. "Magnetic Actuation of Hinged Microstructures." *Journal of Microelectromechanical Systems* 8, no. 1 (1999): 10-17.

[110] Ahmed, S., Z. Ounaies, and M. Frecker. "Investigating the Performance and Properties of Dielectric Elastomer Actuators as a Potential Means to Actuate Origami Structures." *Smart Materials and Structures*23, no. 9 (2014): 094003.

[111] Lee, Howon, Chunguang Xia, and Nicholas X. Fang. "First Jump of Microgel; Actuation Speed Enhancement by Elastic Instability." *Soft Matter* 6, no. 18 (2010): 4342-4345.

[112] Ma, Ying, Yuanyuan Zhang, Baisheng Wu, Weipeng Sun, Zhengguang Li, and Junqi Sun. "Polyelectrolyte Multilayer Films for Building Energetic Walking Devices." *Angewandte Chemie* 123, no. 28 (2011): 6378-6381.

[113] de Leon, Al, Andrew C. Barnes, Patrick Thomas, Johnathan O'Donnell, Christian A. Zorman, and Rigoberto C. Advincula. "Transfer Printing of Self-Folding polymer–metal Bilayer Particles." *ACS Applied Materials & Interfaces* 6, no. 24 (2014): 22695-22700.

[114] Ma, Chunxin, Tiefeng Li, Qian Zhao, Xuxu Yang, Jingjun Wu, Yingwu Luo, and Tao Xie. "Supramolecular Lego Assembly Towards Three-Dimensional Multi-Responsive Hydrogels." *Advanced Materials* 26, no. 32 (2014): 5665-5669.

[115] Peppas, Nicholas A., J. Zach Hilt, Ali Khademhosseini, and Robert Langer. "Hydrogels in Biology and Medicine: From Molecular Principles to Bionanotechnology." *Advanced Materials* 18, no. 11 (2006): 1345-1360.

[116] Brannon-Peppas, Lisa and Nikolaos A. Peppas. "Equilibrium Swelling Behavior of pH-Sensitive Hydrogels." *Chemical Engineering Science* 46, no. 3 (1991): 715-722.

[117] Ahn, Suk-kyun, Rajeswari M. Kasi, Seong-Cheol Kim, Nitin Sharma, and Yuxiang Zhou. "Stimuli-Responsive Polymer Gels." *Soft Matter* 4, no. 6 (2008): 1151-1157.

[118] Luo, JK, R. Huang, JH He, Yong Qing Fu, AJ Flewitt, SM Spearing, NA Fleck, and WI Milne. "Modelling and Fabrication of Low Operation Temperature Microcages with a polymer/metal/DLC Trilayer Structure." *Sensors and Actuators A: Physical* 132, no. 1 (2006): 346-353.

[119] Luo, JK, JH He, Yong Qing Fu, AJ Flewitt, SM Spearing, NA Fleck, and WI Milne. "Fabrication and Characterization of Diamond-Like carbon/Ni Bimorph Normally Closed Microcages." *Journal of Micromechanics and Microengineering* 15, no. 8 (2005): 1406.

[120] Malachowski, Kate, Joyce Breger, Hye Rin Kwag, Martha O. Wang, John P. Fisher, Florin M. Selaru, and David H. Gracias. "Stimuli-Responsive Theragrippers for Chemomechanical Controlled Release." *Angewandte Chemie International Edition* 53, no. 31 (2014): 8045-8049.

[121] Fusco, Stefano, Mahmut Selman Sakar, Stephen Kennedy, Christian Peters, Rocco Bottani, Fabian Starsich, Angelo Mao, Georgios A. Sotiriou, Salvador Pané, and Sotiris E. Pratsinis. "An Integrated Microrobotic Platform for on-demand, Targeted Therapeutic Interventions." *Advanced Materials* 26, no. 6 (2014): 952-957.

[122] Leong, Timothy G., Paul A. Lester, Travis L. Koh, Emma K. Call, and David H. Gracias. "Surface Tension-Driven Self-Folding Polyhedra." *Langmuir* 23, no. 17 (2007): 8747-8751.

[123] Cho, Jeong-Hyun, Anum Azam, and David H. Gracias. "Three Dimensional Nanofabrication using Surface Forces." *Langmuir* 26, no. 21 (2010): 16534-16539.

[124] Zhang, Lidong, Haoran Liang, Jolly Jacob, and Panče Naumov. "Photogated Humidity-Driven Motility." *Nature Communications* 6, (2015): 7429.

[125] Ikeda, Tomiki, Makoto Nakano, Yanlei Yu, Osamu Tsutsumi, and Akihiko Kanazawa. "Anisotropic Bending and Unbending Behavior of Azobenzene liquid-crystalline Gels by Light Exposure." *Advanced Materials*15, no. 3 (2003): 201-205.

[126] Lendlein, Andreas, Hongyan Jiang, Oliver Jünger, and Robert Langer. "Light-Induced Shape-Memory Polymers." *Nature* 434, no. 7035 (2005): 879.

[127] Jiang, HY, Steffen Kelch, and Andreas Lendlein. "Polymers Move in Response to Light." *Advanced Materials* 18, no. 11 (2006): 1471-1475.

[128] Lendlein, A. and R. Langer. "Biodegradable, Elastic Shape-Memory Polymers for Potential Biomedical Applications." *Science (New York, N.Y.)* 296, no. 5573 (May 31, 2002): 1673-1676.

[129] Behl, Marc, Muhammad Yasar Razzaq, and Andreas Lendlein. "Multifunctional shape-memory Polymers." *Advanced Materials* 22, no. 31 (2010): 3388-3410.

[130] Lendlein, Andreas and Steffen Kelch. "Shape-memory Polymers." *Angewandte Chemie International Edition* 41, no. 12 (2002): 2034-2057.

[131] Bassik, Noy, George M. Stern, and David H. Gracias. "Microassembly Based on Hands Free Origami with Bidirectional Curvature." *Applied Physics Letters* 95, no. 9 (2009): 091901.

[132] Leong, Timothy G., Bryan R. Benson, Emma K. Call, and David H. Gracias. "Thin Film Stress Driven self-folding of Microstructured Containers." *Small* 4, no. 10 (2008): 1605-1609.

[133] Leong, Timothy G., Christina L. Randall, Bryan R. Benson, Aasiyeh M. Zarafshar, and David H. Gracias. "Self-Loading Lithographically Structured Microcontainers: 3D Patterned, Mobile Microwells." *Lab on a Chip* 8, no. 10 (2008): 1621-1624.

[134] Mei, Yongfeng, Dominic J. Thurmer, Christoph Deneke, Suwit Kiravittaya, Yuan-Fu Chen, Armin Dadgar, Frank Bertram, Barbara Bastek, Alois Krost, and Jürgen Christen. "Fabrication, Self-Assembly, and Properties of Ultrathin AlN/GaN Porous Crystalline Nanomembranes: Tubes, Spirals, and Curved Sheets." *Acs Nano* 3, no. 7 (2009): 1663-1668.

[135] Schmidt, Oliver G. and Karl Eberl. "Nanotechnology: Thin Solid Films Roll Up into Nanotubes." *Nature* 410, no. 6825 (2001): 168.

[136] Prinz, V. Ya. "Three-Dimensional Self-Shaping Nanostructures Based on Free Stressed Heterofilms." *Russian Physics Journal* 46, no. 6 (2003): 568-576.

[137] Randhawa, Jatinder S., Michael D. Keung, Pawan Tyagi, and David H. Gracias. "Reversible Actuation of Microstructures by Surface-Chemical Modification of Thin-Film Bilayers." *Advanced Materials* 22, no. 3 (2010): 407-410.

[138] Ebefors, Thorbjörn, Edvard Kälvesten, and Göran Stemme. "Dynamic Actuation of Polyimide V-Groove Joints by Electrical Heating." *Sensors and Actuators A: Physical* 67, no. 1-3 (1998): 199-204.

[139] Suzuki, Kenji, Hideaki Yamada, Hirofumi Miura, and Hideaki Takanobu. "Self-Assembly of Three Dimensional Micro Mechanisms using Thermal Shrinkage of Polyimide." *Microsystem Technologies* 13, no. 8-10 (2007): 1047-1053.

[140] Feinberg, Adam W., Alex Feigel, Sergey S. Shevkoplyas, Sean Sheehy, George M. Whitesides, and Kevin Kit Parker. "Muscular Thin Films for Building Actuators and Powering Devices." *Science* 317, no. 5843 (2007): 1366-1370.

[141] Xi, Jianzhong, Jacob J. Schmidt, and Carlo D. Montemagno. "Self-Assembled Microdevices Driven by Muscle." *Nature Materials* 4, no. 2 (2005): 180.

[142] Hartgerink, J. D., E. Beniash, and S. I. Stupp. "Self-Assembly and Mineralization of Peptide-Amphiphile Nanofibers." *Science (New York, N.Y.)* 294, no. 5547 (Nov 23, 2001): 1684-1688.

[143] Aggeli, Amalia, Mark Bell, Lisa M. Carrick, Colin WG Fishwick, Richard Harding, Peter J. Mawer, Sheena E. Radford, Andrew E. Strong, and Neville Boden. "PH as a Trigger of Peptide β-Sheet Self-Assembly and Reversible Switching between Nematic and Isotropic Phases." *Journal of the American Chemical Society* 125, no. 32 (2003): 9619-9628.

[144] Jayawarna, Vineetha, Murtza Ali, Thomas A. Jowitt, Aline F. Miller, Alberto Saiani, Julie E. Gough, and Rein V. Ulijn. "Nanostructured Hydrogels for three-dimensional Cell Culture through self-assembly of fluorenylmethoxycarbonyl-dipeptides." *Advanced Materials* 18, no. 5 (2006): 611-614.

[145] Bilia, A., V. Carelli, Giacomo Di Colo, and E. Nannipieri. "In Vitro Evaluation of a pH-Sensitive Hydrogel for Control of GI Drug Delivery from Silicone-Based Matrices." *International Journal of Pharmaceutics* 130, no. 1 (1996): 83-92.

[146] Jager, E. W., O. Inganas, and I. Lundstrom. "Microrobots for Micrometer-Size Objects in Aqueous Media: Potential Tools for Single-Cell Manipulation." *Science (New York, N.Y.)* 288, no. 5475 (Jun 30, 2000): 2335-2338.

[147] Palleau, Etienne, Daniel Morales, Michael D. Dickey, and Orlin D. Velev. "Reversible Patterning and Actuation of Hydrogels by Electrically Assisted Ionoprinting." *Nature Communications* 4, (2013): 2257.

[148] Ambrosy, A. and K. Holdik. "Piezoelectric PVDF Films as Ultrasonic Transducers." *Journal of Physics E: Scientific Instruments* 17, no. 10 (1984): 856.

[149] Bassik, Noy, Alla Brafman, Aasiyeh M. Zarafshar, Mustapha Jamal, Delgermaa Luvsanjav, Florin M. Selaru, and David H. Gracias. "Enzymatically Triggered Actuation of Miniaturized Tools." *Journal of the American Chemical Society* 132, no. 46 (2010): 16314-16317.

[150] Kotov, NA. "Layer-by-Layer Self-Assembly: The Contribution of Hydrophobic Interactions." *Nanostructured Materials* 12, no. 5-8 (1999): 789-796.

[151] Ionov, Leonid. "Biomimetic hydrogel-based Actuating Systems." *Advanced Functional Materials* 23, no. 36 (2013): 4555-4570.

[152] Ionov, Leonid. "Hydrogel-Based Actuators: Possibilities and Limitations." *Materials Today* 17, no. 10 (2014): 494-503.

[153] S. Janbaz, R. Hedayati, A. Zadpoor, "Programming the shape-shifting of flat soft matter: from self-rolling/self-twisting materials to self-folding origami. " *Materials Horizons*. 3, 536-547 (2016).

[154] D. H. Gracias, V. Kavthekar, J. C. Love, K. E. Paul, G. M. Whitesides, "Fabrication of micrometer-scale, patterned polyhedra by self-assembly. " *Adv Mater.* 14, 235 (2002).

[155] D. B. Burckel, S. Campione, P. S. Davids, M. B. Sinclair, "Three dimensional metafilms with dual channel unit cells." *Appl. Phys. Lett.* 110, 143107 (2017).

[156] D. Joung, T. Gu, J. Cho, "Tunable Optical Transparency in Self-Assembled Three-Dimensional Polyhedral Graphene Oxide." *ACS Nano.* 10, 9586-9594 (2016).

[157] Ozbas, Bulent, Juliana Kretsinger, Karthikan Rajagopal, Joel P. Schneider, and Darrin J. Pochan. "Salt-Triggered Peptide Folding and Consequent Self-Assembly into Hydrogels with Tunable Modulus." *Macromolecules* 37, no. 19 (2004): 7331-7337.

[158] J. Guan, H. He, D. J. Hansford, L. J. Lee, "Self-folding of three-dimensional hydrogel microstructures." *The Journal of Physical Chemistry B*. 109, 23134-23137 (2005).

[159] Luchnikov, Valeriy, Olexander Sydorenko, and Manfred Stamm. "Self-rolled Polymer and Composite polymer/metal micro-and Nanotubes with Patterned Inner Walls." *Advanced Materials* 17, no. 9 (2005): 1177-1182.

[160] Guan, Jingjiao, Hongyan He, L. James Lee, and Derek J. Hansford. "Fabrication of Particulate Reservoir-Containing, Capsulelike, and Self-Folding Polymer Microstructures for Drug Delivery." *Small* 3, no. 3 (2007): 412-418.

[161] Liu, Chao, Joseph Schauff, Daeha Joung, and Jeong-Hyun Cho. "Remotely Controlled Microscale 3D Self-Assembly using Microwave Energy." *Advanced Materials Technologies* 2, no. 8 (2017): 1700035.

[162] Xu, Weinan, Zhao Qin, Chun-Teh Chen, Hye Rin Kwag, Qinli Ma, Anjishnu Sarkar, Markus J. Buehler, and David H. Gracias. "Ultrathin Thermoresponsive Self-Folding 3D Graphene." *Science Advances* 3, no. 10 (2017): e1701084.

[163] Mu, Jiuke, Chengyi Hou, Hongzhi Wang, Yaogang Li, Qinghong Zhang, and Meifang Zhu. "Origami-Inspired Active Graphene-Based Paper for Programmable Instant Self-Folding Walking Devices." *Science Advances* 1, no. 10 (2015): e1500533.

[164] Liu, Ying, Julie K. Boyles, Jan Genzer, and Michael D. Dickey. "Self-Folding of Polymer Sheets using Local Light Absorption." *Soft Matter* 8, no. 6 (2012): 1764-1769.

[165] Liu, Ying, Brandi Shaw, Michael D. Dickey, and Jan Genzer. "Sequential Self-Folding of Polymer Sheets." *Science Advances* 3, no. 3 (2017): e1602417.

[166] Malachowski, Kate, Mustapha Jamal, Qianru Jin, Beril Polat, Christopher J. Morris, and David H. Gracias. "Self-Folding Single Cell Grippers." *Nano Letters* 14, no. 7 (2014): 4164-4170.

[167] Anacleto, Patricia, PM Mendes, E. Gultepe, and DH Gracias. "3D Small Antenna for Energy Harvesting Applications on Implantable Micro-Devices."IEEE, 2012.

[168] Monnard, Pierre-Alain and David W. Deamer. "Membrane self-assembly Processes: Steps Toward the First Cellular Life." *The Anatomical Record: An Official Publication of the American Association of Anatomists* 268, no. 3 (2002): 196-207.

[169] Kalinin, Yevgeniy V., Jatinder S. Randhawa, and David H. Gracias. "Three-Dimensional Chemical Patterns for Cellular Self-Organization." *Angewandte Chemie International Edition* 50, no. 11 (2011): 2549-2553.

[170] Fochi, Federica, Paola Jacopozzi, Elina Wegelius, Kari Rissanen, Pietro Cozzini, Elena Marastoni, Emilia Fisicaro, Paola Manini, Roel Fokkens, and Enrico Dalcanale. "Self-Assembly and Anion Encapsulation Properties of Cavitand-Based Coordination Cages." *Journal of the American Chemical Society* 123, no. 31 (2001): 7539-7552.

[171] Chan, Barbara P., TY Hui, CW Yeung, J. Li, I. Mo, and GCF Chan. "Self-Assembled collagen–human Mesenchymal Stem Cell Microspheres for Regenerative Medicine." *Biomaterials* 28, no. 31 (2007): 4652-4666.

[172] Randall, Christina L., Timothy G. Leong, Noy Bassik, and David H. Gracias. "3D Lithographically Fabricated Nanoliter Containers for Drug Delivery." *Advanced Drug Delivery Reviews* 59, no. 15 (2007): 1547-1561.

[173] Raof, Nurazhani Abdul, Michael R. Padgen, Alison R. Gracias, Magnus Bergkvist, and Yubing Xie. "One-Dimensional Self-Assembly of Mouse Embryonic Stem Cells using an Array of Hydrogel Microstrands." *Biomaterials* 32, no. 20 (2011): 4498-4505.

[174] Cui, Wei, Junbai Li, and Gero Decher. "Self-Assembled Smart Nanocarriers for Targeted Drug Delivery." *Advanced Materials* 28, no. 6 (2016): 1302-1311.

[175] Semiatin, SL. *Elements of Induction Heating: Design, Control, and Applications* ASM International, 1988.

[176] Fink, Donald G. and AD Mcllenzie. "Electronics Engineers Handbook. McGraw-Hill." *New York* (1975): 24-14.

[177] Davies, John and Peter Simpson. *Induction Heating Handbook* McGraw-Hill Companies, 1979.

[178] Crew, Henry. *General Physics: An Elementary Text-Book for Colleges* Macmillan, 1908.

[179] Sadiku, Matthew NO. *Elements of Electromagnetics* Oxford University Press, 2014.

[180] Harrington, Roger F. *Introduction to Electromagnetic Engineering* Courier Corporation, 2003.

[181] Fiorillo, Fausto. *Characterization and Measurement of Magnetic Materials* Academic Press, 2004.

[182] Halliday, David, Robert Resnick, and Jearl Walker. *Fundamentals of Physics,* John Wiley & Sons, 2010.

[183] Yang, Po-Kang, Zong-Hong Lin, Ken C. Pradel, Long Lin, Xiuhan Li, Xiaonan Wen, Jr-Hau He, and Zhong Lin Wang. "Paper-Based Origami Triboelectric Nanogenerators and Self-Powered Pressure Sensors." *ACS Nano* 9, no. 1 (2015): 901-907.

[184] Cho, JH, S. Hu, and DH Gracias. "Self-Assembly of Orthogonal Three-Axis Sensors." *Applied Physics Letters* 93, no. 4 (2008): 043505.

[185] Shin, ByungHyun, Samuel M. Felton, Michael T. Tolley, and Robert J. Wood. "Self-Assembling Sensors for Printable Machines."IEEE, 2014.

[186] Azam, Anum, Kate E. Laflin, Mustapha Jamal, Rohan Fernandes, and David H. Gracias. "Self-Folding Micropatterned Polymeric Containers." *Biomedical Microdevices* 13, no. 1 (2011): 51-58.

[187] Miyashita, Shuhei, Steven Guitron, Marvin Ludersdorfer, Cynthia R. Sung, and Daniela Rus. "An Untethered Miniature Origami Robot that Self-Folds, Walks, Swims, and Degrades."IEEE, 2015.

[188] Sung, Cynthia, Rhea Lin, Shuhei Miyashita, Sehyuk Yim, Sangbae Kim, and Daniela Rus. "Self-Folded Soft Robotic Structures with Controllable Joints."IEEE, 2017.

[189] Solovev, Alexander A., Samuel Sanchez, Martin Pumera, Yong Feng Mei, and Oliver G. Schmidt. "Magnetic Control of Tubular Catalytic Microbots for the Transport, Assembly, and Delivery of micro-objects." *Advanced Functional Materials* 20, no. 15 (2010): 2430-2435.

[190] Felton, Samuel, Michael Tolley, Erik Demaine, Daniela Rus, and Robert Wood. "A Method for Building Self-Folding Machines." *Science* 345, no. 6197 (2014): 644-646.

[191] Lv, Cheng, Deepakshyam Krishnaraju, Goran Konjevod, Hongyu Yu, and Hanqing Jiang. "Origami Based Mechanical Metamaterials." *Scientific Reports* 4, (2014): 5979.

[192] Silverberg, J. L., A. A. Evans, L. McLeod, R. C. Hayward, T. Hull, C. D. Santangelo, and I. Cohen. "Applied Origami using Origami Design Principles to Fold

Reprogrammable Mechanical Metamaterials." *Science (New York, N.Y.)* 345, no. 6197 (Aug 8, 2014): 647-650.

[193] Wu, Pin Chieh, Wei-Lun Hsu, Wei Ting Chen, Yao-Wei Huang, Chun Yen Liao, Ai Qun Liu, Nikolay I. Zheludev, Greg Sun, and Din Ping Tsai. "Plasmon Coupling in Vertical Split-Ring Resonator Metamolecules." *Scientific Reports* 5, (2015): 9726.

[194] Du, Y., E. Lo, S. Ali, and A. Khademhosseini. "Directed Assembly of Cell-Laden Microgels for Fabrication of 3D Tissue Constructs." *Proceedings of the National Academy of Sciences of the United States of America* 105, no. 28 (Jul 15, 2008): 9522-9527.

[195] He, Hongyan, Jingjiao Guan, and James L. Lee. "An Oral Delivery Device Based on Self-Folding Hydrogels." *Journal of Controlled Release* 110, no. 2 (2006): 339-346.

[196] Jakab, Karoly, Cyrille Norotte, Francoise Marga, Keith Murphy, Gordana Vunjak-Novakovic, and Gabor Forgacs. "Tissue Engineering by Self-Assembly and Bio-Printing of Living Cells." *Biofabrication* 2, no. 2 (2010): 022001.

[197] Erkeçoğlu, Sera, Ali Demir Sezer, and Seyda Bucak. "Smart Delivery Systems with Shape Memory and Self-Folding Polymers." In *Smart Drug Delivery System*: InTech, 2016.

[198] Gimi, Barjor, Timothy Leong, Zhiyong Gu, Michael Yang, Dmitri Artemov, Zaver M. Bhujwalla, and David H. Gracias. "Self-Assembled Three Dimensional Radio Frequency (RF) Shielded Containers for Cell Encapsulation." *Biomedical Microdevices* 7, no. 4 (2005): 341-345.

[199] IEEE Standards Coordinating Committee, 28. "IEEE Standard for Safety Levels with Respect to Human Exposure to Radio Frequency Electromagnetic Fields, 3kHz to 300GHz." *Ieee c95.1-1991* (1992).

[200] Haimbaugh, Richard E. *Practical Induction Heat Treating* ASM international, 2001.

[201] Zillipoper, Mini induction heater IRFP460 5 MHz, *4HV.ORG forum high voltage*, 2012. Retrieved from: http://4hv.org/e107_plugins/forum/forum_viewtopic.php?142264

[202] Kshetrimayum, Rakhesh S. "A Brief Intro to Metamaterials." *IEEE Potentials* 23, no. 5 (2004): 44-46.

[203] Liu, Yongmin and Xiang Zhang. "Metamaterials: A New Frontier of Science and Technology." *Chemical Society Reviews* 40, no. 5 (2011): 2494-2507.

[204] Shelby, RA, DR Smith, SC Nemat-Nasser, and Sheldon Schultz. "Microwave Transmission through a Two-Dimensional, Isotropic, Left-Handed Metamaterial." *Applied Physics Letters* 78, no. 4 (2001): 489-491.

[205] Jiang, Zhi Hao, Lan Lin, Ding Ma, Seokho Yun, Douglas H. Werner, Zhiwen Liu, and Theresa S. Mayer. "Broadband and Wide Field-of-View Plasmonic Metasurface-Enabled Waveplates." *Scientific Reports* 4, (2014): 7511.

[206] Wolf, Omri, Salvatore Campione, Alexander Benz, Arvind P. Ravikumar, Sheng Liu, Ting S. Luk, Emil A. Kadlec, Eric A. Shaner, John F. Klem, and Michael B. Sinclair. "Phased-Array Sources Based on Nonlinear Metamaterial Nanocavities." *Nature Communications* 6, (2015): 7667.

[207] Gil, Marta, Jordi Bonache, and Ferran Martin. "Metamaterial Filters: A Review." *Metamaterials* 2, no. 4 (2008): 186-197.

[208] Butt, Haider, Qing Dai, Timothy D. Wilkinson, and Gehan AJ Amaratunga. "Photonic Crystals & Metamaterial Filters Based on 2D Arrays of Silicon Nanopillars." *Progress in Electromagnetics Research* 113, (2011): 179-194.

[209] Brückner, Jean-Baptiste, Judikaël Le Rouzo, Ludovic Escoubas, Gérard Berginc, Olivier Calvo-Perez, Nicolas Vukadinovic, and François Flory. "Metamaterial Filters at Optical-Infrared Frequencies." *Optics Express* 21, no. 14 (2013): 16992-17006.

[210] Chen, Hou-Tong, Willie J. Padilla, Michael J. Cich, Abul K. Azad, Richard D. Averitt, and Antoinette J. Taylor. "A Metamaterial Solid-State Terahertz Phase Modulator." *Nature Photonics* 3, no. 3 (2009): 148.

[211] Chan, Wai Lam, Hou-Tong Chen, Antoinette J. Taylor, Igal Brener, Michael J. Cich, and Daniel M. Mittleman. "A Spatial Light Modulator for Terahertz Beams." *Applied Physics Letters* 94, no. 21 (2009): 213511.

[212] He, Xun-jun, Teng-yue Li, Lei Wang, Jian-min Wang, Jiu-xing Jiang, Guo-hui Yang, Fan-yi Meng, and Qun Wu. "Electrically Tunable Terahertz Wave Modulator Based on Complementary Metamaterial and Graphene." *Journal of Applied Physics* 115, no. 17 (2014): 17B903.

[213] Castellanos-Beltran, MA, KD Irwin, GC Hilton, LR Vale, and KW Lehnert. "Amplification and Squeezing of Quantum Noise with a Tunable Josephson Metamaterial." *Nature Physics* 4, no. 12 (2008): 929.

[214] Fei, Wei, Hao Yu, Yang Shang, and Kiat Seng Yeo. "A 2-D Distributed Power Combining by Metamaterial-Based Zero Phase Shifter for 60-GHz Power Amplifier in 65-Nm CMOS." *IEEE Trans. Microw. Theory Tech* 61, no. 1 (2013): 505-516.

[215] Zhu, Jiang and George V. Eleftheriades. "A Compact Transmission-Line Metamaterial Antenna with Extended Bandwidth." *IEEE Antennas and Wireless Propagation Letters* 8, (2009): 295-298.

[216] Li, Dongying, Zsolt Szabó, Xianming Qing, Er-Ping Li, and Zhi Ning Chen. "A High Gain Antenna with an Optimized Metamaterial Inspired Superstrate." *IEEE Transactions on Antennas and Propagation* 60, no. 12 (2012): 6018-6023.

[217] Bogue, Robert. "Sensing with Metamaterials: A Review of Recent Developments." *Sensor Review* 37, no. 3 (2017): 305-311.

[218] Karaaslan, Muharrem and Mehmet Bakir. "Chiral Metamaterial Based Multifunctional Sensor Applications." *Progress in Electromagnetics Research* 149, (2014): 55-67.

[219] Tao, Hu, Logan R. Chieffo, Mark A. Brenckle, Sean M. Siebert, Mengkun Liu, Andrew C. Strikwerda, Kebin Fan, David L. Kaplan, Xin Zhang, and Richard D. Averitt. "Metamaterials on Paper as a Sensing Platform." *Advanced Materials* 23, no. 28 (2011): 3197-3201.

[220] Al-Naib, Ibraheem. "Biomedical Sensing with Conductively Coupled Terahertz Metamaterial Resonators." *IEEE Journal of Selected Topics in Quantum Electronics* 23, no. 4 (2017): 1-5.

[221] Kabashin, AV, P. Evans, S. Pastkovsky, W. Hendren, GA Wurtz, R. Atkinson, R. Pollard, VA Podolskiy, and AV Zayats. "Plasmonic Nanorod Metamaterials for Biosensing." *Nature Materials* 8, no. 11 (2009): 867.

[222] Melik, Rohat, Emre Unal, Nihan Kosku Perkgoz, Christian Puttlitz, and Hilmi Volkan Demir. "Metamaterial-Based Wireless Strain Sensors." *Applied Physics Letters* 95, no. 1 (2009): 011106.

[223] Jakšić, Zoran. "Optical Metamaterials as the Platform for a Novel Generation of Ultrasensitive Chemical Or Biological Sensors." *Metamaterials: Classes, Properties and Applications* (2010): 1-42.

[224] Agarwal, Kriti, Chao Liu, Daeha Joung, Hyeong-Ryeol Park, Jeeyoon Jeong, Dai-Sik Kim, and Jeong-Hyun Cho. "Three-Dimensionally Coupled THz Octagrams as Isotropic Metamaterials." *ACS Photonics* 4, no. 10 (2017): 2436-2445.

[225] Agarwal, Kriti, Chao Liu, Daeha Joung, Hyeong-Ryeol Park, Sang-Hyun Oh, and Jeong-Hyun Cho. "Three-Dimensional Anisotropic Metamaterials as Triaxial Optical Inclinometers." *Scientific Reports* 7, no. 1 (2017): 2680.

[226] Chiam, Sher-Yi, Ranjan Singh, Jianqiang Gu, Jiaguang Han, Weili Zhang, and Andrew A. Bettiol. "Increased Frequency Shifts in High Aspect Ratio Terahertz Split Ring Resonators." *Applied Physics Letters* 94, no. 6 (2009): 064102.

[227] Gil, I., J. Garcia-Garcia, J. Bonache, F. Martin, M. Sorolla, and R. Marques. "Varactor-Loaded Split Ring Resonators for Tunable Notch Filters at Microwave Frequencies." *Electronics Letters* 40, no. 21 (2004): 1347-1348.

[228] Chevalier, Christine T. and Jeffrey D. Wilson. "Frequency Bandwidth Optimization of Left-Handed Metamaterial." (2004).

[229] Moser, HO, BDF Casse, O. Wilhelmi, and BT Saw. "Terahertz Response of a Microfabricated rod–split-Ring-Resonator Electromagnetic Metamaterial." *Physical Review Letters* 94, no. 6 (2005): 063901.

[230] Chen, Hou-Tong, Willie J. Padilla, Joshua MO Zide, Arthur C. Gossard, Antoinette J. Taylor, and Richard D. Averitt. "Active Terahertz Metamaterial Devices." *Nature* 444, no. 7119 (2006): 597.

[231] Plum, E., X-X Liu, VA Fedotov, Y. Chen, DP Tsai, and NI Zheludev. "Metamaterials: Optical Activity without Chirality." *Physical Review Letters* 102, no. 11 (2009): 113902.

[232] Zhang, Lei, Philippe Tassin, Thomas Koschny, Cihan Kurter, Steven M. Anlage, and Costas M. Soukoulis. "Large Group Delay in a Microwave Metamaterial Analog of Electromagnetically Induced Transparency." *Applied Physics Letters* 97, no. 24 (2010): 241904.

[233] Ding, Fei, Yanxia Cui, Xiaochen Ge, Yi Jin, and Sailing He. "Ultra-Broadband Microwave Metamaterial Absorber." *Applied Physics Letters* 100, no. 10 (2012): 103506.

[234] Gansel, J. K., M. Thiel, M. S. Rill, M. Decker, K. Bade, V. Saile, G. von Freymann, S. Linden, and M. Wegener. "Gold Helix Photonic Metamaterial as Broadband Circular Polarizer." *Science (New York, N.Y.)* 325, no. 5947 (Sep 18, 2009): 1513-1515.

[235] Decker, M., R. Zhao, CM Soukoulis, S. Linden, and M. Wegener. "Twisted Split-Ring-Resonator Photonic Metamaterial with Huge Optical Activity." *Optics Letters* 35, no. 10 (2010): 1593-1595.

[236] Ou, Jun-Yu, Eric Plum, Liudi Jiang, and Nikolay I. Zheludev. "Reconfigurable Photonic Metamaterials." *Nano Letters* 11, no. 5 (2011): 2142-2144.

[237] Tsang, Mankei and Demetri Psaltis. "Magnifying Perfect Lens and Superlens Design by Coordinate Transformation." *Physical Review B* 77, no. 3 (2008): 035122.

[238] Poddubny, Alexander, Ivan Iorsh, Pavel Belov, and Yuri Kivshar. "Hyperbolic Metamaterials." *Nature Photonics* 7, no. 12 (2013): 948.

[239] Fang, Nicholas and Xiang Zhang. "Imaging Properties of a Metamaterial Superlens."IEEE, 2002.

[240] Schurig, D., J. J. Mock, B. J. Justice, S. A. Cummer, J. B. Pendry, A. F. Starr, and D. R. Smith. "Metamaterial Electromagnetic Cloak at Microwave Frequencies." *Science (New York, N.Y.)* 314, no. 5801 (Nov 10, 2006): 977-980.

[241] Alu, Andrea and Nader Engheta. "Plasmonic and Metamaterial Cloaking: Physical Mechanisms and Potentials." *Journal of Optics A: Pure and Applied Optics* 10, no. 9 (2008): 093002.

[242] Cai, Wenshan, Uday K. Chettiar, Alexander V. Kildishev, and Vladimir M. Shalaev. "Optical Cloaking with Metamaterials." *Nature Photonics* 1, no. 4 (2007): 224.

[243] Moser, HO, BDF Casse, O. Wilhelmi, and BT Saw. "Terahertz Response of a Microfabricated rod–split-Ring-Resonator Electromagnetic Metamaterial." *Physical Review Letters* 94, no. 6 (2005): 063901.

[244] Aydin, Koray, Irfan Bulu, Kaan Guven, Maria Kafesaki, Costas M. Soukoulis, and Ekmel Ozbay. "Investigation of Magnetic Resonances for Different Split-Ring Resonator Parameters and Designs." *New Journal of Physics* 7, no. 1 (2005): 168.

[245] Liu, Chao, Kriti Agarwal, Yuping Zhang, Dibakar Roy Chowdhury, Abul K. Azad, and Jeong-Hyun Cho. "Displacement Current Mediated Resonances in Terahertz Metamaterials." *Advanced Optical Materials* 4, no. 8 (2016): 1302-1309.

[246] Padilla, Willie J., Antoinette J. Taylor, Clark Highstrete, Mark Lee, and Richard D. Averitt. "Dynamical Electric and Magnetic Metamaterial Response at Terahertz Frequencies." *Physical Review Letters* 96, no. 10 (2006): 107401.

[247] Sersic, Ivana, Martin Frimmer, Ewold Verhagen, and A. Femius Koenderink. "Electric and Magnetic Dipole Coupling in Near-Infrared Split-Ring Metamaterial Arrays." *Physical Review Letters* 103, no. 21 (2009): 213902.

[248] Deibel, Jason A., Hannah R. Jones, A. Fosnight, R. Shaver, E. Best, D. Langley, Lavern A. Starman, and RA Coutu. "Flexible Terahertz Metamaterials for Frequency Selective Surfaces." In *MEMS and Nanotechnology, Volume 5*, 129-134: Springer, 2014.

[249] Harlow, James H. *Electric Power Transformer Engineering* CRC press, 2012.

[250] Ebrahimi, Amir, Withawat Withayachumnankul, Said Al-Sarawi, and Derek Abbott. "High-Sensitivity Metamaterial-Inspired Sensor for Microfluidic Dielectric Characterization." *IEEE Sensors Journal* 14, no. 5 (2014): 1345-1351.

[251] Ng, Jack, Huanyang Chen, and Che Ting Chan. "Metamaterial Frequency-Selective Superabsorber." *Optics Letters* 34, no. 5 (2009): 644-646.

[252] Soukoulis, Costas M. and Martin Wegener. "Past Achievements and Future Challenges in the Development of Three-Dimensional Photonic Metamaterials." *Nature Photonics* 5, no. 9 (2011): 523.

[253] Xu, Xinlong, Bo Peng, Dehui Li, Jun Zhang, Lai Mun Wong, Qing Zhang, Shijie Wang, and Qihua Xiong. "Flexible visible–infrared Metamaterials and their Applications in Highly Sensitive Chemical and Biological Sensing." *Nano Letters* 11, no. 8 (2011): 3232-3238.

[254] Singh, Ranjan, Wei Cao, Ibraheem Al-Naib, Longqing Cong, Withawat Withayachumnankul, and Weili Zhang. "Ultrasensitive Terahertz Sensing with High-Q Fano Resonances in Metasurfaces." *Applied Physics Letters* 105, no. 17 (2014): 171101.

[255] Torun, Hamdi, F. Cagri Top, G. Dundar, and AD Yalcinkaya. "An Antenna-Coupled Split-Ring Resonator for Biosensing." *Journal of Applied Physics* 116, no. 12 (2014): 124701.

[256] Chen, Tao, Suyan Li, and Hui Sun. "Metamaterials Application in Sensing." *Sensors* 12, no. 3 (2012): 2742-2765.

[257] Jaruwongrungsee, K., U. Waiwijit, W. Withayachumnankul, T. Maturos, D. Phokaratkul, A. Tuantranont, W. Wlodarski, A. Martucci, and A. Wisitsoraat. "Microfluidic-Based Split-Ring-Resonator Sensor for Real-Time and Label-Free Biosensing." *Procedia Engineering* 120, (2015): 163-166.

[258] Han, Jiaguang and Akhlesh Lakhtakia. "Semiconductor Split-Ring Resonators for Thermally Tunable Terahertz Metamaterials." *Journal of Modern Optics* 56, no. 4 (2009): 554-557.

[259] Melik, Rohat, Emre Unal, Nihan Kosku Perkgoz, Christian Puttlitz, and Hilmi Volkan Demir. "Flexible Metamaterials for Wireless Strain Sensing." *Applied Physics Letters* 95, no. 18 (2009): 181105.

[260] Naqui, Jordi, Miguel Durán-Sindreu, and Ferran Martín. "Alignment and Position Sensors Based on Split Ring Resonators." *Sensors* 12, no. 9 (2012): 11790-11797.

[261] Driscoll, T., GO Andreev, DN Basov, S. Palit, SY Cho, NM Jokerst, and DR Smith. "Tuned Permeability in Terahertz Split-Ring Resonators for Devices and Sensors." *Applied Physics Letters* 91, no. 6 (2007): 062511.

[262] Hao, Tong, CJ Stevens, and DJ Edwards. "Optimisation of Metamaterials by Q Factor." *Electronics Letters* 41, no. 11 (2005): 653-654.

[263] Anetsberger, Georg, Olivier Arcizet, Quirin P. Unterreithmeier, Rémi Rivière, Albert Schliesser, Eva Maria Weig, Jörg P. Kotthaus, and Tobias J. Kippenberg. "Near-Field Cavity Optomechanics with Nanomechanical Oscillators." *Nature Physics* 5, no. 12 (2009): 909.

[264] Cong, Longqing, Siyu Tan, Riad Yahiaoui, Fengping Yan, Weili Zhang, and Ranjan Singh. "Experimental Demonstration of Ultrasensitive Sensing with Terahertz Metamaterial Absorbers: A Comparison with the Metasurfaces." *Applied Physics Letters* 106, no. 3 (2015): 031107.

[265] Güney, Durdu Ö., Thomas Koschny, and Costas M. Soukoulis. "Reducing Ohmic Losses in Metamaterials by Geometric Tailoring." *Physical Review B* 80, no. 12 (2009): 125129.

[266] Chen, Jiun-Yeu, Wang-Lin Chen, Jia-Yi Yeh, Lien-Wen Chen, and Ching-Cheng Wang. "Comparative Analysis of Split-Ring Resonators for Tunable Negative Permeability Metamaterials Based on Anisotropic Dielectric Substrates." *Progress in Electromagnetics Research* 10, (2009): 25-38.

[267] R. Hopkins, presented at *IMAPS 39th int. symp. microelectronics*, San diego, CA, USA (2006), 65

[268] Srivastava, Yogesh Kumar, Manukumara Manjappa, Longqing Cong, Wei Cao, Ibraheem Al-Naib, Weili Zhang, and Ranjan Singh. "Ultrahigh-Q Fano Resonances in Terahertz Metasurfaces: Strong Influence of Metallic Conductivity at Extremely Low Asymmetry." *Advanced Optical Materials* 4, no. 3 (2016): 457-463.

[269] Cong, Longqing, Manukumara Manjappa, Ningning Xu, Ibraheem Al-Naib, Weili Zhang, and Ranjan Singh. "Fano Resonances in Terahertz Metasurfaces: A Figure of Merit Optimization." *Advanced Optical Materials* 3, no. 11 (2015): 1537-1543.

[270] Fedotov, VA, M. Rose, SL Prosvirnin, N. Papasimakis, and NI Zheludev. "Sharp Trapped-Mode Resonances in Planar Metamaterials with a Broken Structural Symmetry." *Physical Review Letters* 99, no. 14 (2007): 147401.

[271] Tsakmakidis, KL, MS Wartak, JJH Cook, JM Hamm, and O. Hess. "Negative-Permeability Electromagnetically Induced Transparent and Magnetically Active Metamaterials." *Physical Review B* 81, no. 19 (2010): 195128.

[272] Jansen, Christian, Ibraheem AI Al-Naib, Norman Born, and Martin Koch. "Terahertz Metasurfaces with High Q-Factors." *Applied Physics Letters* 98, no. 5 (2011): 051109.

[273] Chowdhury, Dibakar Roy, Xiaofang Su, Yong Zeng, Xiaoshuang Chen, Antoinette J. Taylor, and Abul Azad. "Excitation of Dark Plasmonic Modes in Symmetry Broken Terahertz Metamaterials." *Optics Express*22, no. 16 (2014): 19401-19410.

[274] Al-Naib, Ibraheem, Yuping Yang, Marc M. Dignam, Weili Zhang, and Ranjan Singh. "Ultra-High Q Even Eigenmode Resonance in Terahertz Metamaterials." *Applied Physics Letters* 106, no. 1 (2015): 011102.

[275] O'Hara, John F., Ranjan Singh, Igal Brener, Evgenya Smirnova, Jiaguang Han, Antoinette J. Taylor, and Weili Zhang. "Thin-Film Sensing with Planar Terahertz Metamaterials: Sensitivity and Limitations." *Optics Express* 16, no. 3 (2008): 1786-1795.

[276] Cubukcu, Ertugrul, Shuang Zhang, Yong-Shik Park, Guy Bartal, and Xiang Zhang. "Split Ring Resonator Sensors for Infrared Detection of Single Molecular Monolayers." *Applied Physics Letters* 95, no. 4 (2009): 043113.

[277] Park, Hyeong-Ryeol, Kwang Jun Ahn, Sanghoon Han, Young-Mi Bahk, Namkyoo Park, and Dai-Sik Kim. "Colossal Absorption of Molecules Inside Single Terahertz Nanoantennas." *Nano Letters* 13, no. 4 (2013): 1782-1786.

[278] Toma, Andrea, Salvatore Tuccio, Mirko Prato, Francesco De Donato, Andrea Perucchi, Paola Di Pietro, Sergio Marras, Carlo Liberale, Remo Proietti Zaccaria, and

Francesco De Angelis. "Squeezing Terahertz Light into Nanovolumes: Nanoantenna Enhanced Terahertz Spectroscopy (NETS) of Semiconductor Quantum Dots." *Nano Letters* 15, no. 1 (2014): 386-391.

[279] La Spada, Luigi, Filiberto Bilotti, and Lucio Vegni. "Metamaterial-Based Sensor Design Working in Infrared Frequency Range." *Progress in Electromagnetics Research* 34, (2011): 205-223.

[280] Chow, Tai L. *Introduction to Electromagnetic Theory: A Modern Perspective* Jones & Bartlett Learning, 2006.

[281] Lee, SeungYeon, Daniel Wratkowski, and Jeong-Hyun Cho. "Patterning Anodic Porous Alumina with Resist Developers for Patterned Nanowire Formation." *MRS Online Proceedings Library Archive* 1785, (2015): 13-18.

[282] Cho, Jeong-Hyun and S. Tom Picraux. "Enhanced Lithium Ion Battery Cycling of Silicon Nanowire Anodes by Template Growth to Eliminate Silicon Underlayer Islands." *Nano Letters* 13, no. 11 (2013): 5740-5747.

[283] Cho, Jeong-Hyun and S. Tom Picraux. "Silicon Nanowire Degradation and Stabilization during Lithium Cycling by SEI Layer Formation." *Nano Letters* 14, no. 6 (2014): 3088-3095.

[284] Ida, Nathan. *Engineering Electromagnetics*. Vol. 2 Springer, 2000.

[285] Aydin, K. and E. Ozbay. "Identifying Magnetic Response of Split-Ring Resonators at Microwave Frequencies." *Opto-Electronics Review* 14, no. 3 (2006): 193-199.

[286] Koschny, Th, M. Kafesaki, EN Economou, and CM Soukoulis. "Effective Medium Theory of Left-Handed Materials." *Physical Review Letters* 93, no. 10 (2004): 107402.

[287] Katsarakis, N., Th Koschny, M. Kafesaki, EN Economou, and CM Soukoulis. "Electric Coupling to the Magnetic Resonance of Split Ring Resonators." *Applied Physics Letters* 84, no. 15 (2004): 2943-2945.

[288] Zhou, Jiangfeng, Thomas Koschny, and Costas M. Soukoulis. "Magnetic and Electric Excitations in Split Ring Resonators." *Optics Express* 15, no. 26 (2007): 17881-17890.

[289] Hammond, Percy. *Electromagnetism for Engineers: An Introductory Course* Elsevier, 2013.

[290] Zhao, Yan, Christos Argyropoulos, and Yang Hao. "Full-Wave Finite-Difference Time-Domain Simulation of Electromagnetic Cloaking Structures." *Optics Express* 16, no. 9 (2008): 6717-6730.

[291] Argyropoulos, Christos, Yan Zhao, and Yang Hao. "A Radially-Dependent Dispersive Finite-Difference Time-Domain Method for the Evaluation of Electromagnetic Cloaks." *IEEE Transactions on Antennas and Propagation* 57, no. 5 (2009): 1432-1441.

[292] Le Floch, Jean-Michel, Michael E. Tobar, Dominique Cros, and Jerzy Krupka. "Low-Loss Materials for High Q-Factor Bragg Reflector Resonators." *Applied Physics Letters* 92, no. 3 (2008): 032901.

[293] Argyropoulos, Christos, Efthymios Kallos, Yan Zhao, and Yang Hao. "Manipulating the Loss in Electromagnetic Cloaks for Perfect Wave Absorption." *Optics Express* 17, no. 10 (2009): 8467-8475.

[294] Fleury, Romain and Andrea Alù. "Cloaking and Invisibility: A Review."2014.

Appendix A

MATLAB Script for MM Cloaking

```
%Metamaterial Cloaking Simulations

%Created by Chao Liu

%University of Minnesota, Twin Cities

%%%%%%%%%%%%%%%%%%%%%%%%%%%%%%%%%%%%%%%%%%%%%%%%%%%%%%%%%%%%%%%%%%%%%%%%%%%%%%%%

%Begin Scripts

%%%%%%%%%%%%%%%%%%%%%%%%%%%%%%%%%%%%%%%%%%%%%%%%%%%%%%%%%%%%%%%%%%%%%%%%%%%%%%%%

clear all;

%define constants

%basic constants

R1 = 100; %inner radius
R2 = 200; %outer radius
A=R2/(R2-R1); %used in Hz calculation
PMLw = 50; % perfect matched layer width

cc = 2.99792458e8; %light speed of free space
mu = 4.0*pi*1.0e-7; %permeability of free space
eps = 1.0/(cc*cc*mu); %permittivity of free space
freq = 2.0e9; %frequency of source, 2GHz
lambda = cc/freq; %wavelength of source, meter
omega = 2*pi*freq; %angular frequency
epsr = @(r) (r-R1)/r; %relative permittivity
epsphi = @(r) r/(r-R1); % phi permittivity
muz =@(r) (A^2)*((r-R1)/r); % mue z

% cloaking constants

dx = lambda/150; % cell size
dy = dx;
dt = dx/(sqrt(2)*cc); %time step
amp = 0.2; % amplitude of the source
js = 6+PMLw; % location of the source
nmax = 300; % max time step

%%%%%%%%%%%%%%%%%%%%%%%%%%%%%%%%%%%%%%%%%%%%%%%%%%%%%%%%%%%%%%%%%%%%%%%%%%%%%%%%

% loss parameters

q = 100;

sterm = sin(omega*dt/2); %for lossy
cterm = cos(omega*dt/2); %for lossy

tangente = 1.71/q; % loss tangent E
tangentm = 1.71/q; % loss tangent M
```

```
gamma = @(r) (2*epsr(r)*(sterm)*tangente)/((1-epsr(r))*dt*(cterm)); % collision frequency
gammam = @(r) ((muz(r)/A)*omega*tangentm)/(1-(muz(r)/A)); % magnetic collision frequency

wpsq = @(r) 2*(sterm)*(-2*(epsr(r)-1)*(sterm)+epsr(r)*gamma(r)*dt*(cterm)*tangente)/((dt^2)*((cterm)^2)); % lossy wp square

wpmsq =@(r) (omega^2)*(1-muz(r)/A)+(muz(r)/A)*omega*gammam(r)*tangentm; % magnetic wp square, lossy

invtm = 1/(mu*(dt^2)); % 1 over mue*dt square

%%%%%%%%%%%%%%%%%%%%%%%%%%%%%%%%%%%%%%%%%%%%%%%%%%%%%%%%%%%%%%%%%%%

%grid constants

ie = 800; % mesh x
je = 900; % mesh y
ib = ie; % ey(800,800)
jb = je+1; % ex(800,801)
icenter = ie/2; % x center of mesh
jcenter = (je-100)/2; % y center of mesh
exinc = 0; % Ex inside cloak count
exoutc = 0; % Ex outside cloak count
eyinc = 0; % Ey inside cloak count
eyoutc = 0; % Ey outside cloak count
hzinc = 0; % Hz inside cloak count
hzoutc = 0; % Hz outside cloak count

%%%%%%%%%%%%%%%%%%%%%%%%%%%%%%%%%%%%%%%%%%%%%%%%%%%%%%%%%%%%%%%%%%%

%Field initialization

ex = zeros(ie,jb); % Ex initial
exprev = ex;
exprevprev =exprev;

exmask = ones(ie,jb); % Ex mask

ey = zeros(ib,je); % Ey initial
eyprev = ey;
eyprevprev =eyprev;

eymask = ones(ib,je); % Ey mask

Dx = ex; % Dx initial
Dxprev = Dx;
Dxprevprev =Dxprev;

Dy = ey; % Dy initial
Dyprev = Dy;
Dyprevprev =Dyprev;

dbary = ex; %Dy bar initial
dbaryprev = dbary;
dbaryprevprev = dbaryprev;

dbarx = ey; %Dx bar initial
dbarxprev = dbarx;
dbarxprevprev = dbarxprev;

hz = zeros(ie, je); % Hz initial
hzprev = hz;
hzprevprev = hz;
```

```
hzmask = ones(ie,je); % Hz mask

bz = hz; %Bz initial
bzprev = bz;
bzprevprev = bzprev;

%%%%%%%%%%%%%%%%%%%%%%%%%%%%%%%%%%%%%%%%%%%%%%%%%%%%%%%%%%%%%%%%%%%%%%%%%%%%%%%%%%%%%%%%%%%%%%%%%%%%%%%%%%%%%%%%%%%%%%%%

% PML fields initialization

PsiEx = zeros(ie,jb);
PsiEy = zeros(ib,je);
PsiHzX = zeros(ie,je);
PsiHzY = zeros(ie,je);

% PML parameters

kapp =1;
kappe=1.5;
kappm=1.5;
a=0.0004;
sig=0.045;

%Electric coefficient

sigex=0;
sigey=sig;
kappex=kapp;
kappey=kapp;
aex = a;
aey = a;
bex = exp(-1*(aex/eps+0+sigex/(kappex*eps))*dt);
bey = exp(-1*(aey/eps+sigey/(kappey*eps))*dt);
cex = (bex-1)*sigex/(sigex*kappex+kappe^2*aex);
cey = (bey-1)*sigey/(sigey*kappey+kappe^2*aey);

%Magnetic coefficient

amx = a;
amy = a;
kappmx=kapp;
kappmy=kapp;
sigmx=0;
sigmy = mu/eps*sig;
bmx = exp(-1*(amx/mu+sigmx/(kappmx*mu))*dt);
bmy = exp(-1*(amy/mu+sigmy/(kappmy*mu))*dt);
cmx = (bmx-1)*sigmx/(sigmx*kappmx+kappm^2*amx);
cmy = (bmy-1)*sigmy/(sigmy*kappmy+kappm^2*amy);

%%%%%%%%%%%%%%%%%%%%%%%%%%%%%%%%%%%%%%%%%%%%%%%%%%%%%%%%%%%%%%%%%%%%%%%%%%%%%%%%%%%%%%%%%%%%%%%%%%%%%%%%%%%%%%%%%%%%%%%%

%Updating parameters for Ex

gamot =@(r) gamma(r)/(2*dt); %gamma over two times dt (0 if lossless, non-0 if lossy)
invt = 1/(dt^2); %1 over dt square
ax = @(r,phi) ((sin(phi))^2)*(invt + gamot(r) + wpsq(r)/4) + epsphi(r)*((cos(phi))^2)*(invt + gamot(r));
bx = @(r,phi) ((sin(phi))^2)*(-2*invt + wpsq(r)/2) - epsphi(r)*((cos(phi))^2)*2*invt;
cx = @(r,phi) ((sin(phi))^2)*(invt - gamot(r) + wpsq(r)/4) + epsphi(r)*((cos(phi))^2)*(invt - gamot(r));
ddx = @(r,phi) (epsphi(r)*(invt + gamot(r))-(invt + gamot(r) + wpsq(r)/4))*sin(phi)*cos(phi);
eex = @(r,phi) (epsphi(r)*(-2)*invt-(-2*invt + wpsq(r)/2))*sin(phi)*cos(phi);
fx = @(r,phi) (epsphi(r)*(invt - gamot(r))-(invt - gamot(r) + wpsq(r)/4))*sin(phi)*cos(phi);
```

```
gx = @(r) eps*epsphi(r)*(-2*invt+wpsq(r)/2);
hx = @(r) eps*epsphi(r)*(invt - gamot(r) + wpsq(r)/4);
lx = @(r) eps*epsphi(r)*(invt + gamot(r) + wpsq(r)/4);

%%%%%%%%%%%%%%%%%%%%%%%%%%%%%%%%%%%%%%%%%%%%%%%%%%%%%%%%%%

%Updating parameters for Ey

ay = @(r,phi) ((cos(phi))^2)*(invt + gamot(r) + wpsq(r)/4) + epsphi(r)*((sin(phi))^2)*(invt + gamot(r));
by = @(r,phi) ((cos(phi))^2)*(-2*invt + wpsq(r)/2) - epsphi(r)*((sin(phi))^2)*(2*invt);
cy = @(r,phi) ((cos(phi))^2)*(invt - gamot(r) + wpsq(r)/4) + epsphi(r)*((sin(phi))^2)*(invt - gamot(r));
ddy = ddx;
eey = eex;
fy = fx;
gy = gx;
hy = hx;
ly = lx;

%%%%%%%%%%%%%%%%%%%%%%%%%%%%%%%%%%%%%%%%%%%%%%%%%%%%%%%%%%

%Grid Steup for Ex

for i=1:ie
   for j=2+PMLw:jb-PMLw-1  % loop all nodes in the grid
tempx = i -1 - icenter;
tempy = j -1 - jcenter;
dist2 = tempx^2 + tempy^2; % distance between current node and center

%%%%%%%%%%%%%%%%%%%%%%%%%%%%%%%%%%%%%%%%%%%%%%%%%%%%%%%%%%

if dist2 < R2^2 && dist2 > R1^2 % inside the cloak
   exinc = exinc +1; % exinc -- inside cloak Ex counting
   exincl(exinc,:)=[i j]; % store Ex location (inside the cloak) - all column
   if tempy==0 && tempx>0 % updating phi value based on node location (inside the cloak)
      phiex = 0;
   elseif tempy==0 && tempx<0
      phiex = pi;
   elseif tempx==0 && tempy>0
      phiex = pi/2;
   elseif tempx==0 && tempy<0
      phiex = 3*pi/2;
   elseif tempx>0 && tempy>0 %Q1
      phiex = atan(tempy/tempx);
   elseif tempx<0 && tempy>0 %Q2
      phiex = pi-abs(atan(tempy/tempx));
   elseif tempx<0 && tempy<0 %Q3
      phiex = pi+abs(atan(tempy/tempx));
   else %Q4
      phiex = 2*pi-abs(atan(tempy/tempx));
   end

   radex=sqrt(dist2); %distance between current node and center
   coefax(exinc)= ax(radex,phiex); %updating coefficient for each node inside the cloak
   coefbx(exinc)= bx(radex,phiex);
   coefcx(exinc)= cx(radex,phiex);
   coefddx(exinc)= ddx(radex,phiex);
   coefeex(exinc)= eex(radex,phiex);
   coeffx(exinc)= fx(radex,phiex);
   coefgx(exinc)= gx(radex);
   coefhx(exinc)= hx(radex);
   coeflx(exinc)= lx(radex);
```

```
%%%%%%%%%%%%%%%%%%%%%%%%%%%%%%%%%%%%%%%%%%%%%%%%%%%%%%%%%%%%
else    % other than inside the cloak
%elseif dist2 >= R2^2  % in free space
   exoutc = exoutc + 1; % in free space Ex counting
   exout(exoutc, :) = [i j]; % store Ex location (in free space) - all column

%%%%%%%%%%%%%%%%%%%%%%%%%%%%%%%%%%%%%%%%%%%%%%%%%%%%%%%%%%%%

%else   %in the PEC
end

if dist2 <= R1^2

   exmask(i,j) = 0;

end
   end
end

%%%%%%%%%%%%%%%%%%%%%%%%%%%%%%%%%%%%%%%%%%%%%%%%%%%%%%%%%%%%

%Grid Steup for Ey

for i=1:ib
   for j=1+PMLw:je-PMLw  % loop all nodes in the grid
tempx = i  -1.5 - icenter;
tempy = j -1.5 - jcenter;
dist2 = tempx^2 + tempy^2; % distance between current node and center

%%%%%%%%%%%%%%%%%%%%%%%%%%%%%%%%%%%%%%%%%%%%%%%%%%%%%%%%%%%%

if dist2 < R2^2 && dist2 > R1^2 % inside the cloak
   eyinc = eyinc +1; % eyinc -- inside cloak Ey counting
   eyincl(eyinc,:)=[i j]; % store Ey location (inside the cloak) - all column
   if tempy==0 && tempx>0 % updating phi value based on node location (inside the cloak)
      phiey = 0;
   elseif tempy==0 && tempx<0
      phiey = pi;
   elseif tempx==0 && tempy>0
      phiey = pi/2;
   elseif tempx==0 && tempy<0
      phiey = 3*pi/2;
   elseif tempx>0 && tempy>0 %Q1
      phiey = atan(tempy/tempx);
   elseif tempx<0 && tempy>0 %Q2
      phiey = pi-abs(atan(tempy/tempx));
   elseif tempx<0 && tempy<0 %Q3
      phiey = pi+abs(atan(tempy/tempx));
   else %Q4
      phiey = 2*pi-abs(atan(tempy/tempx));
   end

   radey=sqrt(dist2); %distance between current node and center
   coefay(eyinc)= ay(radey,phiey); %updating coefficient for each node inside the cloak
   coefby(eyinc)= by(radey,phiey);
   coefcy(eyinc)= cy(radey,phiey);
   coefddy(eyinc)= ddy(radey,phiey);
   coefeey(eyinc)= eey(radey,phiey);
   coeffy(eyinc)= fy(radey,phiey);
   coefgy(eyinc)= gy(radey);
   coefhy(eyinc)= hy(radey);
   coefly(eyinc)= ly(radey);
```

```
%%%
```

```
hFig=figure('Visible','off');

%%%%%%%%%%%%%%%%%%%%%%%%%%%%%%%%%%%%%%%%%%%%%%%%%%%%%%%%%%%%%

%Time Loop Begin

for n = 1:nmax
   t=n*dt; % time
   Time_step=n % display time step
   cla % clear all axes
%%%%%%%%%%%%%%%%%%%%%%%%%%%%%%%%%%%%%%%%%%%%%%%%%%%%%%%%%%%%%

% PML field setup for Ex

PsiEx(:,2:jb-1) = (cey/dx)*(hzprev(:,1:jb-2)-hzprev(:,2:jb-1))+bey*PsiEx(:,2:jb-1);

%%%%%%%%%%%%%%%%%%%%%%%%%%%%%%%%%%%%%%%%%%%%%%%%%%%%%%%%%%%%%

%Dx

Dx(:,2+PMLw:jb-PMLw-1) = Dxprev(:,2+PMLw:jb-PMLw-1)+(dt/dx)*(-hzprev(:,2+PMLw:jb-PMLw-
1)+hzprev(:,PMLw+1:jb-PMLw-2));

%Dx and Dy in PML lower region

Dx(:,2:PMLw+1) = Dxprev(:,2:PMLw+1)+dt*((-hzprev(:,2:PMLw+1)+hzprev(:,1:PMLw))*
1/dx+PsiEx(:,2:PMLw+1));

%Dx and Dy in PML higher region

Dx(:,jb-PMLw:jb-1) = Dxprev(:,jb-PMLw:jb-1)+dt*((hzprev(:,jb-PMLw-1:jb-2)-hzprev(:,jb-PMLw:jb-1))* 1/dx
+PsiEx(:,jb-PMLw:jb-1));

%%%%%%%%%%%%%%%%%%%%%%%%%%%%%%%%%%%%%%%%%%%%%%%%%%%%%%%%%%%%%

% PML field setup for Ey

PsiEy(1:ib-1,:) = bex*PsiEy(1:ib-1,:);
PsiEy(ib,:) = bex*PsiEy(ib,:);

%Dy

Dy(1:ib-1,:) = Dyprev(1:ib-1,:)+(dt/dy)*(hzprev(2:ib,:)-hzprev(1:ib-1,:));
Dy(ib,:) = Dyprev(ib,:)+(dt/dy)*(hzprev(1,:)-hzprev(ib,:));

%%%%%%%%%%%%%%%%%%%%%%%%%%%%%%%%%%%%%%%%%%%%%%%%%%%%%%%%%%%%%

%Ex setup

for i = 1:exoutc % looping in free space
   ii=exout(i,1); % Ex location x (in free space)
   jj=exout(i,2); % Ex location y (in free space)
   ex(ii,jj) = (1/(eps*invt))*(invt*Dx(ii,jj)-2*invt*Dxprev(ii,jj)+invt*Dxprevprev(ii,jj)-(-
2*eps*invt*exprev(ii,jj)+eps*invt*exprevprev(ii,jj)));
end

dbary(3:ie-2,4+PMLw:jb-PMLw-3) = 0.25*(Dy(3:ie-2,4+PMLw:jb-PMLw-3)+Dy(2:ie-3,4+PMLw:jb-PMLw-
3)+Dy(3:ie-2,3+PMLw:jb-PMLw-4)+Dy(2:ie-3,3+PMLw:jb-PMLw-4)); %updating Dy bar

for i = 1:exinc %looping inside the cloak
   ii=exincl(i,1); % Ex location x (inside the cloak)
   jj=exincl(i,2); % Ex location y (inside the cloak)
```

```
   %dbary(ii,jj) = 0.25*(Dy(ii,jj-1)+Dy(ii+1,jj-1)+Dy(ii,jj)+Dy(ii+1,jj)); %updating Dy bar
   ex(ii,jj) =
(1/coeflx(i))*(coefax(i)*Dx(ii,jj)+coefbx(i)*Dxprev(ii,jj)+coefcx(i)*Dxprevprev(ii,jj)+coefddx(i)*dbary(ii,jj)+coefeex(i)
*dbaryprev(ii,jj)+coeffx(i)*dbaryprevprev(ii,jj)-(coefgx(i)*exprev(ii,jj)+coefhx(i)*exprevprev(ii,jj)));
end

%Ex setup for PML

ex(:,2:PMLw+1)=(1/eps)*Dx(:,2:PMLw+1);
ex(:,jb-PMLw:jb-1)=(1/eps)*Dx(:,jb-PMLw:jb-1);

%%%%%%%%%%%%%%%%%%%%%%%%%%%%%%%%%%%%%%%%%%%%%%%%%%%%%%%%%%%%%%%%%%%%%%%%%

% Ex mask for in the PEC

ex(:,:) = ex(:,:).*exmask;
Dx(:,:) = Dx(:,:).*exmask;

%%%%%%%%%%%%%%%%%%%%%%%%%%%%%%%%%%%%%%%%%%%%%%%%%%%%%%%%%%%%%%%%%%%%%%%%%

%Ey setup

for i = 1:eyoutc % looping in free space
   ii=eyout(i,1); % Ey location x (in free space)
   jj=eyout(i,2); % Ey location y (in free space)
   ey(ii,jj) = (1/(eps*invt))*(invt*Dy(ii,jj)-2*invt*Dyprev(ii,jj)+invt*Dyprevprev(ii,jj)-(-
2*eps*invt*eyprev(ii,jj)+eps*invt*eyprevprev(ii,jj)));
end

dbarx(3:ib-3,3+PMLw:je-PMLw-2) = 0.25*(Dx(3:ib-3,3+PMLw:je-PMLw-2)+Dx(4:ib-2,3+PMLw:je-PMLw-
2)+Dx(3:ib-3,4+PMLw:je-PMLw-1)+Dx(4:ib-2,4+PMLw:je-PMLw-1));

for i = 1:eyinc %looping inside the cloak
   ii=eyincl(i,1); % Ey location x (inside the cloak)
   jj=eyincl(i,2); % Ey location y (inside the cloak)
   %dbarx(ii,jj) = 0.25*(Dx(ii,jj)+Dx(ii-1,jj+1)+Dx(ii-1,jj)+Dx(ii,jj+1)); %updating Dx bar
   ey(ii,jj) =
(1/coefly(i))*(coefay(i)*Dy(ii,jj)+coefby(i)*Dyprev(ii,jj)+coefcy(i)*Dyprevprev(ii,jj)+coefddy(i)*dbarx(ii,jj)+coefeey(i)
*dbarxprev(ii,jj)+coeffy(i)*dbarxprevprev(ii,jj)-(coefgy(i)*eyprev(ii,jj)+coefhy(i)*eyprevprev(ii,jj)));
end

%Ey setup for PML

ey(:,1:PMLw) = (1/eps)*Dy(:,1:PMLw);
ey(:,je-PMLw+1:je) = (1/eps)*Dy(:,je-PMLw+1:je);

%%%%%%%%%%%%%%%%%%%%%%%%%%%%%%%%%%%%%%%%%%%%%%%%%%%%%%%%%%%%%%%%%%%%%%%%%

% Ey mask for in the PEC

ey(:,:) = ey(:,:).*eymask;
Dy(:,:) = Dy(:,:).*eymask;

%%%%%%%%%%%%%%%%%%%%%%%%%%%%%%%%%%%%%%%%%%%%%%%%%%%%%%%%%%%%%%%%%%%%%%%%%

% HzX and HzY in PML

PsiHzX(2:ie,1:je) = bmx*PsiHzX(2:ie,1:je);
PsiHzX(1,1:je) = bmx*PsiHzX(1,1:je);

PsiHzY(2:ie,1:je) = (cmy/dy)*(-ex(2:ie,2:je+1)+ex(2:ie,1:je))+bmy*PsiHzY(2:ie,1:je);
PsiHzY(1,1:je) = (cmy/dy)*(-ex(1,2:je+1)+ex(1,1:je))+bmy*PsiHzY(1,1:je);
```

```
%Bz update

bz(2:ie,1+PMLw:je-PMLw) = bzprev(2:ie,1+PMLw:je-PMLw)+(dt/dx)*(ex(2:ie,1+PMLw:je-PMLw)-ex(2:ie,2+PMLw:je-PMLw+1)+ey(2:ie,1+PMLw:je-PMLw)-ey(1:ie-1,1+PMLw:je-PMLw));
bz(1,1+PMLw:je-PMLw) = bzprev(1,1+PMLw:je-PMLw)+(dt/dx)*(ex(1,1+PMLw:je-PMLw)-ex(1,2+PMLw:je-PMLw+1)+ey(1,1+PMLw:je-PMLw)-ey(ie,1+PMLw:je-PMLw));

%Bz update - in PML

bz(2:ie,1:PMLw) = bzprev(2:ie,1:PMLw)+dt*((ex(2:ie,1:PMLw)-ex(2:ie,2:PMLw+1)+ey(2:ie,1:PMLw)-ey(1:ie-1,1:PMLw))* 1/dx + PsiHzX(2:ie,1:PMLw)+PsiHzY(2:ie,1:PMLw));
bz(1,1:PMLw) = bzprev(1,1:PMLw)+dt*((ex(1,1:PMLw)-ex(1,2:PMLw+1)+ey(1,1:PMLw)-ey(ie,1:PMLw))* 1/dx + PsiHzX(1,1:PMLw)+PsiHzY(1,1:PMLw));
bz(2:ie,je-PMLw+1:je) = bzprev(2:ie,je-PMLw+1:je)+dt*((ex(2:ie,je-PMLw+1:je)-ex(2:ie,je-PMLw+2:je+1)+ey(2:ie,je-PMLw+1:je)-ey(1:ie-1,je-PMLw+1:je))* 1/dx + PsiHzX(2:ie,je-PMLw+1:je)+PsiHzY(2:ie,je-PMLw+1:je));
bz(1,je-PMLw+1:je) = bzprev(1,je-PMLw+1:je)+dt*((ex(1,je-PMLw+1:je)-ex(1,je-PMLw+2:je+1)+ey(1,je-PMLw+1:je)-ey(ie,je-PMLw+1:je))* 1/dx + PsiHzX(1,je-PMLw+1:je)+PsiHzY(1,je-PMLw+1:je));

%%%%%%%%%%%%%%%%%%%%%%%%%%%%%%%%%%%%%%%%%%%%%%%%%%%%%%%%%%%%%%%%%%%%%%%%%%%%%%%

%Hz update

for i=1:hzoutc % in free space
   ii=hzout(i,1);
   jj=hzout(i,2);
   hz(ii,jj) = (invtm*bz(ii,jj)-2*invtm*bzprev(ii,jj)+invtm*bzprevprev(ii,jj)+2*invt*hzprev(ii,jj)-invt*hzprevprev(ii,jj))/invt;
end

for i=1:hzinc % inside the cloak
   ii=hzincl(i,1);
   jj=hzincl(i,2);
   hz(ii,jj) = (1/A)*((invtm+(gammam(radhz(i))/(2*mu*dt)))*bz(ii,jj)-2*invtm*bzprev(ii,jj)+(invtm-(gammam(radhz(i))/(2*mu*dt)))*bzprevprev(ii,jj)+A*(2*invt-(0.5*wpmsq(radhz(i))))*hzprev(ii,jj)-A*(invt-(gammam(radhz(i))/(2*dt))+0.25*wpmsq(radhz(i)))*hzprevprev(ii,jj))/(invt+(gammam(radhz(i))/(2*dt))+0.25*wpmsq(radhz(i)));
end

% Hz update for PML

hz(:,1:PMLw) =(1/mu)*bz(:,1:PMLw);
hz(:,je-PMLw+1:je) =(1/mu)*bz(:,je-PMLw+1:je);

%%%%%%%%%%%%%%%%%%%%%%%%%%%%%%%%%%%%%%%%%%%%%%%%%%%%%%%%%%%%%%%%%%%%%%%%%%%%%%%

% Hz and Bz source update

%hz(1:ie,js) = amp*sin(omega*t)*ones(ie,1); % store field source in Hz
%bz(1:ie,js) = mu*hz(1:ie,js);

for i=1:ie

hz(i,js) = hz(i,js) + amp*sin(omega*t);
bz(i,js) = mu*hz(i,js);

end

%%%%%%%%%%%%%%%%%%%%%%%%%%%%%%%%%%%%%%%%%%%%%%%%%%%%%%%%%%%%%%%%%%%%%%%%%%%%%%%

% Hz mask for in the PEC
```

```
hz(:,:) = hz(:,:).*hzmask;
bz(:,:) = bz(:,:).*hzmask;

%%%%%%%%%%%%%%%%%%%%%%%%%%%%%%%%%%%%%%%%%%%%%%%%%%%%%%%%%%%%%%%%%%%%%%%%%%%%%%%

%Time stepping - store field information

Dxtemp = Dxprevprev;
Dxprevprev = Dxprev;
Dxprev = Dx;
Dx = Dxtemp;

Dytemp = Dyprevprev;
Dyprevprev = Dyprev;
Dyprev = Dy;
Dy = Dytemp;

extemp = exprevprev;
exprevprev = exprev;
exprev = ex;
ex = extemp;

eytemp = eyprevprev;
eyprevprev = eyprev;
eyprev= ey;
ey = eytemp;

dbarxtemp = dbarxprevprev;
dbarxprevprev = dbarxprev;
dbarxprev = dbarx;
dbarx = dbarxtemp;

dbarytemp = dbaryprevprev;
dbaryprevprev = dbaryprev;
dbaryprev =dbary;
dbary = dbarytemp;

bztemp = bzprevprev;
bzprevprev = bzprev;
bzprev = bz;
bz = bztemp;

hztemp = hzprevprev;
hzprevprev = hzprev;
hzprev = hz;
hz = hztemp;

%Loop image, save to AVI video file

timestep=int2str(n)
pcolor(ex'); % creating pseducolor plot
colormap jet;
hold on; % start to draw circles
circle(icenter,jcenter,R1); % get function from circle.m
circle(icenter,jcenter,R2); % get function from circle.m
hold off;
shading flat; % setup mesh color
caxis([-80 80]); % color limit
axis([1 ie 1 je]); % x and y axis limit
colorbar;
axis image; % same data length for x and y
title({['Ex at time step =', timestep];['Q-factor =', num2str(q)]});% title of the image
```

```
img = hardcopy(hFig, '-dzbuffer', '-r0');
writeVideo(aviobj,im2frame(img));

end

% end time loop

close(aviobj)

%%%%%%%%%%%%%%%%%%%%%%%%%%%%%%%%%%%%%%%%%%%%%%%%%%%%%%%%%%%%%%%%%%%%%%%%%%%%%%%%%%%%%%%%%%%%%

% save data in csv

for i=1:jb
count(i) = i;
end

newdata = [count;ex(icenter,:)];

csvwrite('csvlist.csv',newdata);
```

Function to draw circles to indicate where the cloaking shell is located (need to be save as 'circle.m' for the main script to use this function):

```
function circle(x,y,r)

%x and y are the coordinates of the center of the circle

%r is the radius of the circle

%0.01 is the angle step

ang=0:0.01:2*pi;
xp=r*cos(ang);
yp=r*sin(ang);
plot(x+xp,y+yp,'-k','LineWidth',1);
end
```